POLITECNICO
MILANO 1863

SCUOLA DI INGEGNERIA INDUSTRIALE
E DELL'INFORMAZIONE

Thermal Management System for an Am-241 based European RPS powered Ice-mining Lunar Rover

Tesi di Laurea Magistrale in
Space Engineering - Ingegneria Spaziale

Author: **Marzio Mazzotti**

Student ID: 951092
Academic Year: 2022-23
Advisor: Prof. Michèle Roberta Lavagna
Co-advisors: Prof. Wang Weizhong, Dr. Alessandra Barco

Abstract

Lunar high latitude regions contain rich deposits of water ice. Water and other volatiles were directly detected by the LCROSS mission in 2009. Remote sensing measurements further corroborate the theory of the presence of vast ice deposits in the Permanently Shadowed Region (PSR) craters. Water ice deposits on the Moon are very valuable to the space community as in-situ extracted water can be used for many purposes, such as LOX/LH2 propellant couple production and human habitat support. PSR craters never see sunlight, so Solar power is not available there. They also present a cryogenic environment, with regolith as cold as 40K. These challenges can be overcome employing a Radioisotope Power System (RPS). NASA is planning to launch VIPER, a RPS powered rover that will explore Lunar poles surveying the PSR and prospecting for water and other volatiles, by the end of 2024. The work presented in this thesis aims at characterizing an ice-mining Lunar rover further developing VIPER concept. The rover will be equipped with an ESA designed Americium 241 based RPS. Am-241 has a 432-year long half-life and can provide decades of stable energy output for the rover operations. The innovation lies in the fact that the RPS will not only provide electrical power to the rover, but that its waste heat will be employed to thermally mine ice from its deposits. The rover is equipped with a sublimation plate, irradiating the underlying regolith to sublimate ice contained within; and with a cold trap, where extracted volatiles will be deposited. This work studied the rover concept feasibility, developing a model of its thermal management system (TMS) to meet sublimation plate and cold trap temperature requirements. The rover TMS design started with tradeoff studies to characterize its core architecture. The process has been iterated through a thermal network 1D analysis. Finally, results have been validated by a 3D finite element method thermal simulation. The findings of this work show that it is possible to perform ice-mining in the Lunar PSR environment, with different degrees of efficiencies depending on the amount of ice in the deposits.

Keywords: Moon, Lunar ISRU, Lunar thermal ice-mining, Lunar water extraction, ice-mining Lunar rover, Radioisotope Power System, Stirling converter, Americium 241.

Abstract in lingua italiana

Le regioni polari della Luna ospitano ricchi giacimenti di ghiaccio, ubicati nelle zone permanentemente in ombra (PSR). Lo sfruttamento dei giacimenti di ghiaccio Lunare è di grande interesse per la comunità spaziale grazie alle prospettive economiche e scientifiche che l'utilizzazione delle risorse in situ (ISRU) offre. L'acqua estratta in loco può essere impiegata per la produzione di propellente, o per il sostentamento di habitat umani. Le PSR non vedono mai la luce solare, rendendo impossibile il ricorso a sistemi fotovoltaici e presentando temperature criogeniche. Queste problematiche possono essere risolte grazie all'uso di generatori di potenza a radioisotopi (RPS). La NASA sta preparando la missione VIPER: un rover equipaggiato con RPS, esplorerà le PSR del polo sud Lunare. Il lavoro presentato punta a caratterizzare il sistema di gestione termica (TMS) di un rover Lunare per l'estrazione del ghiaccio, sviluppando ulteriormente il concetto di VIPER. Il rover oggetto di questa ricerca sarà dotato di un RPS di realizzazione ESA alimentato ad Americio 241, un radioisotopo con un'emivita di 432 anni, che può fornire un output energetico stabile per decadi. L'innovazione di questo lavoro sta nel fatto che il generatore a radioisotopi non fornirà solo potenza elettrica al rover, ma che anche il suo calore di scarto sarà usato per estrarre ghiaccio termicamente. Il rover è equipaggiato con una piastra di sublimazione che irradierà la regolite con il calore di scarto del RPS, facendo sublimare il ghiaccio in essa contenuto; e con una "trappola fredda", dove il vapore si depositerà. Questo studio ha investigato la fattibilità di tale progetto tramite la simulazione del TMS per soddisfare i requisiti di temperatura su piastra e trappola fredda. Il lavoro è iniziato con degli studi di tradeoff per delineare l'architettura base, che è poi stata iterata attraverso un'analisi termica 1D. Infine, i risultati sono stati validati da un'analisi FEM 3D. Le conclusioni raggiunte hanno dimostrato che è possibile estrarre termicamente il ghiaccio dai giacimenti delle PSR Lunari. L'efficienza dipende dalla quantità del ghiaccio nei giacimenti.

Parole chiave: Luna, Utilizzazione delle risorse in situ, Estrazione termica del ghiaccio Lunare, Estrazione di acqua Lunare, Rover Lunare per l'estrazione del ghiaccio, Generatore di potenza a radioisotopi, Conversione Stirling, Americio 241.

Contents

List of Figures

List of Tables

1 | Introduction

1.1. Background

The Moon is Earth's only natural satellite and the gateway that could give humanity access to the rest of the Solar System. The establishment of an operative base will be the first step of any reasonably successful attempt by humanity to further explore and colonize the Solar System and reach its boundaries. In fact, the Moon, has an energetically advantageous position at the edges of Earth's gravity well, corresponding to a characteristic orbital energy (C_3) with respect to Earth's gravitational pull of around -1 km^2/s^2. This value can be calculated by substituting Earth gravitational parameter μ, and Moon's orbit semi-major axis a, in the formula:

$$C_3 = -\mu/a \tag{1.1}$$

A great variety of transfer to Low Lunar Orbits (LLO) is available to be employed by mission designers to reach this first stepping stone: direct transfers, lasting from 2 to 6 days, would require a launcher characteristic energy of at least -2.06 km^2/s^2, and a Lunar orbit insertion ΔV values of at least 813 m/s [1]. Furthermore, libration orbits around Lagrangian points, coupled with the influence of Solar gravitational pull, render possible many families of low energy transfers to LLO, saving even more against a longer transfer time ΔV [1]. Finally, these transfer orbits exist in families: low energy transfer would be extremely flexible with respect to time window and Lunar orbit insertion conditions, such as arrival time or geometry [1].

Hence, exploiting the Moon advantageous position at the edge of Earth's gravitational sphere of influence, would enable the division of a very energetically demanding mission into two legs: a cis-Lunar one and a trans-Lunar one, with a refuelling in between. In this way, the Moon may act as a springboard for exploration and human colonization of the Solar System.

To provide the reader with an idea of the launch C_3 benefits, MAVEN and Mars InSight, were launched with a C_3 of 12.2 km^2/s^2 and 8.19 km^2/s^2, respectively [2, 3]. Juno, NASA's last mission to Jupiter, which reached its target after several flybys, was inserted into the first heliocentric leg of its interplanetary travel with a launcher C_3 of 31.1 km^2/s^2 [4]. As a mean of comparison the characteristic energy of the ISS, calculated through Equation 1.1, is -59.2 km^2/s^2, corresponding to a Low Earth Orbit (LEO) at 400 km altitude.

Such high C_3 requirements drastically limit currently launched spacecrafts mass budget. The ability to refuel midway with a stopover on the Moon would enable massive missions to reach Solar System destinations currently beyond our technological means, empowering humanity to design ambitious explorations missions, which could culminate with the establishment of a human presence on Mars [5].

1.1.1. American efforts: NASA Artemis program

NASA, with the Artemis project, has already laid out a schedule to operate a series of missions with the purpose of bringing astronauts back on the Moon, as shown in Figure 1.1. It is to be noted that the program has faced various technical setbacks and delays, caused by the COVID-19 pandemic and adverse weather events, which pushed launch schedules away from NASA current goals [6]. In fact, Artemis I has been launched on November 2022, one year later than anticipated, so also subsequent missions had to be postponed.

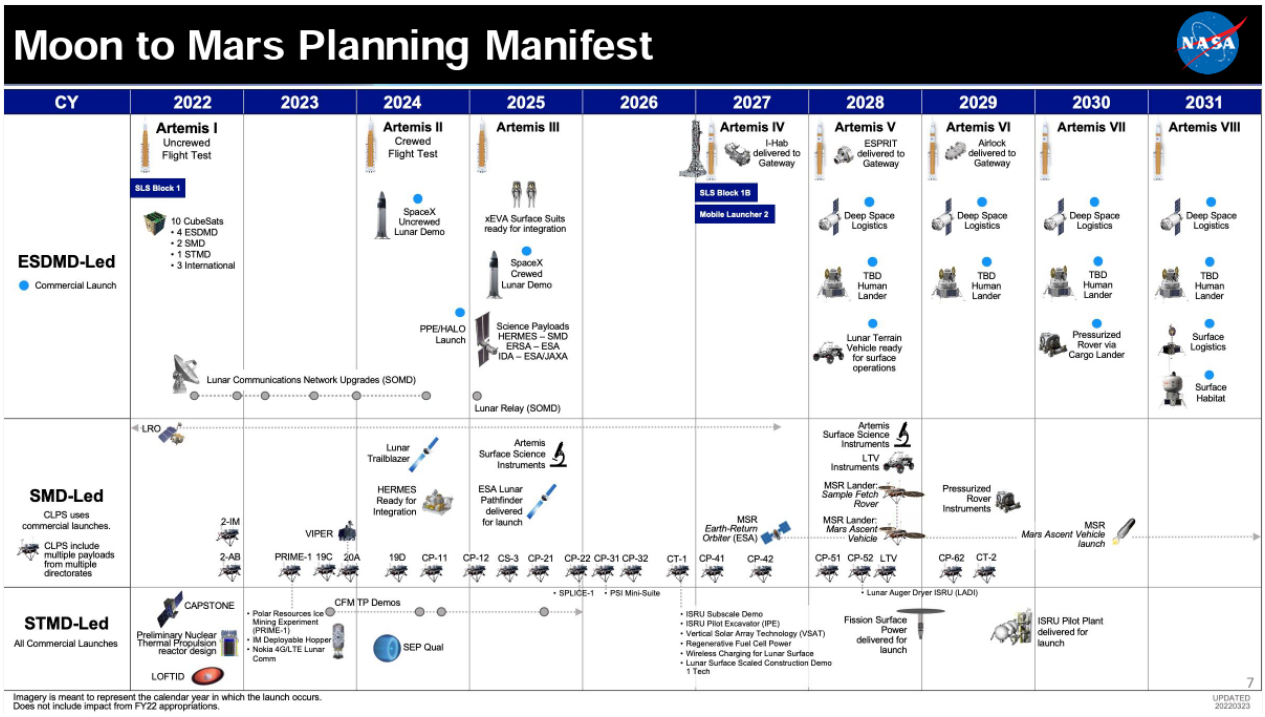

Figure 1.1: Timeline of NASA Artemis and related commercial launches [7].

The Artemis program is a multi-decennial endeavour, in its first tranche of missions, focused on reaching the Moon, NASA will concentrate on regaining and perfecting the human spaceflight capabilities first developed during the Apollo program. Apart from multiple Lunar crewed and robotic missions, the programs aims at establishing a space station in Lunar orbit, Gateway, and to land a polar prospector rover (VIPER), to identify suitable locations for In-Situ Research and Utilization (ISRU) operations, among many others. These developments are all instrumental to establishing a permanent human presence on the Moon. To reach this ambitious goal, NASA

has developed the Space Launch System (SLS), an expendable super-heavy launcher, and Orion, a partially reusable spacecraft capable of supporting a crew of six astronauts beyond LEO. In its second stage, NASA plans to leverage the Lunar base and infrastructure to enable and facilitate human exploration of Mars [5]. In this scenario, Lunar ISRU capabilities, will prove pivotal both to enable the subsistence of a permanent outpost and to refuel the launchers for the second leg of their cruise.

1.1.2. European efforts: ESA Terrae Novae 2030 program

In parallel with NASA, ESA is also working to reach the Moon in the next decade, with the Terrae Novae 2030 program. The program focuses on three space environments, seen as a set of progressive destinations: Low Earth Orbit (LEO), the Moon and Mars. The European human journey into the Solar System will rely on the utilisation of an expanded LEO and Lunar infrastructure, able to support future missions to Mars, while astronauts will also be preceded by a series of robotic precursor missions [8]. The program have a strong focus on European autonomy, in order to provide means of access to space to European technologies, scientific instrumentation and experiments, without having to rely on international partners. Alleviating this type of dependency will also stimulate European companies participation in the space economy, fostering the growth of a vibrant and dynamic commercial space ecosystem within Europe [9].

As the final destination of Terrae Novae 2030 is Mars, a human mission to the red planet will necessitate the support of large infrastructure both in LEO and on the Moon, together with a whole set of technologies and capabilities that must be mastered and developed beforehand. An example of them is advanced environmental control and life support systems, paired with Lunar ISRU systems to support them [9]. Figure 1.2 illustrates European ambition for autonomous roles, in green, plus its contribution to international partners The outlined milestones have been conceived in a step-wise and buildup fashion, so that the objective of an earlier goal is the stepping stone for a later one. Operative capabilities develop in cis-Lunar space from LEO to Moon surface access, mobility, and finally ISRU [9].

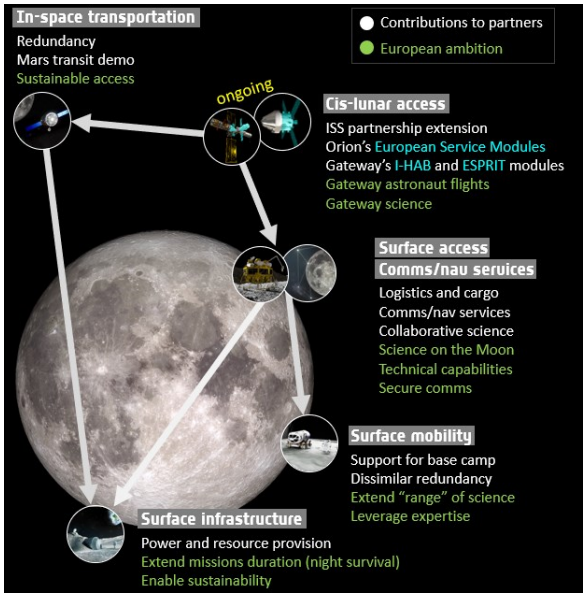

Figure 1.2: European contribution to partners and independent ambitions to reach and colonize the Moon [9].

1.1.3. Chinese efforts: CNSA Lunar Exploration program

NASA and ESA are not the only space agencies interested in reaching the Moon and establishing a permanent base: China National Space Administration agency (CNSA) has also set their gaze up on the Moon with the Chinese Lunar Exploration Program (CLEP).

CLEP is divided into four phases, as illustrated in Figure 1.3. The first consists of the launch of two Lunar orbiters, the second is the launch of soft-landing capable spacecraft, which would deploy Lunar rovers, and the third one being a sample-return mission and the fourth one the development of an autonomous Lunar research station on the Moon south pole.

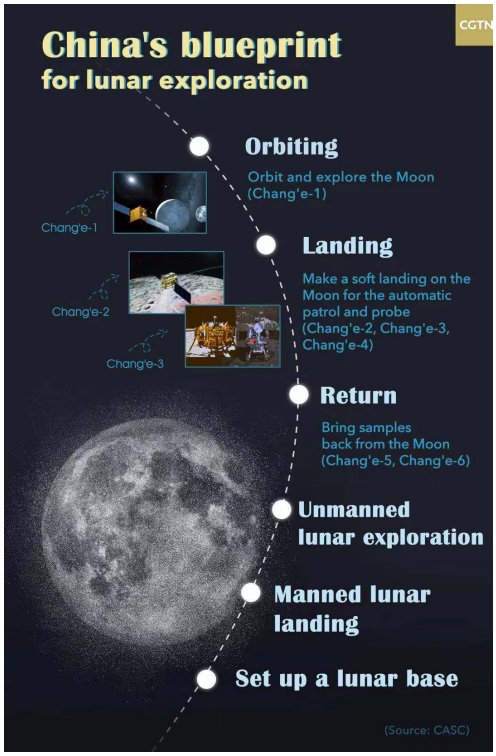

Figure 1.3: CLEP infographic

As today, phases I to III have been successfully completed: Chang'e 3 and 4 landed on the Moon on 14 September 2013 [10] and 3 December 2019 [11], respectively. The two missions landed the rovers Yutu and Yutu II, the latter being deployed on the far side of the Moon [11]. Phase III aim was accomplished 6 December 2020, when Chang'e 5 returned to Earth with a payload of 2 kg of Lunar soil, for the first time in more than four decades, after the end of the US Apollo and Soviet Luna programs [12].

1.1.4. ISRU in the framework of US, EU and Chinese programs

Being part of this grander picture, Lunar ISRU will be pivotal to enable a new wave of bold and ambitious missions around the Solar System. Lunar ISRU will make possible the launch capabilities needed by similar endeavours, by sustaining the permanent outpost that such kind of launch facilities would require. Furthermore, not only will ISRU infrastructures allow for an autonomous Lunar base, but they will also help containing mission costs by enabling propellant production directly on site, making the funding of larger missions more economically feasible by diminishing the propellant mass necessary to the launch systems. Finally, water may even be employed for shielding humans from cosmic and solar radiations while outside Earth magnetosphere, both on large scales in the insulation of building and at smaller scales directly integrating a layer of water in astronauts' suits [13, 14].

1.2. Research and Exploration significance of Lunar ISRU

It is clear that Lunar ISRU harbours a great potential, while still presenting many unresolved problems and criticalities, as it is normal with any novel concept that has yet to be extensively put into practice. Therefore, it is extremely important to carry out more research on the topic.

One of the most important criticalities regarding the development of ISRU technologies is the harsh environment in which resource extraction would need to be carried out. For instance, the greatest part of Lunar ice deposits for water extraction, the main focus of this work, are located at the poles, in the so called Permanently Shadowed Regions (PSR). In fact, it has been estimated that the uppermost layers of Lunar regolith in PSR could hold as much as 2.9 billion tons of water [15]. These areas are mainly placed inside craters located in the polar regions, especially in the southern hemisphere, whose rims, due to the low inclination angle of the Moon axis, cast a long shadow when illuminated by the Solar light parallel to the surface. As these areas are never under direct sunlight, the temperature of the regolith can reach temperatures as low as 30 K [16, 17]. Any ice-mining rover would hence need to operate in such a harsh cryogenic environment, under a set of extremely restrictive requirements from the thermal control and electrical power subsystems point of view.

The research significance of any effort aimed at developing water ISRU capabilities in complete absence of sunlight and cryogenic temperature environment can also have numerous applications beyond Lunar water extraction. In fact, breakthrough in this field could also further contribute to the design of gaseous giants moons exploration missions, such as Encedalus for Saturn and Triton for Neptune. It could also provide insights for scientific missions to other remote celestial objects at the fringe of the Solar System, such as Trans-Neptunian and Kuiper belt objects.

1.3. Economic significance of Lunar ISRU

Following the recent trend of private enterprises entering in the space economy, Lunar ISRU is a particularly fertile ground for a future participation of industry actors in partnership with government agencies. One of these examples is NASA Commercial Lunar Payload Service (CLPS) program. The CLPS program aims to contract transportation services of small robotic landers and rovers hosting scientific and demonstrative payloads to third party industrial partners [18].

Figure 1.4 shows NASA CLPS program delivered missions. It is possible to notice how half of them focus on the south polar region: a proof of the importance that this area of the Moon will hold in the next decades, thanks to its abundance of natural resources deposits. In fact, many of this missions' objective is ISRU related, as with the case of VIPER: NASA's Volatiles Investigating Polar Exploration Rover. The rover will be the first explorer of Lunar PSR and

one of its mission objective is to characterize the local environment and prospect for ice deposits, paving the way for their future large scale utilisation.

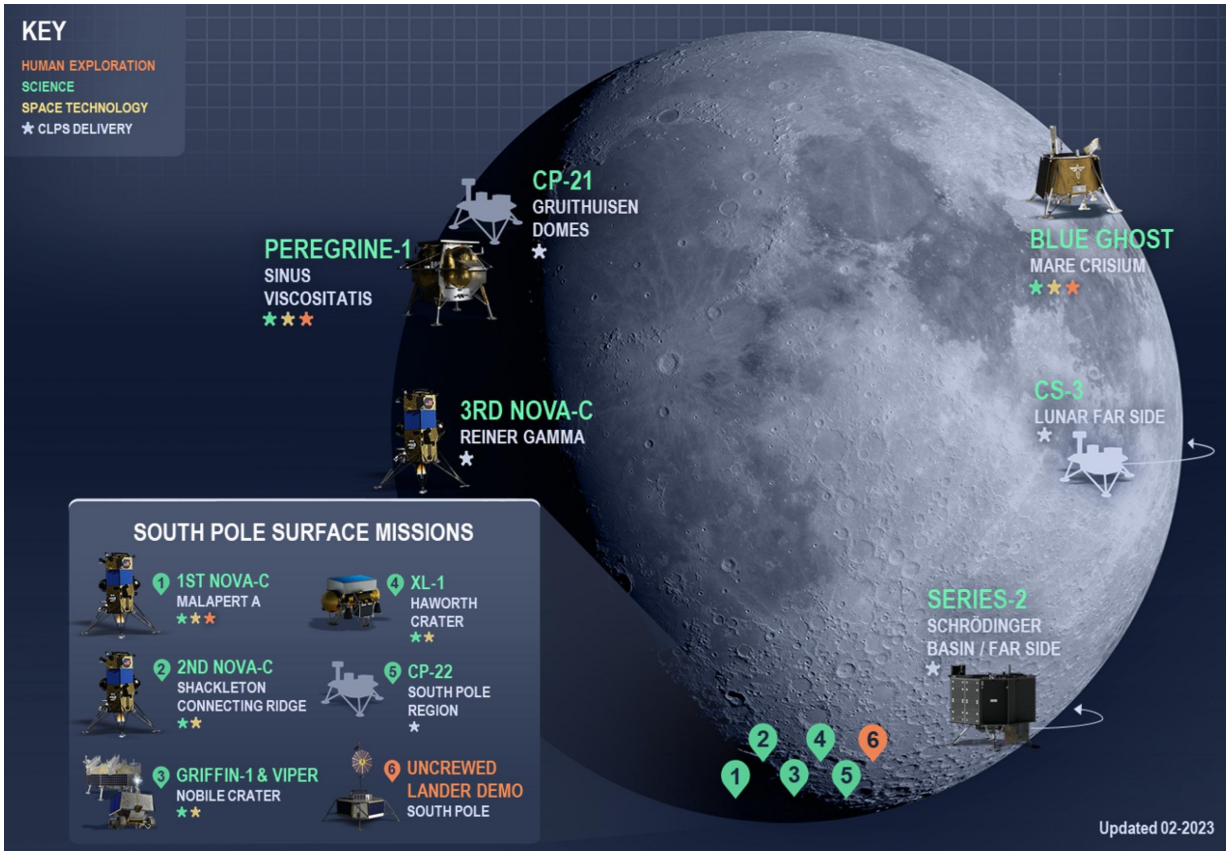

Figure 1.4: Commercial Lunar Payload Services (CLPS) Deliveries [19].

Apart from the primary aim of securing means of access to space for smaller class missions, NASA CLPS program has the objective of fostering the growth of the private sector's participation in the space economy, lowering the expensive initial investment that characterizes this kind of endeavours through a series of government contracts intended to encourage the build-up of capabilities and know-how inside private industry partners.

Furthermore, ISRU operations, once successfully established, could be easily scaled up following demand, and once the initial concept has been devised, the scaling up of operation would reasonably be dependent only on available capital.

Finally, reliance on private partners would help governmental agencies keeping operational cost low and would free up funding for higher added value scientific research, while also fostering the development of a flourishing private space sector able to retain know-how and developing new technologies.

2 | Dissertation objectives

The objective of the current work is to develop a preliminary design of an ice-mining Lunar rover concept which utilizes the waste heat from a Radioisotope Power System (RPS) for heating and sublimating icy Lunar regolith. The project will focus on the design of the Thermal Management Subsystem (TMS) for the ice-mining rover concept. The TMS will include a sublimation plate for sublimating icy-deposits within the permanently shadowed Lunar regolith and a cold trap for trapping expelled volatiles. The area underneath the rover's sublimation plate, where ice extraction will be carried out, shall be contained in a pressure controlled environment, sealed from the outside, in order to avoid losses of volatiles to the completely depressurized atmosphere devoid Lunar surface environment, but also to drive the extracted water to the cold trap by means of pressure differential.

2.1. The ice-mining Lunar rover baseline

The rover design analysed in this research project is the one presented in [20], and its concept has been developed by researchers of University of Leicester Space Park. The rover will be powered by an RPS which waste heat will be directed to the sublimation plate, so that the heat coming from the radioisotope fuel will both power up the electric power subsystem and the mining efforts. Apart from the RPS and the ice-mining subsystem, the rover will be equipped with nothing more than batteries, the mobility and the telecommunication system, with the related electronics.

The RPS will be powered up by Am-241 based oxide fuel pellets gathered in two heat sources, assumed to be on the scale of the European Large Heat Source (ELHS) modules, utilising a total of ∼2 kg of fuel each, and able to produce ∼200 W_{th} each. The choice of two ELHS comparable modules is based on current fuel production estimates and a target launch date of 2030 [20, 21]. The total amount of thermal power available for the RPS has been baselined as ∼400 W_{th}, which, according to the conversion technology employed by the RPS, would become ∼20 W_e & ∼380 W_{th} with a static thermoelectric conversion and ∼80 W_e & ∼320 W_{th} with the dynamic Stirling engine conversion option [20, 21]. The leftover thermal power, commonly known as waste heat in RPS applications, can be used for keeping the rover subsystems warm,

and more importantly, to heat up the sublimation plate. The minimum specific area thermal power to sublimate the stored ice deposits is targeted as 1 kW/m^2 [22], a value similar in order of magnitude to the solar irradiance on the Lunar surface. According to the Stefan-Boltzmann for irradiation:

$$\dot{Q} = \sigma \varepsilon T^4 \tag{2.1}$$

the minimum operating temperature required for the sublimation plate is derived. Considering an emissivity value ε of 0.9 and a view factor between the plate and the Lunar soil of 1, a reasonable approximation due to the proximity between the two objects, a temperature of 100°C will be sufficient to achieve the required heat flux. This calculation also relies on the negligibility of the irradiative heat flux incoming from the regolith, as with the very low temperatures that characterize the PSR craters [23, 24], it will amount to, at most, only a few tens mW. A first order estimate of the plate size, A, can be calculated as in Equation 2.2 [20, 21]:

$$A = \eta \cdot P_{th}/S \tag{2.2}$$

Where η is the thermal management system efficiency, P_{th} is the thermal power output from the RPS made available to the ice-mining operations, and S is the target specific thermal power output of the plate. The waste heat made available to the sublimation plate will likely be lower than the total amount of heat waste from the RPS as a fraction of it will be used for the thermal management of the other rover components. The sublimation plate size will be function of both the thermal power provided by the RPS and the efficiency of the Thermal Management Subsystem (TMS). Plate sizes vary between 0.24 m^2 and 0.32 m^2 over the range of efficiencies investigated [20, 21].

Once heated up, some released water gases will migrate towards unheated regolith regions nearby, refreezing. Even if this is not optimal, the water will not be lost as it could be sublimated again at later times. The volatiles able to be extracted from the soil will be collected by a cold trap. The volume below the rover will be sealed with deployable walls, so to minimise water losses to the environment and to guide it to the cold trap. Wall material will also be reflective of thermal energy to help concentrate the sublimation plate radiated heat [20]. The cold trap is sketched as hollow volume with an opening facing down towards the regolith. Fins present on the interior to facilitate water refreezing will be connected to external radiators through heat pipes or other conductive devices. The opening of the cold trap could be sealed during roving, to avoid intrusion of Lunar dust.

The rover ice-mining operations could be subdivided into 4 phases [20], as shown in Figure 2.1.

In phase I, or Roving to Ice Deposit, the rover will likely be powered up by a combination of RPS power output and battery energy. The waste heat of the RPS could be radiated away from a sky facing radiator. The possibility of doing that is currently being explored and will be part of this research work. During phase II, called Isolating Ice Deposit, the sealing walls will be deployed until they cover possible leakage ways for the extracted volatiles to obtain the reasonably best sealing achievable with their capabilities. Phase III, or Volatile Extraction, will see the rover completely idle while the waste heat from the RPS is being diverted to the sublimation plate and water vapours are being refrozen in the cold trap. According to the estimates of water concentration of 5-10 vol.% and 1 kW/m^2 heating power, this phase is set to last for around 2 days [22]. During this phase, there is also the occasion for batteries to be recharged, in order for the rover to be ready for the voyage to the next plot of regolith. Phase IV, the last phase, called Separation from Deposit, consists of the closing of the cold trap door and the raising of the sealing walls. After these two operations have been carried out, the rover will be ready for a new cycle of extraction operations over a new ice deposit.

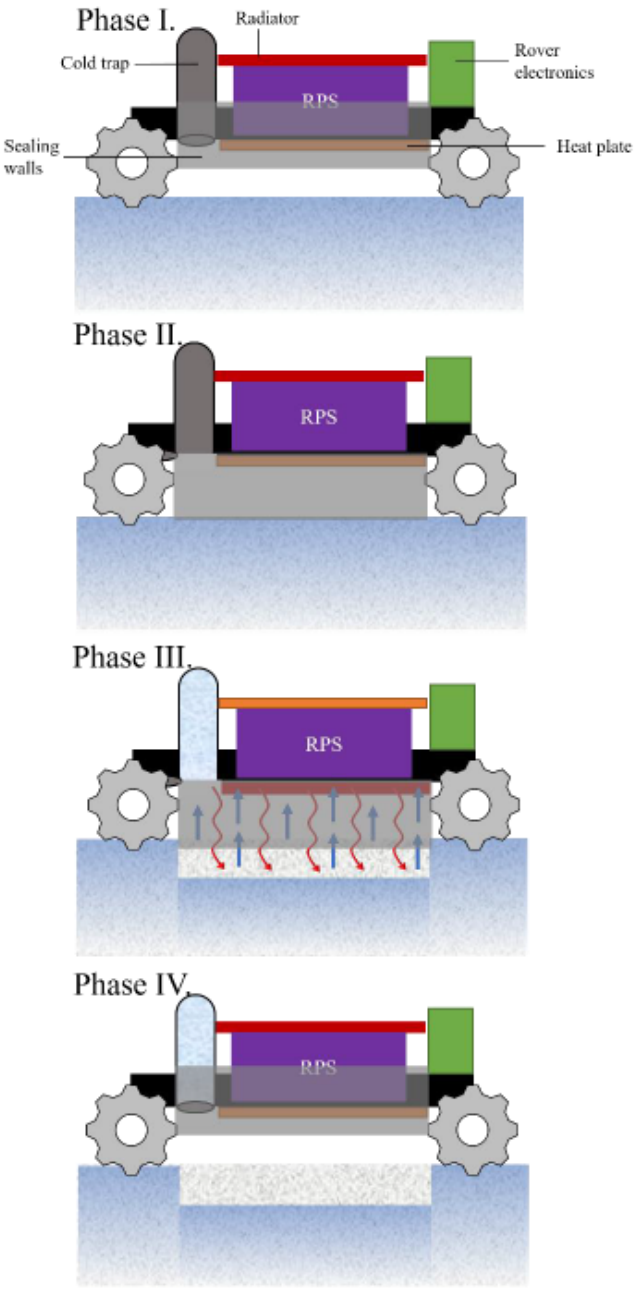

Figure 2.1: Proposed operative schedule for a single ice-mining cycle [20].

2.2. Basic requirements

As introduced in the previous section, a set of three basic requirements can be extrapolated from the presented ice-mining Lunar rover concept. They represent the minimum amount of requisites in order to perform ice mining. They are, in order of importance:

- The sublimation plate must be able of providing 1 kW_{th}/m^2 to the surface of the Lunar regolith. This can be translated into a temperature requirement, mandating that the sublimation plate temperature must be at least 100°C during the whole extraction phase;
- The cold trap must be cold enough to allow water volatiles deposition on its internal surfaces. The exact temperature requirement depends on the maximum allowable pressure inside the sealing walls. -20°C has been selected as maximum cold trap temperature;
- To guarantee rover operativity, a minimum electrical output must be provided by the RPS. A power budget projection will be drawn out and the electrical power requirements compared to the RPS modeled output.

2.3. Additional requirements

Apart from the basic requirements reported in the previous section, which have been formulated to enable water extraction, a second set of "nice to have" requisites can be listed. These requisites are a corollary of the core ones and they aim at extraction operation and the RPS power conversion efficiency increase:

- TMS efficiency increase: to maximize extraction efficiency, the design will attempt to optimize and use the maximum amount of available waste heat from the RPS. This means that heat losses should be controlled and limited.
- Limitation of thermal losses: especially parasitic heat transfer pathways from TMS hot elements to the cold trap, which increasing the temperature of the latter twice penalise the extraction operations.
- Moderate RPS radiator temperature: to increase the RPS electric power output by raising conversion efficiency, its radiator temperature should be kept as low as possible. This requirement is overshadowed by the over the minimum plate temperature.

Finally, various other requirements could be added on the TMS, the effective need for them will be object of tradeoff studies presented in the first part of the technical work. The leitmotif underlining this preliminary ISRU mission characterization effort will be to avoid any unnecessary system complexity. Hence, additional requirements will be added only either if strictly required for the rover survival or if proven greatly beneficial for the ice-mining operations.

2.4. Research scope

This study has a very broad scope, while the objective to characterize and develop a single ice mining system to be employed on board of a Lunar rover might seem circumscribed to a very narrow and limited field of applications, that is not true. In fact, the scope ranges among the following concepts and fields:

- **Lunar ISRU:** the motif below the research effort. The ability to extract, process and store water on the Moon is a necessary step for the establishment of a human settlement.
- **Economical feasibility of Lunar ISRU:** After the first ISRU technologies will be demonstrated, Lunar ISRU will become fertile ground for the participation of private sector in the mining operations. The ice-mining Lunar rover concept is optimal under an economical feasibility point of view, as operations could be scaled incrementally, gradually following the increase of water demand.
- **Bolstering future exploration capabilities:** the longest-term objective and ultimate reason for the development of ISRU capabilities is the future prospect of increased exploration capability that a Lunar base will allow, enabling more complex Solar System robotic exploration missions and culminating with a crewed mission to Mars.
- **RPS development:** the absence of sunlight in the mining areas warrants the employment of an RPS system. The need for extensive use of RPS systems in case of ISRU operation scaling up would be a great opportunity for the nascent ESA RPS program.
- **RPS integration:** the most innovative aspect of this work, the integration of the RPS on the ice mining rover to double up its functions. The waste heat coming from the RPS will not be considered a by-product of the electrical power conversion process, but will also become an extremely valuable resource enabling water extraction.
- **Operation in extreme environment:** the Lunar PSR environment poses a set of strict constraints. Very few missions have ever ventured in similar environments: baselines are scarce and new innovative solutions will need to be devised to enable the rover survival.

2.5. Technical routes

The main technical route of this work relies on the rover TMS thermal modeling. A brief initial part will be based on literature research to select RPS thermal to electric power conversion technology able to provide enough electrical power to guarantee the rover basic operations. To do this, a preliminary power budget for the ice-mining Lunar rover will be delineated. Subsequently, after the thermal mining power budget has been set, trade-off studies will be conducted on MATLAB Simulink by laying out a 1D thermal network. Once the TMS architecture have been set, various rounds of iterations will be performed synergising the aforementioned MATLAB Simulink 1D thermal network with a more in depth 3D finite element thermal analysis on Siemens NX. The latter step will also require the CAD drawing of the rover and its TMS, also performed on NX. Finally, MATLAB Simulink and Siemens NX thermal models final version results will be employed to validate the feasibility of the ice-mining Lunar rover concept.

3 | Literature review

3.1. Overview of Lunar ISRU

The concept of Lunar ISRU is a major point of focus for Solar System exploration and colonization efforts as it often proves as a vital enabler for missions that could otherwise be unfeasible under the current state of the art. In fact, the utilization of local Lunar resources will help to alleviate the onerous mass constraints for the more ambitious missions, using the Moon energetically advantageous position at the edge of Earth's gravity well as an intermediate step between the Earth and the other planets of the Solar System. Lunar ISRU efforts concentrate on the extraction of oxygen and water, but also metals and even solar wind implanted volatiles, such as Helium isotopes, a likely fuel for nuclear fusion [25], could be gathered from the Lunar regolith [26]. Table 3.1 shows most relevant solar wind implanted volatiles, among which lies ^{3}He, together with their concentration and average mass per m^3 of regolith.

Volatile	Concentration ppm (μg/g)	Average mass per m^3 of regolith (g)
H	46± 16	76
^{3}He	0.0042± 0.0034	0.007
^{4}He	14.0± 11.3	23
C	124± 45	206
N	81± 37	135
F	70± 47	116
Cl	30± 20	50

Table 3.1: Concentration of Solar wind implanted volatiles in Lunar regolith [26].

Figure 3.1 shows the chemical composition of Lunar regolith according to the samples brought back to Earth by Apollo 16. Oxygen is of particular interest as it can be used to sustain human life and it provides 75% to 80% of chemical propulsion propellant mass [26]. This would enable refuelling of launchers after they have landed on the Moon, so that lighter and cheaper mission could be launched, or, as an alternative, heavier payloads, at the same price. Oxygen comprises more that 40% of the Lunar regolith by mass [26].

There are several methods of producing oxygen from regolith. Some examples of the available technologies are: reduction with hydrogen, reduction with methane, vapor phase pyrolysis, sulphuric acid reduction, electrolysis of molten and solid Lunar regolith. Furthermore, there are some specific electrolysis processes, such as the FCC-Cambridge, which, conducted on solid Lunar regolith, are able to yield useful metals as by-products [27]. Oxygen is an integral part of regolith, extraction operations would not be relegated to specific latitudes (as it would happen for water).

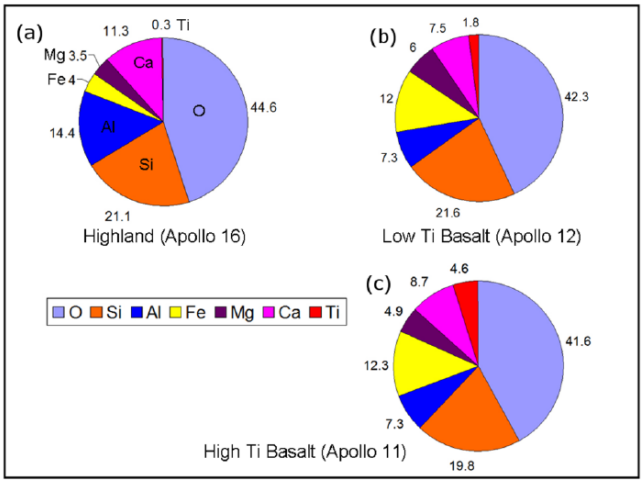

Figure 3.1: Composition of the Lunar regolith samples brought back to Earth by Apollo 16 [26].

3.2. Lunar water-ice ISRU

Water extraction, the main focus of this research work, is a key enabler for Solar System exploration and the establishment of a permanent Lunar outpost. The recent discovery of water ice in the craters of the Permanently Shadowed Regions (PSR) at the Moon poles has been defined as of "Game Changing" importance [26], as it would enable long term sustainability of a crewed base. Furthermore water would provide the totality of chemical propulsion propellant mass, unlike oxygen, which would constitute only three quarters of it: the capability of independent refueling would strongly influence design and reuse of cargo and crewed landers [26].

Observations by the Lunar Exploration Neutron Detector (LEND) and the Lunar Reconnaissance Orbiter (LRO) showed that water ice will be stable at the surface or beneath a shallow overburden no more than a meter deep [24]. Meanwhile, the Lunar Crater Observation and Sensing Satellite (LCROSS) impacted a crater located in the PSR and from the ejected materials in the plume created by the impact, the Shepherding Satellite from the analogous mission detected a water content of approximately 5.6 wt% ($\pm$ 2.9%) [28]. These measurements are very encouraging, but unfortunately, ice form, concentration and distribution remain largely unknown. Hence, any future development of Lunar water ISRU operation must be preceded by a more thorough investigation able to carefully characterize the most prospective craters. For this reason NASA is planning to launch VIPER by the end of 2024. VIPER stands for Volatiles Investigating Polar Exploration Rover, and it will explore Lunar poles surveying the PSR and prospecting for water and other volatiles [29, 30].

3.2.1. Ice deposits and Ice Stability Regions

A first order estimation of the amount of water present on the Moon has been given by [15] as 2.9 billion tons, mainly stored in cold traps, areas which present the right conditions for long term retainment of ice. Along the Moon geological history, there have been three suggested sources for the water still found today: delivery by carbonaceous asteroids, and to a much lesser extent, comets; volcanic outgassing from the lunar interior; and Solar wind implantation, combined with micrometeoroid impacts [31].

Ice from micrometeoroids, weighing less than 1 g, is the only direct way of water delivery to the cold trap, even though water could also reach the deposit by migration from nearby regions where ice cannot be stable. Comets and larger asteroids could also have substantially contributed to the accretion of ice deposits in cold traps. Depending on the size of the impacting body, large meteoroids could implant water in melts, breccias and surviving projectile fragments, which could later be vaporized and migrate to the poles [31, 32]. Even larger bodies, containing large quantities of ice and releasing greater energy on the impact, could create transient collisional atmospheres lasting from hours to days, from which ice could be captured directly in the cold traps [31, 33]. Impacts from meteoroids of any size were much more common in earlier days of the Moon geologic history; in fact, as Figure 3.2 displays, the relative impact rate of meteoroids on the Lunar surface was several orders of magnitude higher in periods earlier than 3 Ga ago, when they reached today's negligible frequency.

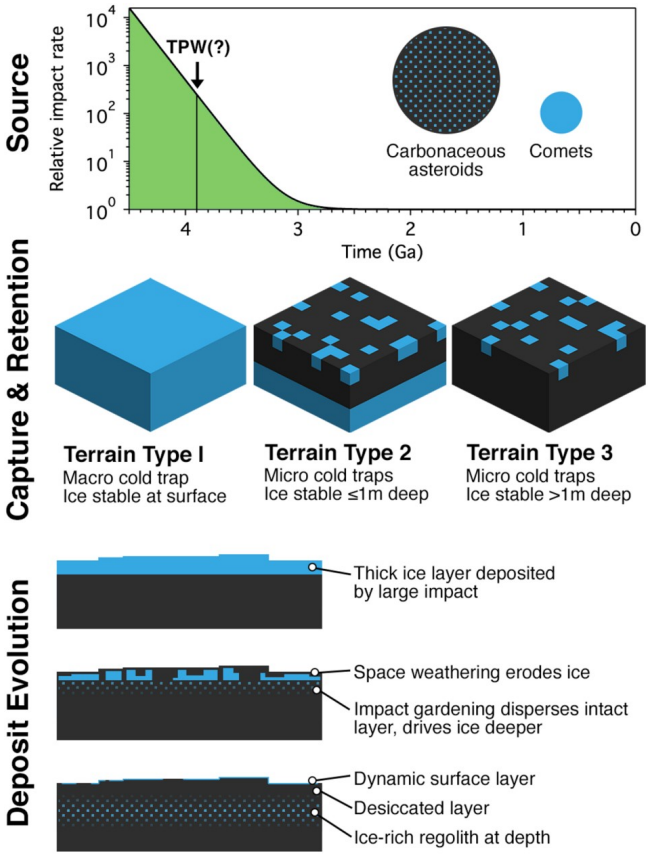

Figure 3.2: From top to bottom: Meteoroid ice source impact rate over time, with True Polar Wander date highlighted; Different types of cold trap terrain for ice capture dynamics; Evolution of ice deposits after ice capture [31].

Volcanic outgassing is another potential source of water for Lunar ice deposits [34]. Volcanic activity was much more intense in earlier ages of Moon geologic history. It is supposed that intense spikes of volcanic activity, happened between 3.8 and 3.5 Ga ago, could have outgassed

enough water vapor to have ideally deposited 1.5 m of ice deposit in the cold traps [35]. It is important to note that the previous estimation could hold only under certain specific hypothesis, such as physical vicinity between the outgassing sites and high outgassing intensity, in order to allow for the generation of collisional atmospheres and ice deposition in a similar fashion as in the asteroid impact cases [36]. In any case, water molecules implanted in equatorial regions could still have migrated to the polar cold traps regions through ballistic transport [31, 37].

Finally, Solar wind could have implanted the basic components of water molecules, especially hydrogen. All together, space weathering processes, to which ensemble Solar wind deposition belongs, could be responsible of a steady state water deposition of ∼4 wt% within the regolith column [31, 38]. The overall importance of this water source is mainly dependent on the intensity of the Solar wind, which was much higher in the early Solar System history [39, 40]. These findings support the hypothesis that Solar as a water source could be as important as the previous two, and also that, just like the previous two, its impact was much more pronounced in the early periods of Moon geological history [31].

Figure 3.2 also illustrates three types of cold traps: macro cold traps, usually located in correspondence of PSR, where temperatures are consistently low enough to have an homogeneous layer of ice stable at the surface. Micro cold traps, on the other hand, are more likely to present the conditions for superficial ice stability only for smaller areas, if any; ice can be stored under the surface at greater or shallower depths in the thermally insulating regolith [31]. These three terrain types constitute what is collectively known as Ice Stability Regions (ISR), defined as the area in which ice sublimation rate slows down to less than 1 mm/m^2 per Ga [42]. Hence, in these areas, water could be stable in ice form for geological periods of time. Ice needs temperature lower than 100 K to be able to survive for eons on the Lunar surface [43, 44], and the only place where this low temperature are possible is in PSR at the Lunar poles, or in the scarcely illuminated areas neighbouring them. Figure 3.3 shows a representation of a PSR crater and its surroundings, with the three previously mentioned terrain types. There are about 28.000 km^2 of Lunar soil that consistently present a surface temperature of 100 K or lower [42, 45], mainly located in PSR.

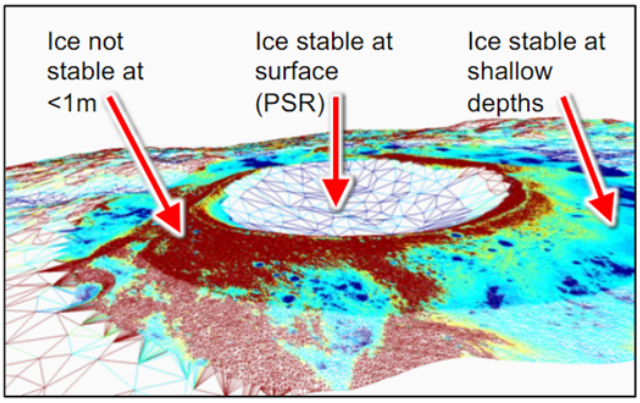

Figure 3.3: The representation of a PSR crater and its surroundings [41].

The principle method for defining an ISR is employing a thermophysical criterion, accounting for ice survivability against sublimation only [31]. There are at least other two phenomena

influencing ice at Lunar cold traps: space weathering and impact gardening. Space weathering is the least influential between the two, as incoming Solar wind only erodes superficial layers of ice, fragmenting the homogeneous ice layers formed after a deposition event. Impact gardening, conversely, is the main driver affecting the redistribution of ice at local level, and is also responsible for some water volatiles loss to space [31]. Figure 3.2 shows the evolution over time of an ideal ice deposit due to space weathering and impact gardening: depending on the energy of the impact, ice can be mixed within the regolith from centimeters to meters depths [31]. Considering the much higher impact rates from 3 Ga ago and earlier, much of the redistribution happened in concert with ice deposition due to meteoroids impacts, so that nowadays, ice originally deposited on the Lunar surface has become more homogeneously diluted over the regolith column, extending deeper as well [31, 46, 47].

ISR predictions are further complicated by Moon obliquity axis and true polar wander. In fact, the low inclination of the Moon axis favourably impact the PSR distribution, increasing the cold trap area suitable for ice retention. Moon axis, unfortunately, has not always been at the current low inclination, as around 4 Ga ago the Moon underwent 5.5° circa of true polar wander, meaning that its axis tilt changed by the previously mentioned amount [31, 48]. Figure 3.4 illustrate Lunar cold trap location before and after the true polar wander event (first and second row from top). The three ISR classifications are taken from the definitions of Figure 3.2, where TT1 means macro cold trap with ice stable on the surface, TT2 stands for micro cold trap with ice stable at depths shallower than 1 m and TT3 micro cold traps with ice deeper than 1 m

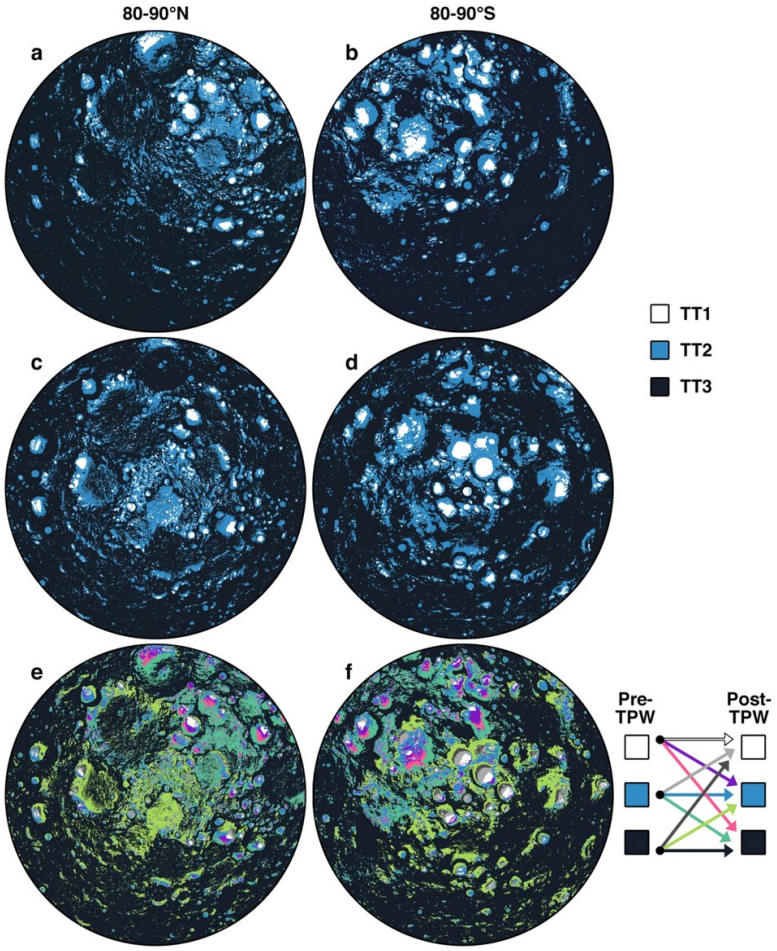

Figure 3.4: An evolution of ISR due to Lunar true polar wander, rows from top to bottom: North and South paleo poles, North and South present day poles, North and South poles variational map [31].

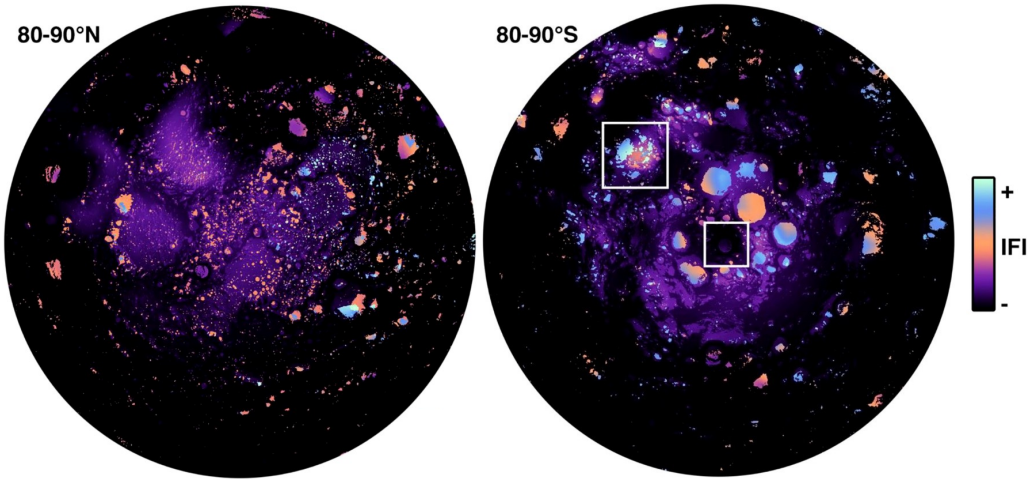

Figure 3.5: IFI for Lunar northern and southern pole, taking into account past ice sources and retention factors, including the change of ISR after the true polar wander event [31].

or no ice at all. The bottom row shows the variational map, in which the colors are linked to the kind of ISR transition happened after the true polar wander event. As the greater part of the ice meteoric impacts, as well as the other Lunar ice sources have been much more influential before the true polar wander event supposed date, it is very important to account for the ice lost in deposits that could have retained ice in ancient ages but found themselves outside of cold traps after the event. This problematic severely limits the potential ice deposits, completely disqualifying great parts of the northern hemisphere as a candidate region for Lunar ice ISRU.

Condensing all the considerations exposed in this section, it has been possible to derive an overall term for the presence of ice on the Lunar poles, which has been developed by [31], and it is called Ice Favourability Index (IFI). Figure 3.5 shows the the north and southern hemispheres polar regions, suggesting once again that the greater part of Lunar ice lies at the south pole. It also shows that not all the present-day PSR are good candidates for hosting large ice deposits, as they might have become permanently shadowed only after the true

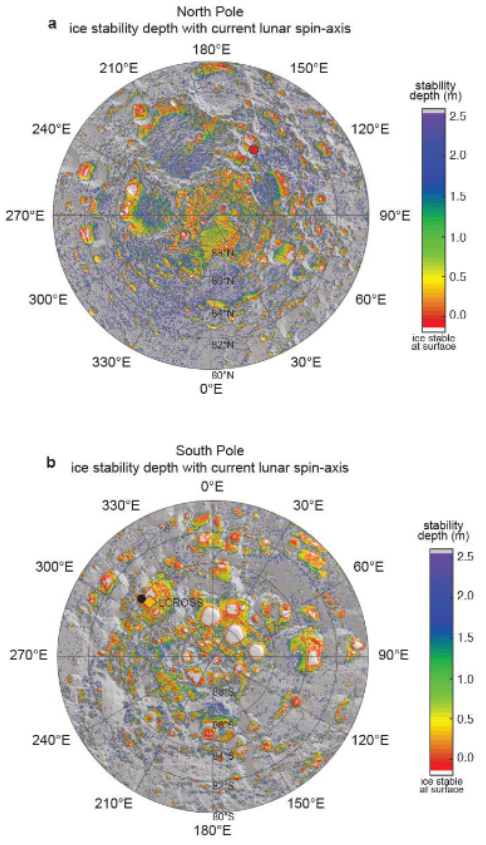

Figure 3.6: Model results for ice stability depth in the North and South Polar regions of the Moon [42].

polar wander, and previous to that event, were not able to capture and retain much ice. One example of this circumstance is Shackleton crater, located in the white square just at the south pole: in fact, this area was not a PSR in ancient eras [48], reason for which local ice reserves will probably be very scarce. Conversely, Cabeus crater, underlined by the white square in the upper left corner of the southern hemisphere pole map, is very promising regarding the abundance of ice deposits. This is because Cabeus is an ancient crater, hosting many large PSR, both during the paleopole and present-day pole eras [31], suggesting a continued presence of ice from ancient times to nowadays. Finally, the aforementioned data have been confirmed by the LCROSS impact mission [28], suggesting around 5 wt% as a reliable conservative estimate for the maximum amount of ice to be expected in high IFI widely extended ISR [31].

Finally, IFI values can be corroborated by thermophysical model for the depth of the ice stability region depending on local surface temperature [49]. Figure 3.6 shows a Lunar surface temperature model results for the Lunar south and north poles. Indicating the ice stability region depth for each area. Once again these results overlaps with high IFI areas, amounting to 28000 km^2, which correspond to the regions presenting surface temperatures lower than 100 K. When higher temperatures are considered, the total surface of the candidate sites for ice mining expands up to 240.000 km^2 [42], chiefly located near the aforementioned polar PSR, especially in the southern hemisphere, as illustrated by Figure 3.6, showing model predicted ISR depths based on past mission observation data.

3.2.2. Lunar water-ice ISRU techniques

Lunar ice ISRU operations can resort to a wide array of technologies using both mechanical and thermal techniques, both of which have their pros and cons. In case of mechanical extraction technologies, the excavated raw material, which can be composed by up to 30% ice mass, with the rest being regolith, must undergo a beneficiation process, i.e. the separation of valuable mineral resources from waste material. Beneficiation efforts can be of different nature: pneumatic, magnetic or electrostatic. The Aqua Factorem process [50] is an example of ice extraction process relying on mechanical techniques. Unfortunately, the Aqua Factorem, along with similar mechanical processes, requires an in depth characterization of the form of the ice deposits enclosed in the regolith. This is due to the fact that mechanical separation techniques efficiencies will depend on how the ice-regolith aggregated structure is formed. As today, there is limited knowledge of this aspect. In fact, ice content could be anywhere up to 30%, with lots of regional variation [51]. This is a great obstacle for the further development of such class of methods. Figure 3.7 illustrate the various steps of ice ore excavation, beneficiation and extraction, showing the mining rover along with the water cleanup and refinement facility.

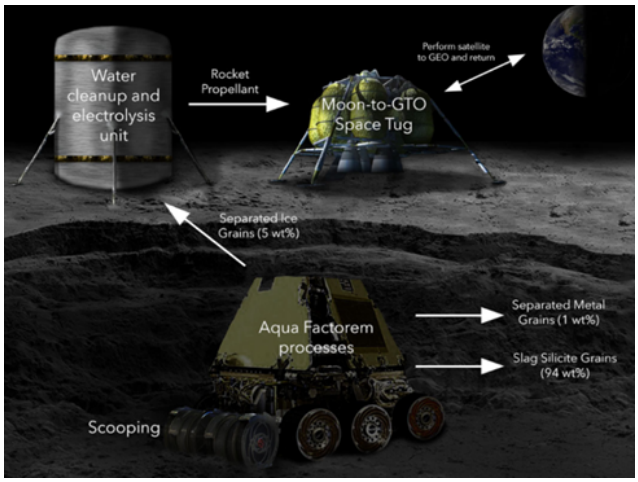

Figure 3.7: The Aqua Factorem architecture: mining rover plus refinement facility [50].

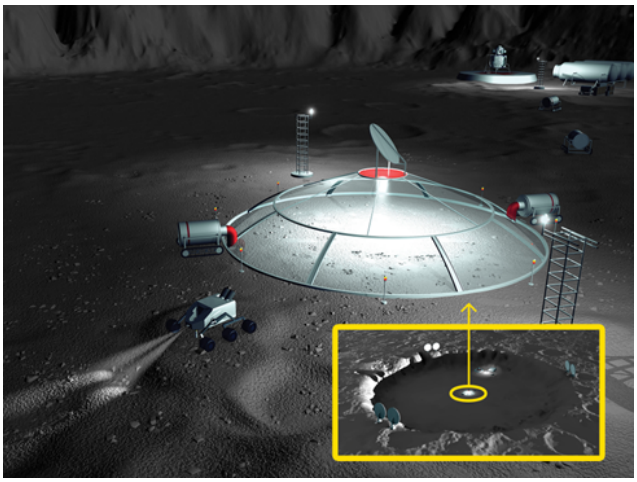

Figure 3.8: Large scale thermal mining concept, using heliostats on crater rims [52].

Thermal mining relies on heating up the regolith to provoke sublimation in the ice deposits beneath its surface. The water vapour generated is then captured by a cold trap, where it can refreeze. As the Moon does not have an atmosphere, all thermal mining efforts must be carried out in a contained environment to minimise volatile loss towards the void of space. The main criticalities of this alternative are the high thermal powers required and the fact a fraction of the extracted volatiles will refreeze in the areas adjacent to the mining site. On the upside, no excavation and beneficiation steps are needed, as the water vapour that refreezes in the cold trap has already been separated from the regolith.

There are multiple methods available to perform thermal mining, one alternative is to concentrate reflected solar radiation on a single spot through the use of heliostats [53]. An illustration exemplifying the concept can be seen in Figure 3.8, where heliostats focus sunrays from the constantly illuminated crater rim to a lens on top of a tent: the thermal mining sealed environment. Adjacent to the tent, lies the cold trap, where the water volatiles will deposit and ice will be collected. This solution features a high degree of complexity and necessitates of high mass launch capabilities. It would also require advanced robotic or human presence on site to build the heliostats on the PSR uneven crater rim, adding yet another layer of complexity to the endeavour [53]. Hence, this option is too onerous for the early stage of the development of Lunar ISRU capabilities.

Thermal mining can also be carried out on smaller scales, with the heat source and sealing equipment embarked on board of a rover, such as in the Ice-mining Lunar rover case. Under the current technological constraint, this option is of simpler realization, as a rover would pose much less delivery and logistical problems. Figure 3.9 illustrates two alternative options for a rover embarked thermal mining system. The first one is the use of homogeneous plate heating,

which requires a radiating heat flux of 1 kW/m^2 to achieve non negligible recovery rates [22]. The second one is to employ heater rods: mounted on a rover, they would be inserted inside the regolith with a drill and subsequently heated [54, 55]. Mining efficiency depends on rods number, grid density and power level, but the power required per rod to extract a non-negligible amount of water is a minimum of 1000 W, with configurations starting from 4 rods or more [22], requiring a very powerful heat source.

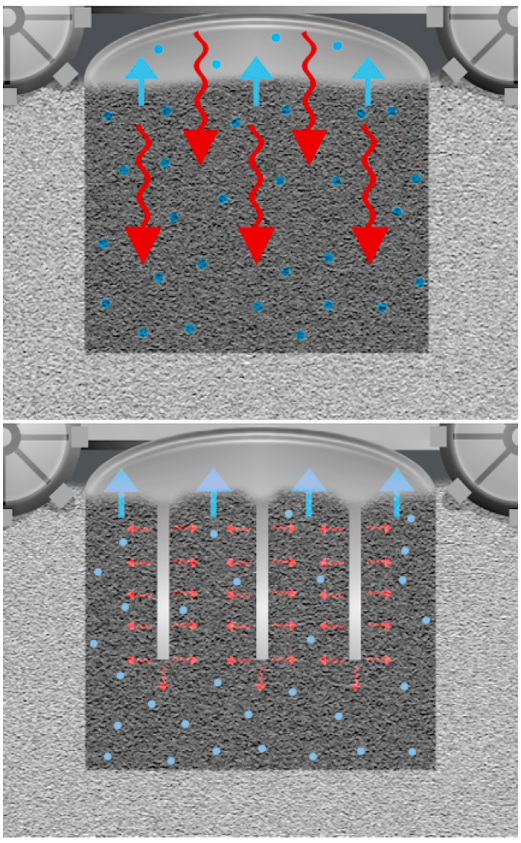

Figure 3.9: Homogeneous plate heating (top), vs. heated rods drilled inside the regolith (bottom) [22].

Thermal power could be drawn from the electrical power budget of the rover, through electrical resistances, or thanks to the heat generated by radioisotopes, both from Radioisotope Heating Units (RHU) or from the waste heat of an RPS. Due to the constraint of the PSR environment, it would be impossible to rely on Solar power, obliging designers to favour RPS systems as electrical and thermal power source. The high amount of thermal power required from the rod heating mining method disqualifies it in the majority of cases as a feasible alternative, leaving only surface heating. Finally, Surface heating has also been found more efficient that rod heating [22], with greater recovery values (ratio between the mass of the water extracted and the total water) against a much lower (at least an order of magnitude) heat consumption.

3.3. Power Systems required for ISRU

The necessary condition of Lunar thermal ice mining is the presence of a heat source. Hence, the role played by power systems employed for Lunar water ISRU is twofold: first, they must provide enough electrical power to run all the required instrumentation for the control of the extraction process, and secondly, they often provide the thermal energy heat source to sublimate the ice. In some cases, such source can be natural, as in the case of the sunrays concentrated on the extraction spot by heliostats, but in many others, it is man-made, and originates from the heat waste of the power system, or from the thermal to electric power conversion losses. This section will introduce two environment independent power systems, able to provide both electrical and thermal power in the sunlight deprived Lunar polar PSR: radioisotope power systems and fission reactors.

3.3.1. Radioisotope Power Systems

Radioisotope Power Systems (RPS) have been employed for electric power generation on spacecrafts since the dawn of the space era [56]. RPS function in a simple and straightforward way: the heat released by the decay of a radioisotope heat source is converted into electrical power that can be employed to power up the spacecraft subsystems, or accumulated in battery arrays.

RPS are extremely reliable power sources that constantly provide a continuous and stable power output, totally independent from the conditions of the environment surrounding the spacecraft. For this reason, RPS have been widely employed in planetary exploration missions whose destination lies at Jupiter and beyond, where the Sun becomes too dim, disqualifying Solar panels as a power source. New Horizons, Cassini, Ulysses, Galileo and the Voyager probes all equipped a RPS [56]. Furthermore, providing a stable and continuous power output can advantage the design process of an operative duty cycle, simplifying it and often reducing the need for large battery arrays. For these reasons, RPS are also widely employed on rovers. Mars Perseverance and Mars Curiosity rovers both host Radioisotope Thermal Generators (RTG) units, a kind of RPS, to provide electrical power to their instruments [57]. There are two important distinctions characterizing an RPS: the conversion technology to obtain electrical power from the radionuclide thermal power and the kind of radioisotope employed as fuel.

Radioisotope fuel choice

The radioisotope, or radionuclide, is the source of thermal power which is being converted into electrical power by the RPS. Radionuclides needs to be stable and of a coherent form. They are usually manufactured in the form of oxides or ceramics [58]. The radionuclide heat source is inserted into a multilayer containment system [58] with the aim of minimizing any risk of fuel dispersal in case of a launch failure. In the instance of ESA's developed Am-241 fuel based heat sources [58], the most internal cladding layer is made of a platinum 20%-rhodium alloy welded around the radioisotope to form a sealed container. The sealed container is equipped with a vent hole covered by a porous frit, studied to release the pressure increase deriving from the helium buildup from the radionuclide alpha decay, along with the additional release of oxygen by the high temperature Am-241 fuel module. Surrounding the cladding, an insulating layer can be found, enveloped in a carbon-carbon composite aeroshell.

The ideal RTG fuel is an isotope that must have the following characteristics [59]:

- High power density, so that a small amount can generate substantial quantities of heat;
- High temperature stability, so that its characteristics remain unchanged over many years;

- Long half-life, so that its power output remain stable along the mission lifetime;
- Present low or no chemical toxicity;
- Low neutron, beta and gamma emission which could interfere with S/C instruments, requiring massive shielding;

As already outlined, an important concern in the choice of a radioisotope is its type of decay, and therefore, the shielding required. Gamma emitters are extremely pernicious, since gamma waves are highly energetic, and can penetrate thick layers of shielding, interfering with on board systems and instruments. Furthermore, it is difficult to extract thermal energy from gamma rays, hence the thermal output of a gamma emitter isotope would be quite low anyways. Alpha emitters, on the contrary, require much less shielding, since alpha particles penetration capacity is modest, and are the best suited for heat transmission. For these reasons, only radioisotopes with dominant alpha decay have ever been considered.

After all the previously mentioned requirements have been fulfilled, a radioisotope is mainly chosen with a trade-off between two characteristics: half-life and energy density. A long half-life isotope is beneficial because it would provide a stable supply of power for a long time, and the difference between End of Mission (EoM) and Begin of Mission (BoM) thermal power output would be minimal, since only a small fraction of the isotopes could decay during the mission operative time. High energy density isotopes are also indicated because they can help reducing the total mass of the RTG assembly, merely by requiring less fuel mass to achieve the same power levels. Generally, shorter half-life means higher energy density, and vice versa.

Isotope	Radiation emission	Half-life	Specific power (W/g)
Plutonium-238	α, *low* γ	87.7 years	0.56
Americium-241	α, *low* γ	432 years	0.11

Table 3.2: RPS fuel candidate radionuclides [60].

Table 3.2 presents the two most suitable radioisotope fuel candidates. Pu-238 presents a long half-life and good isotopic power, it is not a strong gamma emitter and does not require shielding, since it almost totally follows alpha decay. Pu-238 has been employed as radioisotope fuel for all NASA's planetary mission from Voyager 1 to New Horizons, being used for probes as well as for rovers, it has also been employed on many Apollo missions [56]. The employment of Pu-238 derives from its strong heritage and historical reasons. In fact, although Pu-238 cannot be used in nuclear bombs, its brother isotope Pu-239 can: during the Cold War there were both in U.S.A. and U.S.S.R. many operative reactors producing weapon-grade isotopes and Pu-238 was available too, as a byproduct of the process. The availability of Pu-238 declined with the

end of the cold war, both in the U.S and in Russia, due to the dismissal of great part of the two superpowers nuclear arsenals. U.S. stopped Pu-238 production in 1988 [61], Russia sold NASA some kilograms of Pu-238, probably due to the depletion of its stockpiles [62]. In 2015, a new method of production involving the use of Neptunium-237 has been adopted [63]. Pu-238 will be produced at Oak Ridge National Laboratory, in Tennessee, with a projected output of 1.5 kg per year by 2026 [64].

Although Pu-238 production has been resumed in the US, its scarcity is felt dearly on the other side of the Atlantic. For the above reason, ESA is considering the employment of Americium 241 as radioisotope fuel. Am-241 has a half-life of 432.8 years, almost 5 times the one of Pu-238, while its isotopic power is 0.11 W/g, around 1/5 of Pu-238. It is a very weak gamma emitter, in fact almost 99% of the emitted energy is under the form of alpha particles [65], requiring thus very thin shielding. The extremely long half-life could enable century long exploration missions, even outside the Solar System, to the point that the limiting factor would become the other subsystems' components lifetime. This is counterbalanced by the lower isotopic power offered by the radioisotope. Such a drawback can be tolerated as even for a long mission, the difference between BoM and EoM power output would be marginal. The designer would not be obliged to oversize the system for the harshest condition (EoM), resulting in additional mass savings. In fact, considering a 20-year timescale (15 years nominal mission plus 5 years margin) the loss in thermal power output would be just 3.2% against 15% if Pu-238 were employed [66].

Am-241, in the chemical form of AmO_2, has a high melting point (2113°C) [67] and is acceptably stable. Am-241, unlike Pu-238, can be obtained by reprocessing nuclear waste from civil purpose reactors. UK National Nuclear Laboratory produces the Americium oxide material by chemically extracting it from the plutonium stockpile produced from reprocessed civil fuel, through the AMPEX process [68].

Conversion technologies

Once the choice of the radionuclide has been completed, the RPS designer must choose the heat to electrical power conversion technology. The two power conversion technologies alternatives are static thermoelectric and thermodynamical Stirling cycle based engine, although also Brayton cycle is being considered for dynamical power conversion [69].

Thermoelectric conversion is the most reliable technology between the two alternatives. Its reliability derives from the absence of moving mechanisms, eliminating a possible failure mode, Furthermore, this option has a rich flight heritage, being part of the first RPS powered American satellite, launched in 1961 [56]. A wide selection of thermoelectric materials, such as silicon-germanium (SiGe), lead telluride (PbTe), tellurides of antimony, germanium and silver (TAGS), and bismuth-telluride (BiTe) has been made available during the long history of development of

this technology. While some of these materials can operate both in atmosphere and in vacuum, most of the heritage technology (SiGe thermoelectrics) has been designed to operate only in vacuum. However, this is not of concern, as the Lunar atmosphere is almost nonexistent and could not pose any threat to a thermoelectric RPS. Two other points of merit of a thermoelectric conversion RPS would be the easy and cheap scalability, resulting in enabling a very convenient tailoring of the RPS size to the spacecraft or planetary rover power requirements if there ever were the need to do so, and the complete absence of vibrations during its operations [56]. Finally, thermoelectric technology can convert thermal energy into electrical energy with system efficiencies exceeding 6% [56]. A very successful RPS employing thermoelectric conversion technology is the MMRTG Multi-Mission Radioisotope Thermal Generator (MMRTG) [70], shown in Figure 3.10. The MMRTG employs as thermal sources 8 General Purpose Heat Sources (GPHS), a standardized radioisotope heat source, to meet the needs of a specific mission.

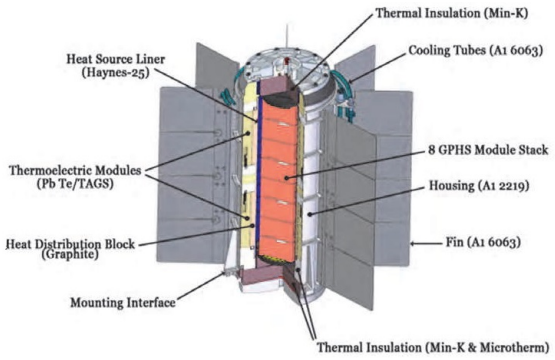

Figure 3.10: The Multi-mission Radioisotope Thermoelectric Generator (MMRTG) [60].

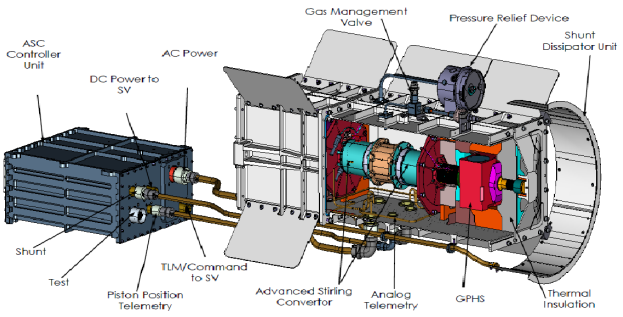

Figure 3.11: The Advanced Stirling Radioisotope Generator (ASRG) [71].

On the other hand, Stirling engine conversion has characteristics which are opposite to thermoelectric conversion. It is not as reliable as the thermoelectric alternative, as there are moving parts which add complexity to the system, and also has no flight heritage, as it is a newer technology. A dynamic conversion system would also be less readily scalable, and it would transfer some vibrational loads to the spacecraft. Its major merit is a much higher conversion heat to electrical power efficiency, ranging from 20% to 30%. Being the conversion more elaborated, its efficiency depends on various factors. The most influential are thermodynamic cycle convertor efficiency, depending on the heat load and the cold side temperature. Other important aspects are the AC-DC convertor efficiency, usually estimated as 90%, from typical components, and convertor control parasitic power, which is generally ∼10 W, based on standard controller hardware performances. As a mean of comparison, NASA Advanced Stirling Radioisotope Generator (ASRG), shown in Figure 3.11, can achieve an efficiency of 26%, although it uses Pu-238 instead of Am-241 as radioisotope [72]. Currently, the ASRG program has been scrapped and replaced with the Dynamic Radioisotope Power System program [73].

ESA is also recently developing a European alternative to NASA Stirling cycle based RPS: the European Radioisotope Stirling Generator (ESRG), whose breadboard model is reported in Figure 3.12. It will be powered by Am-241 instead of Pu-238 and it targets an electrical power output of 100 W at 28 V, springing from a thermal power input of 435 W, with an efficiency of 23%, a total predicted mass of 66kg and specific power figure of 1.51 W/kg [74].

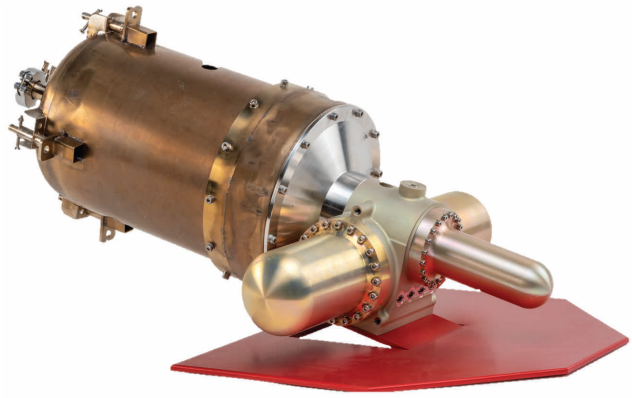

Figure 3.12: The ESRG breadboard unit [74].

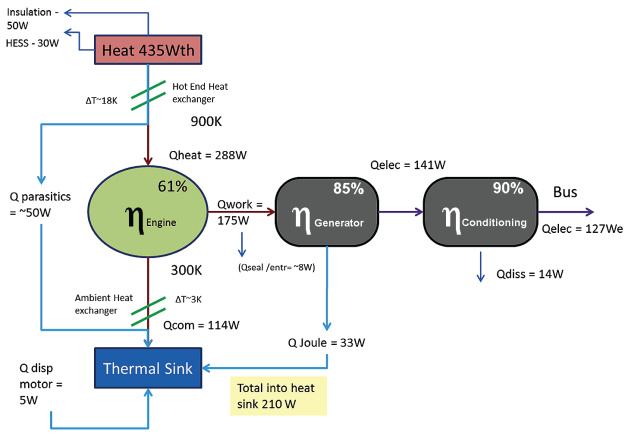

Figure 3.13: A schematic of the ESRG heat flow [74].

Figure 3.13 illustrates in detail the heat flow from the Am-241 source through the various steps of thermal to electric power conversion process, detailing the amounts of electric power produced, along with the heat-waste dissipated by the radiators and many undesired parasitics heat transfer pathways and other unwanted losses.

3.3.2. Fission Reactors

As already mentioned in subsection 3.2.2, Lunar ice ISRU thermal mining requires large amounts of heat to sublimate the ice deposits. Furthermore, once the initial phase of exploration Lunar high IFI PSR craters will have been carried out and large deposits have been prospected for, thermal mining operations could be freely scaled up to met water and cryogenic propellant demand. In this future advanced phase of commercial utilisation of the Moon natural resources, monetary budget constraints will not be a limiting factor to ISRU activities, as the mining expenses would be certainly backed up by the revenue obtained by selling the extracted resources. Hence, given the larger power budget demands, a future increase in the scope and magnitude of ice mining operations could only be bolstered by nuclear fission reactors.

Small scale nuclear fission reactors specially conceived for space use exist with a wide variety of designs. They are also called Surface Power Systems and will play a pivotal role not only for ISRU operations as they could also be employed to support Lunar and Martian human habitats. The anticipated power output for Lunar ISRU operations will depend on their scope

and magnitude: a NASA study is considering an escalation in 3 steps, with the aim of deploying a sequence of reactors that would supply increasing amounts of electrical and thermal power for a growing ISRU presence on the Lunar surface [75]:

- The first small scale nuclear fission reactor to be deployed would be part of a pilot ISRU plant operation, requiring only 10 kW_e to function;
- The subsequent mission would involve a preliminary ISRU production plant comprising of a human habitat, for an electrical power budget up to 50 kW_e ;
- The last and final mission would be fully fledged ISRU production plant, also comprising of a permanent human outpost, for an overall power requirement of 500 to 2500 kW_e;

Conversion technologies and reactor types

Nuclear fission reactors for surface power applications can be either fast spectrum, where the fission chain is sustained by fast neutrons, carrying energies of 1 MeV or grater, or moderated, in which fast neutrons from a previous fission event are slowed down to the thermal energy range by a moderator before causing another fission event [76]. The reactor core maximum temperature, from which the nuclear fuel choice depends, is driven by its construction material.

A stainless steel reactor would allow a maximum core temperature of 900 K, limiting the nuclear fuel choice to UO_2 or UZrH. The employment of refractory alloys based on niobium, tantalum or molybdenum, could raise core operational temperature to 1300 K, allowing the utilization of UN and UO_2 [76]. Although there are concerns over the long term material performance of refractory alloys, their use would result in a greater power conversion efficiency, diminishing heat waste magnitude, allowing for smaller radiators and an overall lighter mass compared to the stainless steel design. The reactor cooling technologies, also considered the high temperatures at play, could be either liquid metal cooling, gas cooling or heat pipe cooling [76]. Finally, the thermal to electrical power conversion alterna-

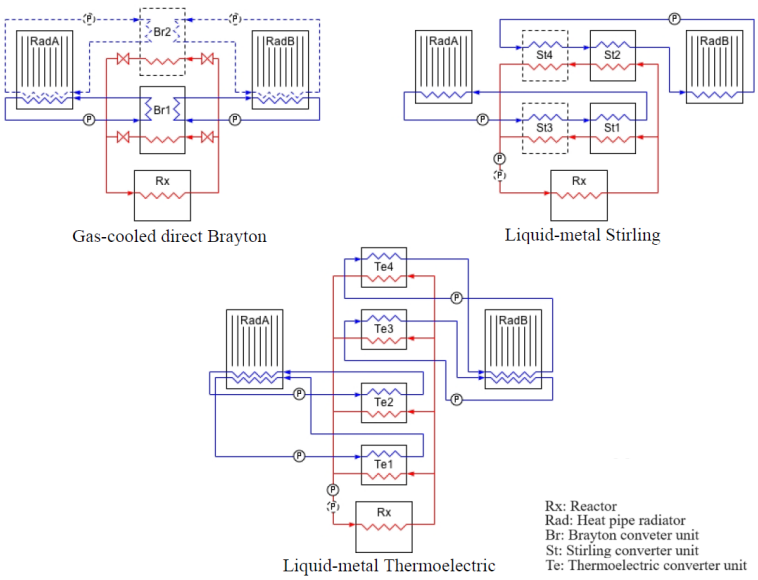

Figure 3.14: Nuclear fission Surface Power System architectures based on three different conversion technologies and cooling method combinations. Dashed lines indicate redundant converters, fluid loops and pumps [76].

tives, whose architectures are presented in Figure 3.14, can be based on Brayton or Stirling cycles, or on thermoelectric effect [76]. All the reactors that are going to be mentioned have been designed with a reference power level of 50 kW_e, although they could be scaled for a range of power outputs starting from 25 to 200 kW_e. Finally, great importance has been given to reliability, as maintenance is extremely impractical due to the high radiation level and hostile operative environment: all the designs will be highly redundant, at least single failure tolerant, employing additional converter units than actually needed, so that all of them will not need to work at full regime under nominal circumstances [76].

Gas cooled direct Brayton concept The gas cooled direct Brayton is directly derived from the Jupiter Icy Moons Orbiter (JIMO) spacecraft, proposed by NASA in the early 00's, but never launched [77]. As shown in the upper left portion of Figure 3.14, it uses two identical converter units, even as only one would suffice for producing the nominal power output. In fact, the two convertors are operated at 50% of the generator rated power, so that if one of them malfunctions, the remaining one can be put to work at full regime, still guaranteeing the same power level as per design specifications. The system, like all the other ones, comprises of two heat pipe radiators. The reactor is gas cooled, with a mixture of helium and xenon transporting the heat from the reactor to the Brayton turbines. The HeXe working fluid is heated directly in the reactor core and exits from it at the temperature of 900 K in the stainless steel version. If refractory materials are employed, this temperature is increased to 1150 K, which is the maximum operating temperature for the turbine super-alloy blades [76]. Heat is then dissipated from the converters to the heat pipe radiators through a water based pumped fluid loop. Each converter is initially connected to a different radiator. A series of backup connections is installed between the converters and the radiators, so that full operational capability is maintained even in the unlikely case of radiator breakdown [76].

The liquid-metal Stirling concept The liquid-metal Stirling concept employs 4 converters in 2 serial pairs. Only two of them are required for nominal power operations. The serial configuration is beneficial as the second Stirling converter of each pair is working at a lower temperature, hence can have a longer operative life, being subject to lower stress, such as creep [76]. The reactor coolant loop, being liquid-metal based, necessitates of redundant annular linear induction pumps to function. If the reactor main material is stainless steel, sodium-potassium (NaK) is utilized as coolant: the reactor exit temperature is 900 K and the Stirling hot head temperature is 850 K. Conversely, for the refractory super-alloys based generator, lithium is used as coolant: reactor exit temperature will be 1100 K and Stirling hot end temperature will be 1050 K [76]. Heat is transported from the Stirling engine cold end to the water heat pipe radiators by a water based pumped fluid loop for the low temperature design. NaK is instead employed for the high temperature version of the generator. This architecture can

tolerate maximum 2 converter unit failures without impacting power production, although even one failure in a radiator loop would result in 50% power output reduction [76].

Liquid-metal Thermoelectric concept The liquid-metal thermoelectric architecture makes use of 4 converter units in parallel with each others. No redundancies have been implemented for two reason, the first being that is very difficult to operate thermoelectric modules in off-design mode, the second being that such modules, not having moving parts, are already very reliable. Furthermore, each module is subdivided into a series of thermoelectric couples intimately connected by an intricate network of series/parallel connections, with enough built-in redundancies [76]. Once again, as the reactor is liquid-metal cooled, redundant annular linear induction pumps are necessary to recirculate the coolant fluid. The reactor exit temperature and the thermoelectric unit hot shoe temperature are 900 K and 850 K respectively, with the coolant being NaK, for the stainless steel option. In case of a refractory material design, the previous temperatures are increased to 1300 K and 1250 K, and the coolant is lithium. The thermoelectric cold shoe temperature is too hot for a water based radiator coolant loop. Hence, for the stainless steel design, NaK must be used as a radiator coolant, coupled with cesium heat pipes. Conversely, the hotter temperatures of the super-alloy based design dictate the use of lithium radiator coolant and cesium heat pipes [76]. In both designs, two thermoelectric converter units will be coupled to each radiator through an independent coolant loop [76].

Reactor shielding options

Two shielding options can be considered for the fission reactor: excavation shielding with on site materials and Earth delivered shielding. They are illustrated in Figure 3.15.

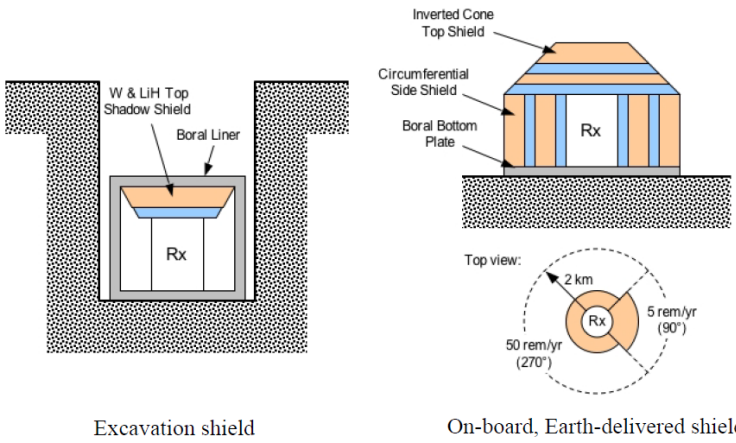

Figure 3.15: The two reactor shielding architectures [76].

The excavation shield option is the best one in terms of system mass, as the regolith will screen the greatest part of the radiation without the need for massive shielding to be brought from Earth. The downside is the requirements of construction and excavation equipment, a favourable topology and, most likely, crewed assistance. The reactor would be placed at the bottom of a vertical excavation. On top of it is present a conical shadow shield, manufactured in tungsten and lithium hydride, which screens the converter units and radiators, located outside the depression hosting the re-

actor. A 2 cm thick boron-aluminum (Boral) liner encases the whole reactor, in order to absorb neutrons, providing a safeguard against neutron back-scatter. This shielding configuration is extremely effective in controlling reactor emitted radiation, reducing the radiation dose to 5 rem/yr at a distance of just 6 m from the reactor ceterline [76].

The Earth delivered shielding, conversely, is the easier option with regards to the reactor installation procedure, but comes with added mass and has a higher radiation emission. The shielding apparatus is an inverted cone top shield, plus a circumferential side screen. As in the previous shielding approach, a Boral liner is required to avoid neutron back-scatter in the regolith under the reactor. In order to save mass, shielding is increased over a portion of the side circumferential shield amounting to a 90° view, reducing radiation to the safety level of 5 rem/yr at a distance of 2 km. This will be the direction of the habitat and ISRU facility location. The rest of the shielding, is sized to limit radiation to 50 rem/yr at 2km distance, making it an hazard to carry out crewed operation in the area [76].

Finally, a hybrid shielding approach could be devised on a case by case basis, using local topological features, natural reliefs and depressions to reduce Earth delivered screen mass [76].

Waste heat management technologies

In all the three aforementioned designs, the waste heat from the converter units must be dissipated to space. This task is managed by a pumped fluid loop which transports the waste heat from the converter to the heat pipe radiators, in an arrangement similar to the JIMO mission concept [78]. Figure 3.16 shows the interface between the pumped fluid loop and heat pipe radiator, along with some features from both systems.

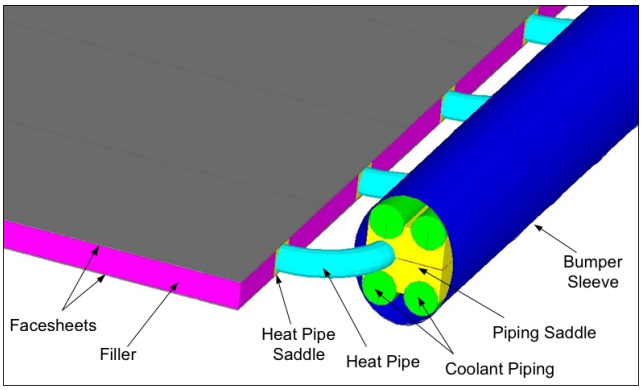

Figure 3.16: Pumped fluid loop interface with the heat pipe radiator panel [76].

The pumped fluid loop cold end transfers its waste heat to the radiator's heat pipes evaporators, which are bent at 90° with respect to the rest of the heat pipe. The heat pipes evaporators are thermally integrated with the pumped fluid loop by a high conductivity graphite saddle [76]. The external bumper sleeve, made of a thin shell of composite material, is designed to provide structural integrity and meteoroid impact protection. Heat pipes flow parallel along the radiator length, their linear density is the result of a trade-off between fin effectiveness and panel mass. The heat pipe condensers, which run all along the radiator, are encased in a graphite saddle, which acts as supporting structure, while both the coolant loop and the heat pipes en-

velopes are made of titanium. All the heat pipes are sandwiched between two high conductivity composite facesheets [76]. Finally, a lightweight porous carbon based filler material is present between the heat pipes, because of structural considerations [76]. Radiators dissipate heat by irradiation to deep space. They present a high emissivity low absorbivity surface finish, as in the case of many thermal control paints. Radiators are sized with equatorial lunar noon as worst case condition. They are oriented vertically to the Lunar terrain, doubling the available radiating surface, as the radiators can reject heat from both sides. In this configuration radiator sees a portion of Lunar surface, for an equivalent sink temperature of 317 K [76].

Case study: the Kilopower

The fission reactors that have been introduced in the previous pages are still presenting both a very large nominal power output and heavy system mass: as an example, the lightest design among them is a 25 kW_e refractory alloy based, gas-cooled Brayton reactor, with in-situ shielding, for a total mass of 4200 kg [76]. This makes them unsuitable for a range of intermediate power applications, especially the ones required by the still in development state-of-the-art ISRU technologies. Current radioisotope power systems developed by NASA can address power requirements up to 1 kW_e, while fission reactor can provide power outputs starting from 10 kW_e. For such reason, NASA has filled the gap in its power system portfolio with the development of the Kilopower [80], which could be used both in nuclear electric propulsion (NEP) surface power systems [81]. In the first design, the Kilopower requirements are to host an operating reactor at the steady state temperature of 800 °C, with a 4 kW_{th} thermal power output converted to 1 kW_e by multiple Stirling engines working in parallel. To meet the higher power requirements of an early stage Lunar ISRU mission, NASA is planning to increase the Kilopower electric power output up to 10 kW_e, requiring around 40 kW_{th} [82].

The Kilopower, as shown in Figure 3.17, can be divided in two parts, one on the hot end of the Stirling convertors and the other on their cold end. The hot end is composed by the nuclear reactor and by

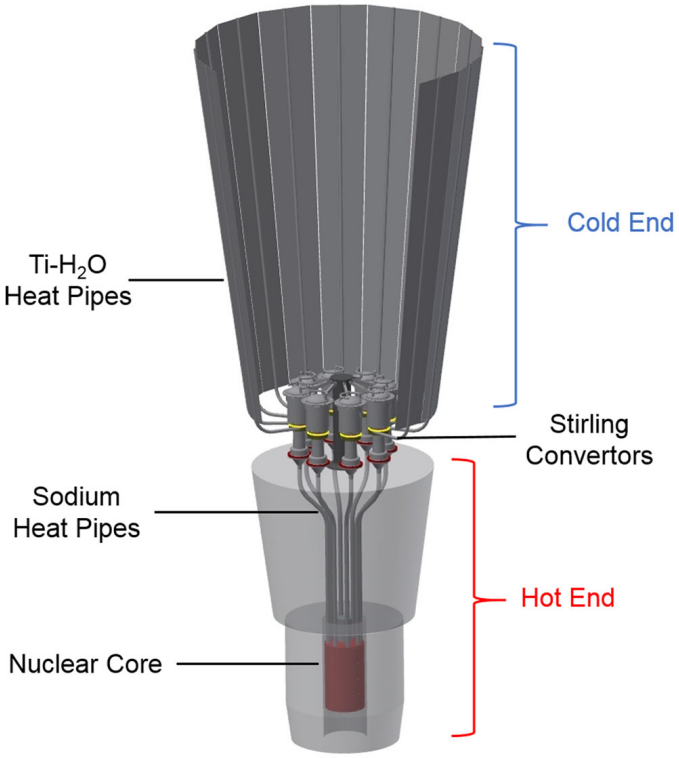

Figure 3.17: The Kilopower conceptual design and its thermal management system [79].

high temperature sodium heat pipes tasked with the reactor cooling. The sodium heat pipes are connected to the converters hot end. On the other side of the Stirling engine, water-titanium heat pipes transfer the waste heat from the converter cold head to a radiating surface which will dissipate it through irradiation into deep space [79]. Water-titanium heat pipes have been chosen for their higher operational temperature, their capability to work even without gravity assistance, and the large quantities of heat they can transfer, which amount to 125 W per heat pipe in nominal conditions, raising up to 250 W during transients [79]. Water-titanium heat pipes also are the best suited choice to adapt to a variety of scenarios and varied working conditions, among which are zero gravity space operations, microgravity operations, with slight adverse gravity conditions, planetary surface operation with gravity aid and start up after launch, after being exposed to launch conditions.

The heat pipes will be equipped with an innovative bi-porous screen evaporator, which presents a C-shaped interface to facilitate the heat exchange between the Stirling assembly and the heat pipe. The adiabatic and condenser section, will have an axial groove structure to facilitate liquid return during space operations [79]. The heat pipes will present a 82° bending to accommodate for the radiator geometry as in Figure 3.17.

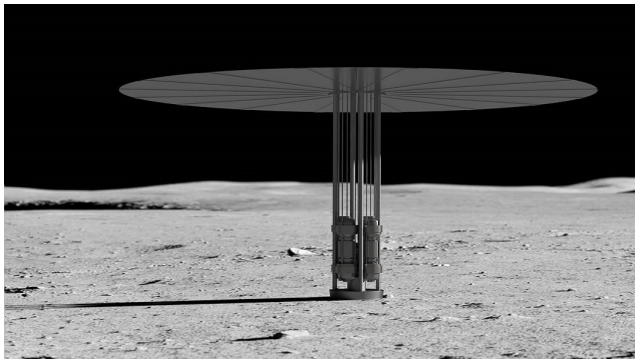

Figure 3.18: Illustration of a conceptual fission surface power system on the Moon, based on the Kilopower design [82].

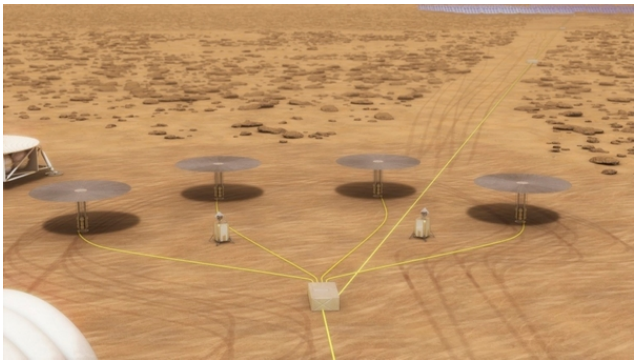

Figure 3.19: fission surface power concept utilizing multiple 10 kW_e units to provide 40 kW_e of power on the Moon or Mars. [83].

Finally, NASA plans to exploit and develop the Kilopower design to power up its earliest stage of human mission on the Moon and Mars. Figure 3.18 shows a Kilopower inspired Fission Surface Power system on the Moon, providing 10 kW_e of power, enough for a small habitat and pilot ISRU plant [82]. The output of multiple Kilopower reactors could be joined together to scale up in operation magnitude, like in Figure 3.19, where four systems similar to the one of the previous image are all connected to the same PMAD station, for a joint power output of 40 kW_e [83].

3.4. Mars and Lunar rovers

This section is going to discuss examples of past rover missions to the Moon and to Mars, along with mission concepts currently being developed. The scope of this section is hence to gather high level data about planetary rovers, such as masses, volumes, locomotion and thermal control architectures, power budgets, other subsystem related information and rover operations. The information will be used as a baseline for the rover TMS design and to perform tradeoffs.

Although the proposed ice-mining Lunar rover is going to operate in the cryogenic environment of the Moon PSR, Mars rovers have also been considered to increase the pool of available baselines. Martian rover present some specific adaptations to the Martian environment, such as the presence of an atmosphere, enabling convection as a possible heat transfer way and the possibility of strong winds. Lunar rovers do not have to address this problems, as there is no atmosphere on the Moon. In both environments, but especially on the Moon, the dust poses great problem to the survivability of geared subsystems. Lunar regolith dust is extremely fine and has very good insulating properties. It can very easily deposit on concave surfaces, or even radiators, altering their emissivity properties, as it happened to the Lunar rover Lunokhod 2.

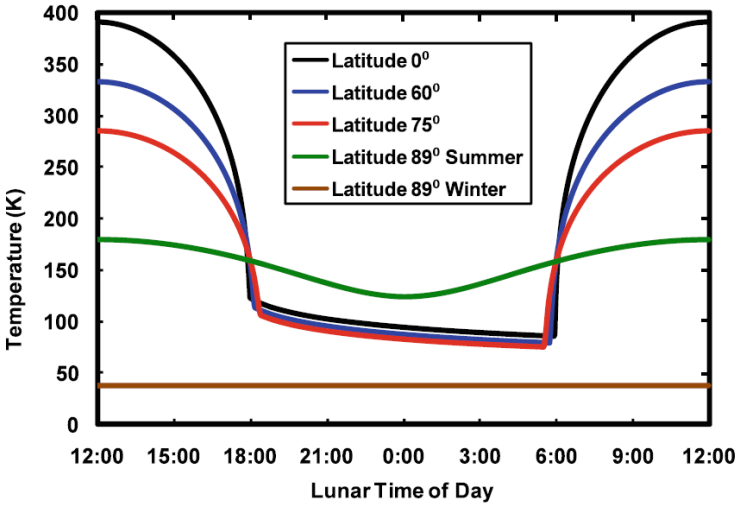

Figure 3.20: Lunar temperature model results based on LRO Diviner Lunar Radiometer Experiment. Time expressed in Lunar hours, corresponding to 1/24 of a Lunar day (28 Earth days). Temperatures at the poles calculated at solstices [28].

The absence of an atmosphere causes high temperature excursions between the Lunar day and night: at equatorial latitudes temperatures can drop as low as 100 K during the night and raise as much as 400 K during the day [28]. At the poles, on the other hand, they can be as low as 30 K during winter and not surpass 180 K during summer, as illustrated in Figure 3.20. According to the scientific objectives and engineering requirements of the exploration mission, some rovers have been designed to withstand a cold Lunar night, while some others have their operative time reduced to 14 days (the duration of half a Lunar sol). No rover has instead been directed to Lunar polar PSR, where cryogenic temperatures are one of the greatest challenges for the vehicle design, even thought a few missions will attempt such feat in the near future.

3.4.1. Mars rovers

Many exploration vehicles have already roved on Mars surface, here some of their designs will be introduced. Both flown missions and design studies will be presented.

Sojourner and Rocky VII

Sojourner is the first wheeled vehicle to have ever successfully rove on Mars. Developed by JPL, it had the scientific objective of studying the Martian geology and the technical objective of demonstrating roving capabilities on Mars. Mars Pathfinder landed on Mars on the 4th of July 1997. Sojourner, shown in Figure 3.21, is a very light rover, weighing only 11.5kg. Its dimension when fully deployed are 65cm length by 48 cm width by 30 cm height, with a ground clearance of 15 cm and a stowed height of 19 cm. It relied on solar panels and batteries to power up its operations [85]. Rocky VII, the immediately previous design iteration of Sojourner [85], is closely related to its slightly more advanced brother: it was intended to have each motor drive a couple of wheels [86], instead of each wheel having its independent motor like Sojourner [85]. Sojourner, shown in Figure 3.21, is a very light rover, weighing only 11.5kg. Its dimension when fully deployed are 65cm length by 48 cm width by 30 cm height, with a ground clearance of 15 cm and a stowed height of 19 cm. It relied on solar panels and batteries to power up its operations [85]. Rocky VII, the immediately previous design iteration of Sojourner [85], is closely related to its slightly more advanced brother: it was intended to have each motor drive a couple of wheels [86], instead of each wheel having its independent motor like Sojourner [85].

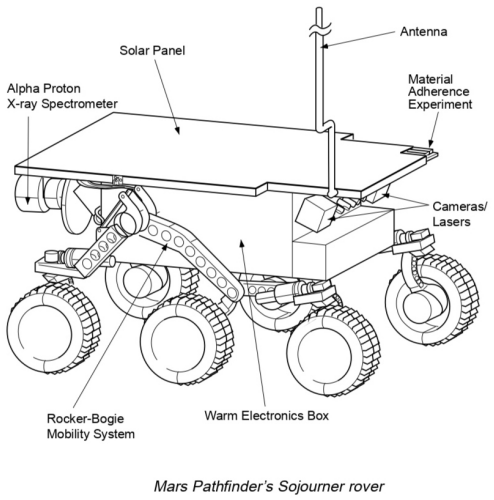

Figure 3.21: Sojourner rover [84].

Mobility Sojourner has a 6-wheeled rocker boogie suspension system, derived from the Rocky series. This allows the vehicle to traverse obstacles with more than a wheel diameter in size. The wheels are made of aluminium with stainless steel cleats, each one is independently actuated by a Maxon RE016 motor [85]. The power required to operate at -80°C is less than 8.5 W, while it can be lowered to 2 W at 0°C. The nominal speed on plain surface is 0.4 m/min [85].

EPS The rover is equipped with 0.2 m^2 GaAs solar panels which, at mid-sol on a latitude of 19.5° N, results in a peak power of 15 W and an average energy production of 104 Wh/sol. The EPS is backed by 9 LiSOCl2 primary battery packs, providing up to 300 Whr of energy [85]. Auxiliary battery power can double the solar panels peak power output. All on board

processes, comprising of CPU, will be turned off during night time, with the exception of the alarm clock routine, and WEB heating, provided by the batteries [85].

TCS The main engineering challenge to be overcome by the TCS was the survivability of the rover during the cold Martian night, with temperatures as low as 160 K. Components not designed to withstand the night have been located inside the Warm Electronics Box (WEB), which insulation is made of solid silica aerogel [85]. The outside of the WEB is wrapped in a high emissivity gold coating. The WEB is kept in the operative temperature range (from -40°C to +40°C) by a combination of 3 Radioisotope Heating Units (RHU), providing 2.925 W of thermal power [87], electronic waste heat and computer controlled resistive heaters. Thermal losses per Martian day are required not to exceed 2 W beyond the RHU heat output, equivalent to the 50 Wh/sol energy allotted to the resistive heaters by the electric power budget [85]. No thermal control is applied outside the WEB, apart for 1.2 W resistive heaters on the wheel motors. This is necessary to bring the motors at operating temperature before start-up [85].

The small rover Sojourner, although one order of magnitude lighter than the projected mass of ice-mining Lunar rover, is still interesting from a mass and power budget standpoint, as it is able to perform essential tasks with a very light body and a meagre power budget. The WEB is also a widespread thermal control architectural choice that can be taken as a baseline.

Spirit and Opportunity (Mars Exploration Rover A and B)

Spirit and Opportunity are two twin rovers, designed by JPL and operated by NASA, which landed on Mars in January 2004. They are also known as Mars Exploration Rover (MER) A and B. The scientific objective of the two rovers is to discover if Mars could potentially host life, and, if not, whether there had ever been such conditions in the past. The mission also had the technological objective to demonstrate long-range traverse capabilities [88]. Each of the two MER vehicles has a mass of 176.5 kg, the wheelbase is 141 cm long and 122 cm wide, while at the height of the deployed solar panels the rover is 151 cm long and 225 cm wide. The rover hosts a mast, on top of which a suite of imaging and surveying instruments take advantage of the 154 cm height over the Martian soil, which grants a wider view over the surrounding area [88]. Figure 3.22 is a computer graphic rendition of how the MER rover should appear on Mars.

Mobility One of the mission requirements for the MER rovers is to drive for at least 600 m over the 90-sol [88], hence mobility system performance an influential drivers in the rover design. The rovers are two 6-wheel drive, 4-wheel steer vehicles employing a rocker bogie suspension system derived from Sojourner [89]. The Aluminum wheels have a diameter of 26 cm, with cleats to develop traction in sandy terrain [89]. All 6 wheels are provided with autonomous motors, while the front and rear couples also have steering capabilities, provided by Maxon engines. They can survive night time temperatures lower than -55°C, but need to be heated up

before operations [88]. The suspension system directly derives from the Rocky series, together with a differential, the rocker bogie suspensions allow for all the wheels to keep contact with uneven terrain. The distribution of mass along the rover has been studied so to allow for 45° tilt without overturning risk. The top speed of the rover on flat hard terrain is 4.6 cm/s, but under autonomous drive with hazard control active, the speed averages at less than 1 cm/s [89]. The highest power required by each one of the six motors under maximum load conditions is 56 W, requiring 2 A of current at 28 V [89].

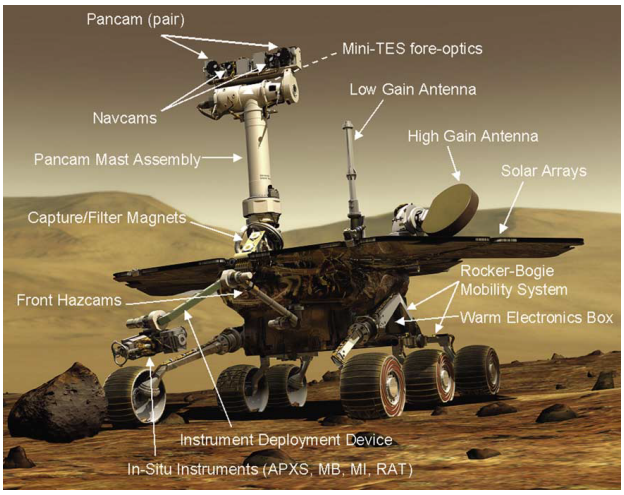

Figure 3.22: The MER rover [88].

EPS MER is powered by solar panels, in combination with Li-ion secondary batteries. The triple junction cells based solar panels, with a total surface of around 1.4 m^2, produce about 900 Wh per sol at BoM and 600 Wh per sol at EoM [88]. Energy storage takes place in two 8 Ah Li-ion secondary batteries that can provide 400 Wh of energy to power up peak power usage operations, such as intensive roving or WEB heating. The power system has been designed with the aim of guaranteeing the following operations: wake-up, routine data sampling, rover status evaluation, communication through X-band DTE for 1 hour and through UHF with orbiters twice per day, shut down, night time survival and heating. The operations will consume 430 Wh of energy out the 600 Wh produced at EoM [88], so that the remaining portion could be used for roving and science.

TCS Temperature sensitive components are housed in the WEB, which is insulated by 2.5 cm of opacified aerogel. The temperature inside the WEB is controlled by RHUs, electronics waste heat and auxiliary heaters. The allowable temperature range inside the WEB is between -40°C and +50°C, while the external environment ranges from -97°C to 0°C. No more than 100 Wh of battery energy the batteries can be dedicated to night-time heating [88]. The minimum working temperature of the wheel motor is -55°C, so special heaters have been installed to enable preheating before operations [88].

Spirit and Opportunity have been a great advance over their predecessor Sojourner, featuring a great increase in mass and power budgets. Due to their mass and dimensions, they are a more suitable baseline than Sojourner for the ice-mining Lunar rover, especially for the TCS.

Curiosity and Perseverance (Mars Science Laboratory and Mars 2020)

Curiosity, landed on Mars in 2012, and Perseverance, landed in 2021, are the latest design of rovers on Mars up to this date. It is part of the Mars Science Laboratory (MSL) mission.

Curiosity and Perseverance are massive rovers: 2.8 m width, 3 m length, 1.1 m top deck height and 2.2 m total height. The former weighs 899.2 kg, while the latter 1025 kg [90]. The requirements for MSL, whose image is shown in Figure 3.23, are traversing at least 100 m per sol, processing data at high speed, storing and broadcasting them with an X-band DTE or via UHF through orbital relay. Curiosity is equipped with an MMRTG [90], providing a constant stream of power unregarding of environmental conditions. The employment of the MMRTG is a major difference with the previous Mars rovers, which all relied on solar panels. Operative schedules has been revolutionized as power demanding operation can now also be conducted at night. The downside is the need to manage the large amount of waste heat, both on Mars surface and during the interplanetary travel. The nominal mission duration is one full Martian year, or 669 sols, equal to 687 Earth days. The rover scientific objective is to study Mars habitability and to clear the way for future human explorations endeavours [90].

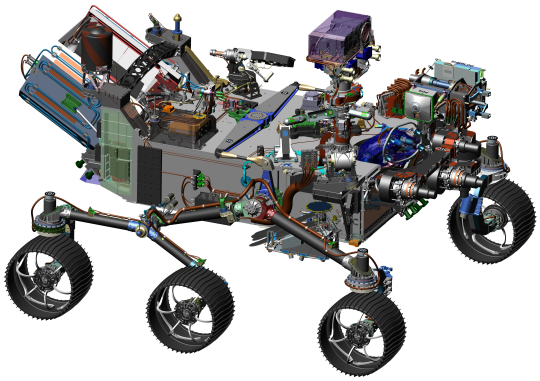

Figure 3.23: Mars 2020 CAD drawing [91].

Mobility The rover mobility system is 6-wheel drive, 4-wheel steer, rocker boogie suspensions, heritage from previous missions The wheels are all cleated with autonomous driving capability, their diameter is 50 cm. The clearance from ground is 66 cm. It can withstand a static tilt up to 50°, reduced to 30° while driving. The maximum speed on flat hard terrain is 4 cm/s, reduced to an average of 1.5 cm/s under autonomous hazard avoidance driving regime [90].

EPS The MMRTG is able to generate up to 110 W_e at BoM, peak power requirements exceed the RTG output and are managed by two Li-ion rechargeable batteries with a capacity of 42 Ah, which are expected to go multiple charge/discharge cycles per sol. To safeguard battery life, the arrays have been oversized so that depth of discharge will not exceed 60% [90].

TCS The operative and survival temperature ranges for the rovers are similar to the previous missions ones, so similar solutions have been devised. An addition is the presence of a Remote-WEB, positioned on top of the mast, encasing Navcams and P/Ls. The heat from the MMRTG must be radiated away to avoid overheating, but it could also be used to heat heat up various components, especially during the night. The MMRTG is encased in a double walled shell, where the inner and outer surfaces are separated by a paraffine actuator, which acts as a heat switch. Heat is gathered from the inner radiator, called hot plate, which has the objective of absorbing the heat waste from the RTG. From the hot plate, the heat can flow to the cold plate, which radiates the heat away from the rover, or can be collected by a sophisticated pumped fluid loop composed of more than 60 m long piping, and directed where needed [92]. This

design alleviates the need for survival heaters in the WEB but it can be made possible only thanks to the large mass and power budget of the rover, which allows for a pump and all the tubes to be installed on board [93].

Curiosity and Perseverance present considerable mass and large power budgets which are far too large to be considered as baselines for the ice mining rover. Nonetheless, the RPS integration with the rover can provide interesting insights for the Ice-mining Lunar rover.

MarsFAST

MarsFAST is a Martian rover design feasibility study conducted in 2014 by ESA's Concurrent Design Facility at ESTEC. The study aimed at characterizing a 150 kg class rover synergizing with a potential Mars Sample Return future mission, but also at demonstrating "FAST" mobility performance requirements [94]. MarsFAST objective is to traverse at least 15 km in a maximum of 110 sols, without the support of radioisotopic material for either power generation or thermal control [95]. Apart from technology demonstration, the rover will also perform in-situ science in support of a future Mars robotic exploration [95]. The contract with NASA for the landing services mandates a maximum stowed volume of 148x95x55 cm and mass of 200 kg, considering both rover and egress system [95]. Figure 3.24 shows the MarsFAST rover before egressing from the lander. The rover has an envelope volume of 116x91x53 cm when stowed, and 231x181x144 cm when deployed. The rover final mass, comprising of 20% margin, is 156.1 kg, with 15.3 kg of P/Ls. The egress system margined mass is 21.9 kg MarsFAST design main drivers are: fast and long distance mobility, absence of RHU for components heating, DTE telecommunications capabilities limited to 5 minutes in worst case scenarios and Survival for up to 14 sols during dust storms, in hibernation mode [95].

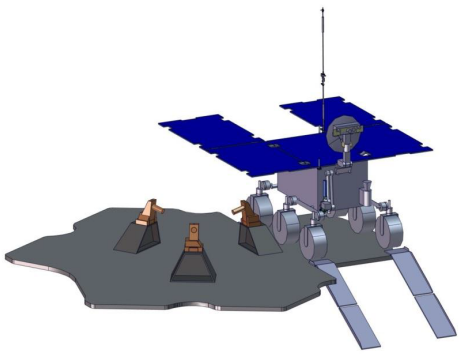

Figure 3.24: The MarsFAST rover [95].

Locomotion Locomotion is the main driver of MarsFAST rover design: it must be sturdy and reliable, and allow fast speeds to meet technology demonstration requirements. The rover employs a triple bogie architecture. It has 6 rigid wheels, with a 30 cm diameter and 13 cm width, each one equipped with one driving motor, one steering motor and one deployment and walking motor. All the actuators will be Maxon RE-max equipped with planetary gear. Sizes will vary depending on the actuator function. The rover has a ground clearance of at least 30 cm, can overcome 20 cm obstacles, climb slopes up to 20°, be stable under inclinations up to 35° and rove at a nominal speed of 1.8 cm/s on flat terrain [95]. Nominal roving has been identified in the semi-rough terrain at 2.1 cm/s wheel speed case, requiring 30 W of power [95].

EPS The EPS subsystem is tasked with providing enough energy for the rover mobility, but also to support the TCS in maintaining operational temperatures along the vehicle through resistive heaters. The rover deploys 2.24 m^2 of solar panels, for a 1.8 m^2 3G30 Next Generation Solar Cells surface, with a 33% efficiency and capable to provide 607 Wh/Sol EoL [95]. Li-ion secondary batteries with a capacity of 653 Wh/Sol in a 7s12p configuration are present on the vehicle: they weigh 4.8 kg. The Power Conditioning Unit (PCU) is based on an unregulated bus architecture and bus voltage will follow battery voltage during night and battery recharge mode [95]. An important driver for the EPS is to limit power consumption during hibernation, when the rover will consume just 18 W of power: 15 W by the TCS, 1 W by the EPS own PCDU and 2 W for the on board computer. This will allow the rover to survive without solar illumination for a maximum of 12 days, as in case of a dust storm [95]. Apart from hibernation, OBDH power consumption will amount to 14 W when the rover will be active but not navigating and 25 W during navigation [95].

TCS The baseline requirements for the TCS is to allow mission operations for consecutive 180 sols, in an equatorial latitude band situated between 5° S and 20° N. without RHUs. As insulation, a 3 cm thick layer of aerogel will cover the internal walls of the rover bathtub. An additional 3 cm thick aerogel layer will insulate the batteries, due to their high sensitivity to temperature gradients and narrow operational temperature range. 3 cm standoffs between avionics and their support plate will also be used to negate free convection, thanks to the low Martian pressure. The same applying for the batteries. Units and enclosure internal surfaces will be gold plated for low emissivity. Finally, loop heat pipe thermal switches will be employed to remove excess heat during roving and navigation. They will be connected to a 0.19 m^2 radiator [95]. The energy required for the heating of the rover over a sol oscillates between 298 and 350 Wh, depending on latitude, operational mode and the presence of, or not, of wind [95].

MarsFAST is a very useful design study and it can provide a solid baseline for the ice-mining Lunar rover design. The locomotion system is well characterized and with a low actuation cost. Another relevant baseline is provided by the OBDH hibernation power consumption, which will be required also on the ice-mining Lunar rover to save power and maximise battery recharge during the long ice-extraction phases.

3.4.2. Lunar rovers

The Moon is Earth only natural satellite and its nearest celestial object. Although relatively easy to reach, space exploration efforts have since long focused on other destinations, as interest in the Moon declined after the US crewed Moon landing of 1969. The race to the Moon was sprung by the progresses of the USSR, which through the Luna program, had deployed the rovers Lunokhod 1 and 2, in 1970 and 1973. An image of them is presented in Figure 3.25.

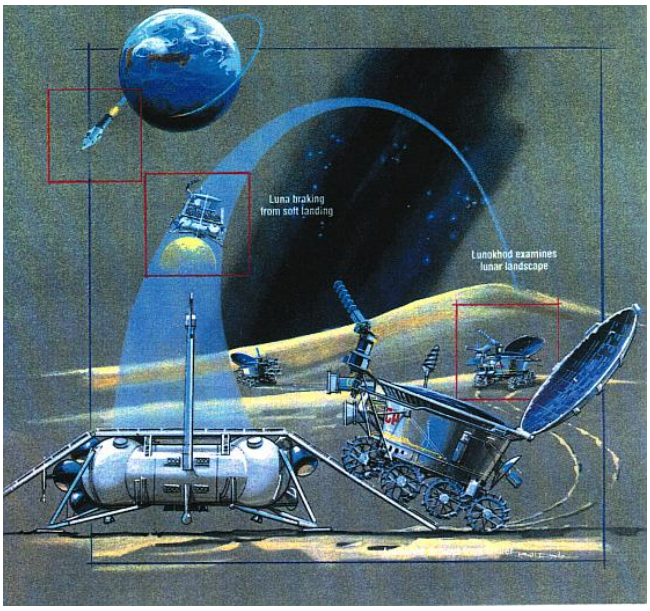

Figure 3.25: Lunokhod mission diagram [96].

Designed to support human missions, the two rovers weighted around 840 kg and were commanded by pilots who relied on static imagery and were dependent on shadows to identify surface reliefs [97]. Both rovers relied on eight independently powered woven-wire wheels, which could drive at two different speeds: 1 km/h and 2 km/h [98]. The rover managed to withstand the wide temperature excursion between Lunar day and night by relying on a clam-like lid which could be closed during the night, covering a radiator positioned on top of a pressurized electronic warm box hosting a Polonium-210 RHU. The inner surface of the covering lid hosted solar panels, so that during the Lunar days the sunlight could illuminate the open lid, while the radiator dissipated the heat from the RHU [97], as it can be seen in Figure 3.25.

A combination of difficulty in mobility due to the need for continuous human supervision and the partial failure of the lid mechanism was the reason for the demise of Lunokhod 2. In fact, as the Sun was behind the rover, the pilot in the mission control room could not spot a small crater in which the rover plunged. Although the crew had been able to steer the vehicle away from the crater, Lunar dust accumulated in the concave geometry of the lid, hosting the solar panels, causing a power dip. The loss of power could have been survivable would not have been for the fact that when closing the lid at night, some of the Lunar regolith, a silicate insulating material, fell on the radiator, causing the overheating of the internal components, delivering the final blow to the rover [97]. Lunokhod 1, instead, died out due to the natural decay of the heating capabilities of the Po-210 radioisotope, whose high-power density is counterbalanced by a very short half-life of 140 days.

After the end of the space race and following the successful Moon landings of the Apollo program, funding was next directed to more sustained crewed exploration in Earth Orbit. This was also the effect of a technological gap which caused entering space to be very expensive, making it sole appanage of governmental space agencies. Nowadays, we are at the start of a second golden era for Moon exploration, as access to space is becoming more and more affordable. Ice and oxygen mining techniques are being developed after the discoveries of solid-state water at the poles and institutional and private actors are developing plans land rovers for mining or exploration purposes. The following pages will illustrate some of them.

Volatiles Investigating Polar Exploration Rover

Volatiles Investigating Polar Exploration Rover (VIPER) is a Lunar volatiles and measurement detection mission in development at NASA and it will be delivered by Astrobiotic's Griffin lander under NASA CLPS program by the end of 2024. VIPER will land on Mons Mouton, on the west ridge of the Nobile crater, and will conduct science and map hydrogen bearing volatiles in the ISR, mainly located in the Lunar PSR craters [29]. The information VIPER will gather is not only of scientific interest, but will also help pave the road for an economically feasible ISRU of Lunar ice deposits, by assessing their amount and characterizing the physical processes ongoing in the Lunar cold traps. Due to the extreme temperature and power constraints posed by the harsh PSR environment, the rover is optimized for Lunar regions that receive prolonged periods of sunlight, and it will visit PSR only for few hours [30]. The mission duration will be more than 90 Earth days during which the rover will cover up to 20 km [30]. The rover is presented in Figure 3.26, it weighs around 430 kg, with a square base with a side of 1.8 m and a top mast height of 2.6 m.

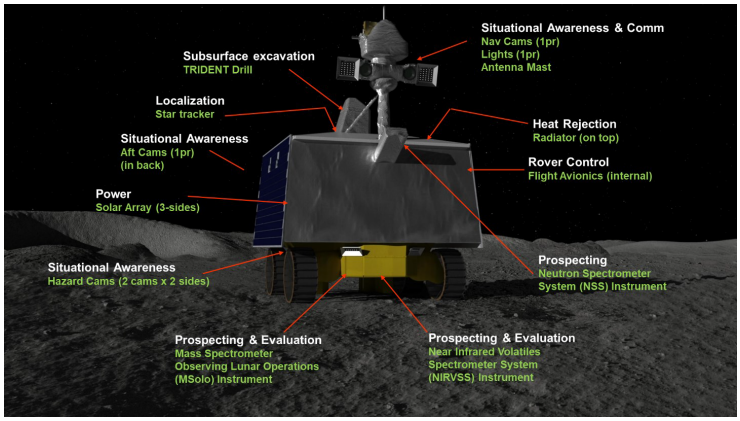

Figure 3.26: The VIPER rover and its equipment [29].

Mobility VIPER will have 4 wheels of 50 cm diameter, with the ability to overcome 20 cm large obstacles and to climb 15° slopes [30]. The maximum speed will be 20 cm/s [30], although the science acquisition speed will be 10 cm/s [29].

EPS VIPER equips three 1 m^2 solar panels, positioned on port, starboard and aft surfaces, generating about 410 W of electrical power. Batteries will be employed to backup peak power consumption regimes: PSR exploration and night-time survival electrical heaters [29].

As VIPER will not be fully autonomous, a DTE link must be established during roving and scientific operations. Furthermore, being the rover reliant only on solar panels, and having limited autonomy while on batteries backup power, both DTE and direct solar illumination are indispensable during operations. If any of the two requirements will not be satisfied, the rover will not be able to operate and will take the opportunity to recharge its batteries when the Sun will be present without DTE link. In case the Sun is not present, as in at night, the rover will go into sleep mode, turning off all the P/Ls and unrequired instrumentation and activating the survival heaters while running on battery power [29].

RPS powered VIPER based Lunar PSR exploration rover

VIPER is very versatile rover concept that lends itself to readaptations. A team of US-based researchers have recently proposed a design based on the original VIPER vehicle, refitted with RPS as electric power source instead of solar panels. A further iteration of the VIPER rover design was developed in collaboration with the University of Leicester, where an americium-fueled RPS was considered as the power source [99]. Replacing the electrical power source with a RPS revolutionized the mission operations, enabling the rover to venture inside the PSR for long periods of time, exploring them and conducting significative scientific experiments. Furthermore, the rover could have even more autonomy, enabling a journey of over 100 km in 18 months, with margin for potential decade-long operations, exploiting the 87.7 years long half-life of the radionuclide Pu-238 [100]. The RPS proposed is a Stirling dynamic radioisotope power system being developed by NASA as part of the Dynamic Radioisotope Power Sources (DRPS) program [101]. The RPS would produce around 300 W_e using six General Purpose Heat Sources (GPHS) and eight Stirling convertors. The RPS assembly would be quite bulky and heavy, but since it will be swapped with the solar arrays and a portion of the batteries, there would not be any increase in the final mass and size of the vehicle with respect to VIPER. Finally, the use of a dynamic conversion system would reduce the impact of the waste heat on the surroundings while still providing enough of it to heat up vital components during operations in the cryogenic PSR environment [100].

The prospected landing site is near Spudis Ridge, where the same Astrobiotic's lander from VIPER will let the rover egress to Lunar soil. From the landing site, the vehicle will be able to drive to numerous PSR areas with a deep dive into the De Gerlache crater. The rover speed and mobility capabilities will be the same of VIPER, but the possibility of working on a much tighter schedule comprising of 4 h drive, 4 h stationary science and drilling and 16 h rest, during which batteries will be recharged. Figure 3.27 illustrates the VIPER rover, modified with the RPS on the rear side.

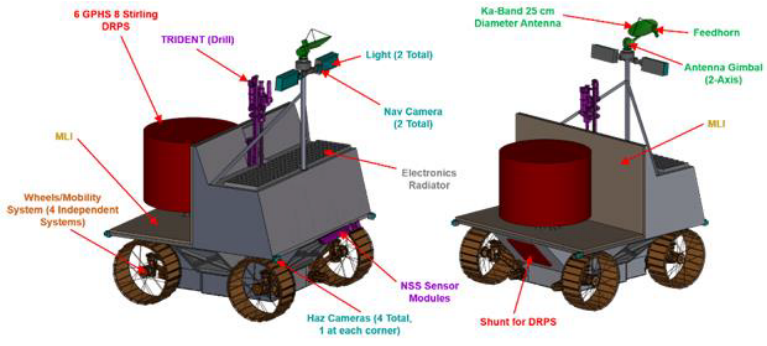

Figure 3.27: The RPS powered VIPER rover [100].

TCS The presence of the RPS on board of the vehicle gives rise to an important issue: the waste heat emitted by his radiators will interfere with the Lunar soil, impacting scientific measurements due to the alteration of the Lunar volatiles' composition by the strong incoming heat flux. Another criticality lies in the significant heat flow directed to the other rover components.

Both problems have solved by relegating the RPS to the rear portion of the rover volume, covering the view of its radiator to the front of the rover and to the Lunar terrain beneath it. This coverage is achieved through the installation of two MLI adiabatic walls separating the RPS from the soil and the anterior part of the vehicle [100]. Thanks to the presence of the two adiabatic walls, the waste heat from the RPS will now be able to interfere only with the Lunar surface that the rover has already traversed. Internal components will be kept into operative temperature ranges through a combination of insulation and louvered radiator surface, to eliminate excess heat in case of high temperatures. To avoid WEB overheating, it is required that the WEB radiator must be completely decoupled from the RPS radiator, meaning that the view factor between the two must be 0. A system of heat pipes and cold plates will reject heat from the WEB, while heaters will be activated in case of excessive heat loss [100].

EPS The Stirling controller is mounted directly below the RPS bottom panel, rebalancing the vehicle centre of gravity towards the geometrical centre of the rover volume and shortening cable length, saving mass. The 28 V power electronics box is located next to the Stirling controller. The power output of the DRPS will be 335 W_e at BoM, decaying to 315 W_e at EoM, considered as after 4.5 years after fueling. This is lower than the power output of the DPRS in a deep space environment (353 W_e), due to the fact that, being one third of the available radiator surface obstructed by the adiabatic walls, the Stirling engine temperature of the cold source is higher, decreasing its efficiency [100]. Batteries are employed to cover for peak power usage modes: mobility and drill. In any case, the EPS, taking advantage of the continuous power output by the RPS, will require a much smaller battery mass to meet the same operational requirements as VIPER, making this design a competitive alternative.
Table 3.3 shows a recapitulation of the main differences between the two designs:

Characteristic	VIPER	RPS powered VIPER design
Mass	430 kg	430 kg
Peak power	480 W	564 W
Time in PSR	6 hours per incursion	No time limit (18 months mission)
Lifetime	100+ Earth days	18 months, with possible extension
Communications	DTE: 230 kbps high-gain, 2 kbps omnidirectional	230 kbps to Gateway, 2 kbps emergency channel
Lunar regions	Sunlit areas with short PSR excursions, DTE cooms necessary	Unlimited exploration range and time, science area limited to forward of the rover due to waste heat
Science	VIPER volatiles science suite	Additional power available for science ops (16 h recharge, 4 h roving, 4 h science)
Cost approach	Novel design, launched by private partner (CLPS program)	Reduce development costs by leveraging design work of VIPER

Table 3.3: VIPER and RPS VIPER based rover characteristic comparison [102].

Both the original VIPER vehicle and the alternative DRPS based rover design could provide valuable insights and be used as baselines for the ice-mining rover concept development. In fact, the environment where VIPER and the ice-mining rover are going to operate is the same: Lunar PSR. They both face the same engineering challenges and could apply similar solutions to overcome their common design criticalities. The DRPS based alternative is particularly on the spot regarding similarities of objectives and possible solution to the PSR environmental challenges and could in fact be regarded as a "bigger brother" of the ice-mining Lunar rover, as the only significant difference between the two is the bigger size, heavier mass and larger power budget of the RPS based VIPER design.

MoonRanger

MoonRanger is a mission developed in concert by Carnegie Mellon University, Astrobiotics Technology and NASA Ames Research Center. The MoonRanger rover will land on the Lunar south pole aboard a Masten XL-1 lander in late 2023 [103]. From there, the 18 kg micro-rover will autonomously conduct scientific experiments in order to characterize hydrogenous volatiles at the south Lunar poles, including inside PSR. MoonRanger will host a single payload: a Neutron Spectrometry System. An illustration of the rover can be seen in Figure 3.28.

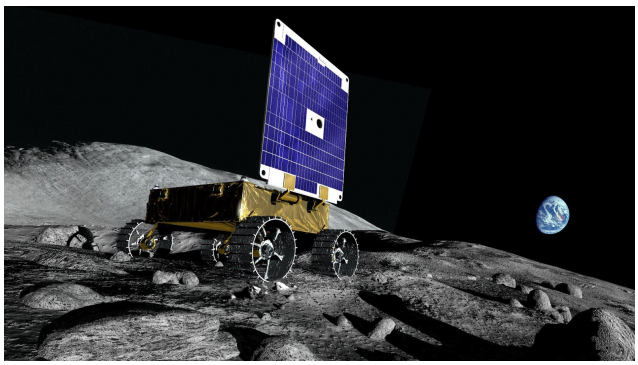

Figure 3.28: Artist impression of the MoonRanger rover [104].

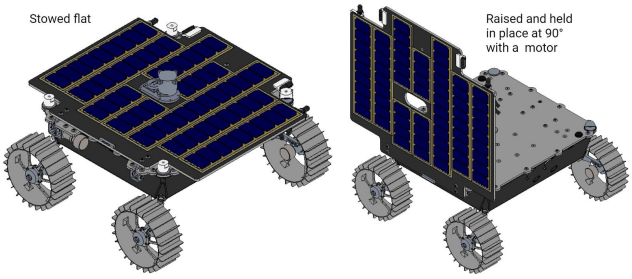

Figure 3.29: A CAD model of MoonRanger with the solar panel stowed and deployed [104].

MoonRanger designers adopt a low-cost approach in the rover development. Budget constraints, low mass and high mobility requirements resulted in a rover design heavily inspired from the Mars Pathfinder Sojourner rover, albeit with limited redundancies and significant trade-offs to be operated between many rover subsystems [104]. In fact, MoonRanger will not carry any direct-to-Earth capability, which will be tasked to the lander, so that and the rover will only have to interface with the much nearer lander. MoonRanger hss not been design to survive a lunar night, so its mission lifetime will only last half a Lunar day [104].

Mobility The four-wheel, skid-steered no suspensions mobility system is directed by a fully autonomous navigation system employing a light stripe-based mapping algorithm. The wheels are in aluminum and present a rim diameter of 17 cm, topped by a series of 25 grousers 1.5 cm long and granting a clearance from ground of 16 cm. Each wheel is actuated by a brushless Maxon motor. The rover nominal speed is 2.5 cm/s. Due to the low mass and high autonomy, the rover will conservatively avoid ascents greater than 10° and descents greater than 15° [104].

EPS The rover is Solar powered: the solar arrays will be folded over the upper radiator deck during the transfer. The solar panel surface will coincide with the rover upper panel dimensions of 65 x 68 cm. The solar panels will be deployed by the actuation of a series of hold-down-and-release mechanisms (HDRMs), and will reach the final configuration where the solar array panel will be orthogonal to the upper radiator deck, as shown by a picture of the rover in Figure 3.29.

TCS The thermal control subsystem design is greatly simplified by the short mission duration, which will not mandate the survival of a Lunar night. Nevertheless, the rover will have to endure terrain temperatures as low as 50 K while exploring the PRSs and will constantly be exposed to a sky sink temperature of 3 K. As a result of the tight power budget under which the rover is operated, thermal control strategies will be mainly passive, with the use of resistive heaters in the avionics' box only in case of survivability risk due to the cold external environment. The temperature range for surface operation has been conservatively set at -10°C to +35°C during surface operations and -15°C to +40°C during roving [104]. Passive thermal control strategies rely mainly on surface finishes to tweak surface emissivities locally for each component. MLI will avoid heat loss by radiation from avionics box, chassis, and wheels motors. The rover hosts two radiators, the first is the upper deck radiator, eliminating heat waste from the avionics which are mounted directly under it. The second one is the radiator on the back of the solar panels, which will see sunrays at almost 90° incidence, owing to the low angle of inclination of the Moon and the high latitude of the polar region.

LUVMI and LUVMI-X

The LUnar Volatiles Mobile Instrumentation (LUVMI) is a lightweight highly mobile rover vehicle designed by a consortium of European enterprises and universities coordinated and sponsored by ESA. The rover has been designed with the aim of exploring low illumination regions of the Lunar south pole and surveying for ice deposits, posing the basis for future ISRU ventures. The rover design is highly flexible, allowing for the installation of many different P/L classes; for the time-being, the P/Ls consist of a suite of volatiles science instruments and experiments [105]. LUVMI is a 40kg rover able to accommodate 30-40 kg of P/Ls. Onboard solar panels generate up to 180 W, at least half of which are available for the P/Ls. Batteries can be added up to 1750 Wh of capacity. Its envelope size amount to 85x92x45 cm when stowed and 140x92x80 cm when deployed. LUVMI has DTE link capabilities with uplink speeds of 1-2

Mbps, satellite data relay is also a possibility [106]. LUVMI-X is a lighter and more advanced iteration of the LUVMI design featuring higher mobility potential. It has a dry mass of 25 kg, topped by up to 25 kg of available P/L allowance. Solar panels output up to 140 W of power, of which more than half can be dedicated to supply P/Ls demand. Batteries can be scaled up to 1400 Wh of capacity. Stowed envelope dimensions are 85x77x35 cm while the rover will occupy a volume of 114x77x80c m when fully deployed [106].

Both rovers target the ambitious aim of a nearly 1:1 vehicle to P/L mass ratio. LUVMI-X solar panels have been optimized for catching the highest portion of sunrays possible at Lunar low latitudes, where the direction of sunlight is almost parallel to the terrain. Consequently, the solar panel will be deployed over a vertically mounted mast, whose axis can rotate freely to position the panel assemblage orthogonal to the incident sunlight [107], as show in Figure 3.30.

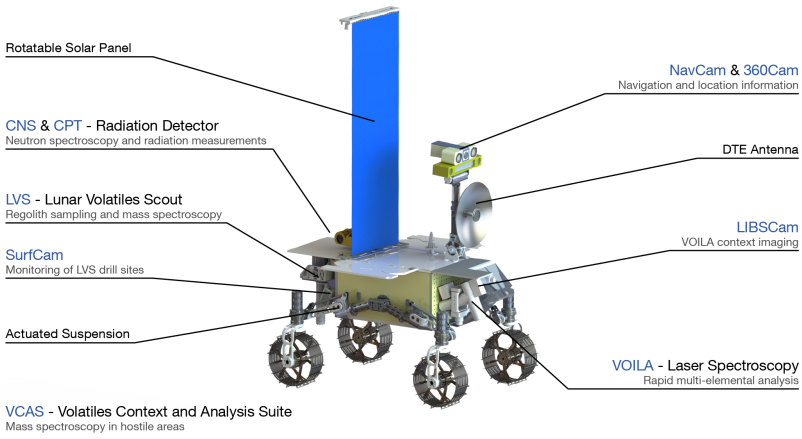

Figure 3.30: LUVMI-X and its instrumentation [107].

EPS The solar arrays, paired with battery backup power, are capable of sustaining operations in the darkness of PSR for 6 hours at a time, or can allow the rover to survive a short Lunar night for maximum 24 hours of hibernation thanks to polymide heaters located near the avionics [108]. At the poles, the Sun incident angle is nearly 90°: overheating is avoided through a series of sky-facing radiators. One of the design drivers of the LUVMI and LUVMI-X rovers is high mobility. In fact, based on the development team calculations, a possible exploration path of 5 km starting from a possible landing site near the Shackleton crater would be covered by LUVMI-X in half a Lunar day, or 14 Earth days [108].

Mobility Both rovers have 4 Aluminum wheels, hosting in-house designed motors. All wheels have independent steering capabilities of nearly 360° and are equipped with a differential mechanism. The wheels are equipped with grousers to increase traction on sandy terrains and wheel stiffness [108]. The rover also presents rocker bogie suspensions, capable of lowering its main body to surface level and raising it up to 30 cm from ground and can climb up to 30° slopes [108]. LUVMI and LUVMI-X have been designed to be teleoperated from Earth through DTE telecommunication link, but can also sustain a semi-autonomous operation regime [108].

LUVMI and LUVMI-X are a flexible rover baseline optimized for activities at the Lunar poles, with restricted PSR operative capabilities. In addition, it has been explicitly required by ESA

that such rover must be able to accommodate a wide range of prospective payloads enabling the maximum variety of mission objectives [108]. Hence, this design could be adopted as a baseline for the ice-mining rover as well. It is noteworthy that, as the ice-mining rover will not embark any scientific P/L, all the mass allotted to the P/L section could be used for hosting of the RPS assembly, which having a power density of 2 W_e/kg, would weigh around 40 kg. The RPS projected mass corresponds to the P/L allowance for the rover. Further mass margin could be granted by the consideration that counting the RPS as P/L would free up at least all the solar arrays mass, which was being allotted to the rover dry mass budget. Furthermore, it could be possible to procure another small mass and volume margin by limiting the capacity of the secondary batteries, since the continuous power output of the RPS would drastically reduce the need for backup power during PSR exploration and ice-mining. Finally, another design driver imposed by ESA is affordability [108], which harmonizes perfectly with the scope of the ice-mining Lunar rover mission, as it would allow a fast scaling up of operation once a suitable mining site has been discovered and rover operations have been fully qualified.

AMALIA

AMALIA is the rover conceived by Team Italia for participating in the Google Lunar X-Prize Challenge, not to be confused with the Amalia rover developed for the Exomars mission. The X-Prize requirements were to drive a minimum distance of 500 m and establish a telecommunication link with Earth twice. The teams must at least be 90% privately founded [109], so the imperative of containing engineering budgets was be the most potent driver of the rover design. Such requirement materialized in a light mass and low volume rover, in order to be able to secure a cheaper launch. Direct consequence was a short mission duration of half a Lunar day, to avoid the need for night-time survival, an L-band telecommunication system and an equatorial landing site, to maximize solar power generation [110]. AMALIA targets a mass budget of 30 kg, including SS margins. The design philosophy adopted requires simplicity, employing off-the-shelf components where possible [110].

The rover, shown in Figure 3.31, is composed by a platform on which are located the components. On top of it are located the foldable camera mast, solar arrays, and the WEB radiator. On the lateral sides are positioned two wings hosting additional arrays of solar cells, deployed upon lander egress. On the bottom surface is attached the WEB, accommodating all electronic components.

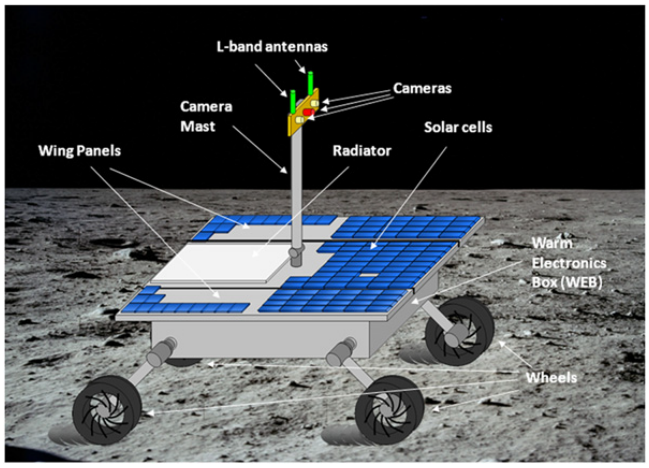

Figure 3.31: The AMALIA rover [110].

Structure The rover structural design is based on a trussed assembly developing around the WEB. For the aim of mass optimization, all trusses are made of Carbon Fibre Reinforced Plastics (CFRP). Two additional honeycomb panels have been installed with the aim of reinforcing the structure. One is located beneath the WEB, and is made of CFRP skins and Nomex core. The other, integrally composed of Aluminum alloy, is positioned on top of the WEB.

TCS As the rover will not be required to withstand the cold environment of a Lunar night, TCS design is greatly simplified, so passive thermal control strategies were targeted. The hot case has been considered as the moment during which the rover is moving on the Lunar surface under direct and perpendicular incident sunlight when regolith temperature can raise up to 400 K. Internal heat dissipation by other subsystems has been identified as 10.5 W due to locomotion actuators, 11 W due to robotics and mechanism actuators, 57.8 W for the OBDH subsystem and 8.8 W for telecommunications. The latter two loads are dissipated inside the WEB. To address the hot case scenario, a careful selection of surface finishes and control of thermal conductive path along the rover chassis have been analysed.A radiator has been installed on the upper platform, facing deep space, but with full view of the Sun. The baselined radiator, 0.22 m^2 large, will have an emissivity of 0.85 and an absorptivity of 0.15. To further reject heat from the scorching hot regolith, the whole WEB large parts of the rover are completely wrapped in MLI, with an emissivity of 0.05 [110]. Electrical heaters will act as thermostats, controlled by temperature sensors. They will be switched on during the only cold case scenario the rover will have to witness: the orbital transfer during the Earth to Moon trajectory.

EPS The rover electrical power system faces sizeable power requirements, especially from the locomotion subsystem, due to the necessity of covering 500 m in 14 days. Solar panels provide a 12 V regulated power bus. Li-ion secondary batteries will provide full power to the bus: around 100 W. They will weigh 750 g. Under these power requirements, batteries will last a hour [110].

Mobility The locomotion system is based on four non-pneumatic elastic wheels driven by brushless torque motors located in the hubs [110]. Four independent longitudinal swing arms acts as suspensions, they are provided with torsional spring but no damper, as the low speeds achieved by the rover and the smooth terrain it is going to drive over did not required them. Low pressure gas is blown in the wheel hubs and other cavities to avoid Lunar dust accumulation. All the wheels are driving, and their diameter is 18 cm. The rover will be able to overcome 7 cm large obstacles and driving over 12 cm long crevices. It can climb up to 20° steep slopes and present a maximum speed on level ground of 1.4 cm/s [110]. Each wheel, motor, suspension and power electronics assembly weighs 1.7 kg, margin comprised. On flat terrain, while travelling at top speed, each motor will provide a torque of 0.11 Nm requiring 0.017 W of power, for a total mobility power budget of 1.15 W. During the climb of a 20° slope the overall locomotion power requirement will increase to 19 W [110].

The AMALIA rover, although not designed to survive a Lunar night, and of lower mass than what could be expected from the anticipation over the RPS mass for the ice-mining Lunar rover, is of inspiration for the innovative and lightweight materials employed in its realization. Another point of merit of this rover design is the high mobility of the locomotion system, especially if compared to the low power requirements.

3.4.3. Martian and Lunar rover power budgets

The content of this subsection reports the power budgets of the rovers previously presented. As described in subsection 3.3.1, in any RPS, thermal and electrical power are shared from the same source, the radioisotope fuel module, in a zero-sum game fashion. For the design of a functioning TM, not only it is important to know the thermal environment and its imposed boundary conditions, but also the rover power budget and its EPS architecture. The two subsystems must divide between each other the only energy source on board of the rover: they are intimately interdependent.

Mobility power estimation Before reporting a detailed break-down of each rover power budget, it is worthy to consider the following engineering relationship for a first order estimation of the mobility system power consumption on level terrains [111]:

$$P_{Drive} = N_{Wheels} \cdot \frac{M_{Rover} \cdot g_{Moon}}{2} \frac{V_{max}}{\eta_{Gear}} \tag{3.1}$$

where the motor actuation power (P_{Drive}) depends on the number of wheels (N_{Wheels}), the rover total mass (M_{Rover}) and the local gravity g_{Moon}, roughly equal to 1/6 of Earth's gravity, around 1.62 m/s^2. Finally, it is also directly proportional to the maximum roving speed (V_{max}) and inversely proportional to the gear transmission efficiency (η_{Gear}), which has been set as 0.97 [111]. This relationship has been successfully used for the high level design of Martian rovers at JPL. The formula is very useful to understand the order of magnitude of the mobility subsystem power, even tough it must be noted that the most rover have two driving modes, normal (or science acquisition) and maximum speed: when the mobility actuators have been sized and selected to optimize power consumption for the slowest of the two, the maximum speed power requirements does not scale linearly with velocity, but follows an almost exponential regime.

Considering the LUVMI 4 wheeled-rover presented in 3.4.2 as a baseline for the ice-mining Lunar rover mass and size, the ice mining Lunar rover is projected to have a mass of ∼80 kg (40 kg rover + 40 kg P/L). Adding a +50% generous margin to reflect the difficulties and uncertainties of RPS integration over a very different original design, a very conservative mass of 120 kg is derived. Under these assumptions, the rover engines will consume just 4 W of

electrical power to actuate 4 motors at a nominal speed of 1 cm/s. If a nominal speed of 10 cm/s were needed, the total actuation power would be scaled up to 40 W. That would require larger motors, posing a cascade of constraints on other subsystems: an increased power to heat up the actuators, a more potent GNC equipment, resulting in a power consumption increase.

Rover speed is a very important metric, and it has non-negligible ramifications in many of the thermal control system architectural choices, which will be addresses in the next chapters. Furthermore, the requirements over the mobility subsystem vary substantially according to if the rover will need to climb the rim to get into the crater, or if it will be possible to land in an illuminated zone inside the crater and then rove into the PSR. If the latter were possible, a less mobile rover with limited speed would be a good choice, as it would probably be able to achieve the ice-mining requirements with a less complex and cheaper subsystems. This solution is also enabled by the latest observations of the Lunar south pole crater plateau surface, which is generally smooth and can presents paths with inclinations of less than 8° [112].

Power budgets Table 3.4 illustrate the Mars Pathfinder Sojourner rover power breakdown. The data are enriched by Table 3.5, reporting the power budget breakdown of Rocky VII, the previous design iteration of Sojourner. Although the mass of both rovers is one order of magnitude lower than the ice-mining Lunar rover projected mass, some data can be nonetheless extrapolated, as computer system and the sensors power budget do not scale with rover mass.

Function	Power	Time	Energy
Motor heating (1 motor at a time)	7.51W	1h	7.51Wh
Motor heating (2 motors at a time)	11.26W	0.5h	5.63Wh
Diving (extreme terrain at -80°C)	13.85W	0.5h	6.92Wh
Hazard detection	7.33W	0.25h	1.83Wh
Imaging (3 images at 2 rein/image)	4.5	0.1h	0.45Wh
Image compression (compress 3 images at 6 rein/image)	3.7W	0.3hr	1.2Wh
6Mbit communication (50 min/sol)	6.27W	0.8h	5.2Wh
42 10s health checks per day	6.27W	0.1h	0.63Wh
Remainder 7h daytime CPU operations	3.7W	4h	15Wh
WEB heating	as needed	as needed	50Wh max.
Solar panel production	Peak:≥10W	6h/sol	104Wh/sol

Table 3.4: Sojourner electric power budget breakdown [85].

The motors actuation power can validate the relationship in Equation 3.1. Rocky VII maximum velocity is 30 cm/s: it is hypothesized that the nominal speed will be one order of magnitude lower, around 3 cm/s. Considering mass 11.5 kg under Martian gravity, the predicted actuation power for the 6-wheeled vehicle will be ∼8 W, confirming the data in Table 3.5.

Subsystem	Power	Mass
Computer system	28W	2.5kg
Sensors	6W	1kg
Motors (nominal)	8W	2kg
EPS	6W	Batteries: 2kg Solar panels: 2kg
Structure	-	4kg
Total	48W	11.5kg

Table 3.5: Rocky VII EPS breakdown [113].

Table 3.6 reports the power budget of the RPS powered VIPER design based PSR exploration rover. To the contrary of Sojourner and Rocky VII, this design have more than twice the projected mass of the ice-mining Lunar rover, and more than one order of magnitude of its available power. In any case, the information provided by Table 3.6 is interesting to characterize mass uncorrelated subsystems such as OBDH and TMTC, which instead depends on the computational load and on the telecommunications architecture, which would be shared between the RPS powered VIPER and the ice-mining Lunar rover (either lander of Gateway relay). It is also noteworthy the fact that the TCS power budget allocated active components such as heaters is very low and constant within the alternation of the various power modes, showing that is possible to maintain almost all equipment inside its operational temperature range without much difficulty, even in PSR, as the waste heat from the RPS can be employed for this purpose. Finally, it is again possible to validate Equation 3.1, as entering with the rover 430 kg of mass and maximum speed of 20 cm/s, the 4 wheeled vehicle is expected to consume ∼288 W, very close to the 300 W accounted for the "Peak roving" mode.

	Ground & launch phases	Lunar transit & descent	Rover check-out	Peak roving	Roving science sunlit	Drilling science sunlit	Standby phase sunlit	Roving science shadowed	Drilling science shadowed	Standby phase shadowed
Time	30d	4d	1d	0.5h	8h	1h	16h	8h	1h	extended
Rover total	86W	128W	254W	564W	354W	430W	174W	334W	430W	132W
RPS	39.0W	39.0W	39.0W	39.0W	39.0W	39.0W	39.0W	39.0W	39.0W	39.0W
AD&C	-	-	54.7W	54.7W	54.7W	11.0W	7.0W	54.7W	11.0W	7.0W
OBDH	28.0W	28.0W	28.0W	47.6W	49.3W	49.3W	20.4W	49.3W	49.3W	20.3W
TMTC	-	42.5W	42.5W	42.5W	42.5W	42.5W	42.5W	42.5W	42.5W	-
EPS	10.1W	10.1W	10.1W	30.3W	30.3W	30.3W	15.6W	30.3W	30.3W	15.6W
TCS	6.8W	6.8W	6.8W	6.8W	6.8W	6.8W	6.8W	6.8W	6.8W	6.8W
P/L	1.6W	1.6W	73.2W	43.2W	81.2W	251.2W	43.2W	51.2W	251.2W	43.2W
Mobility	-	-	-	300.0W	60.0W	-	-	60.0W	-	-

Table 3.6: VIPER electric power budget breakdown [100].

Table 3.7 illustrates some equipment power consumption from the AMALIA rover design. Even better than with the RPS powered VIPER rover, this power budget breakdown can give an idea

of the ice-mining Lunar rover rover-to-lander telecommunication equipment power requirement, which should be less than 10 W. Once again, Equation 3.1 is confirmed by the data presented in the table. In fact, the 4 wheeled vehicle, moving at a nominal speed of 1.4 cm/s and having a mass of 30 kg will see a predicted mobility system power demand of 1.4 W, which is in line whit the table reported value of 1.15 W total consumption plain terrain.

Function	Power/Actuator	Total SS power
Mast 3DOFs mechanism (Maxon RE025)	≤10W	≤30W
Command data handling & GNC	-	57.8W
Telecommunications	-	8.8W
Camera system optical head (CSOH)	-	∼4W
Camera system electronic module (CSEM)	-	4W idle or in download 8.5W acquisition and/or download
Mobility	0° slope: 0.0170W 20° slope: 0.0742W	0° slope: 1.15W 20° slope: 19.0W

Table 3.7: AMALIA electric power budget breakdown [110].

Finally, MarsFAST, the ESA-JPL joint design study report for an autonomous highly mobile 150 kg rover, has a declared mission scope of demonstrating European planetary exploration technology by covering 15 km on Mars [95].The rover nominal speed is 1.8 cm/s. Applying Equation 3.1 to the rover mass and considering Martian gravitational acceleration of 3.72 m/s^2, the 6-wheeled MarsFAST mobility system will have a nominal consumption of 31 W, comparable to the rover "Drive mode" mobility system power budget from Table 3.8, and very close to the values reported in the literature [95].

	SS Peak power	EDL	Deploy-ment	Drive	Science short stop	Science long stop	Science night stop	Nominal night	DTE Comms	Idle day	Sleep
Rover total	N/A	20W	42W	79W	60W	52W	36W	20W	52W	29W	18W
TCS	-	4W	6W	-	6W	6.38W	12.15W	12W	4W	6W	15W
Mobility	76W	-	-	40.98W	-	-	-	-	-	-	-
TMTC	-	-	-	3W	3W	3W	-	2W	24W	4W	-
OBDH	-	3W	14W	25W	14W	14W	14W	2W	14W	10W	2W
Mechanisms	10W	6.4W	14.75W	-	-	10W	-	-	0.3W	-	-
GNC	3.7W	-	-	2.85W	-	-	-	-	-	-	-
Cameras	10W/each	-	-	-	20W	1.68W	-	-	-	-	-
EPS	-	4W	7W	7W	7W	4W	4W	4W	7W	7W	-
P/L	67W	-	-	-	10W	8.06W	5.98W	-	2W	2W	1W

Table 3.8: MarsFAST electric power budget breakdown [95].

4 | The ice-mining Lunar rover final design

Before reporting the various trade-offs performed to reach the ice-mining Lunar rover final design for this feasibility study, and illustrating the thermal analysis and their results, the rover CAD model will be presented. This is done in order to give the reader an idea of the subsystems, the instrumentation geometries, and their position aboard of the rover. Figure 4.1 shows the rover on the Lunar surface, Figure 4.2 illustrates a longitudinal section of the rover, in both images represented during the water extraction phase.

The rover model presented in the figures has been designed on the Siemens NX CAD, numerous FEM thermal analysis have been run based on a subset of the parts presented in the previous images. Such elements have been chosen in order to minimize computational loads and simulation time, while result accuracy has been kept high by the employment of all the most representative parts to simulate the heat flows from the DRPS, only heat source, to the sublimation plate target and through many loss paths along the rover.

The rover is divided in three main areas by the adiabatic wall ① made in insulative material and coated in MLI, its design have been derived by the DRPS powered VIPER concept, albeit in a slightly rearranged form. The rear part hosts the DRPS ⑦, only source of electrical and thermal energy for the rover, which is encased by the highly insulative DRPS sleeve ②. On the front side, separated from the DRPS heat source by the vertical portion of the adiabatic wall, lies the cold trap ③, on top of the WEB ④. Finally, the bulk of the adiabatic wall is what can be called the main deck of the rover: the horizontal part which has both thermal and structural purposes. This section of the adiabatic wall is tasked with sustaining the other rover subsystems and components, also providing an interface for the locomotion system ⑤, whose architecture has been derived by LUVMI. Finally, the insulating rover deck also delimits the third and last macro-area of the rover: the part below, between the walls and the Lunar surface, where it is fitted the lowerable MLI Tent ⑥. The MLI tent is tasked with encasing the sublimation plate and the Lunar surface area where ice extraction is being carried out, in order to locally focus the irradiated heat but also to create a sealed environment to limit volatiles losses.

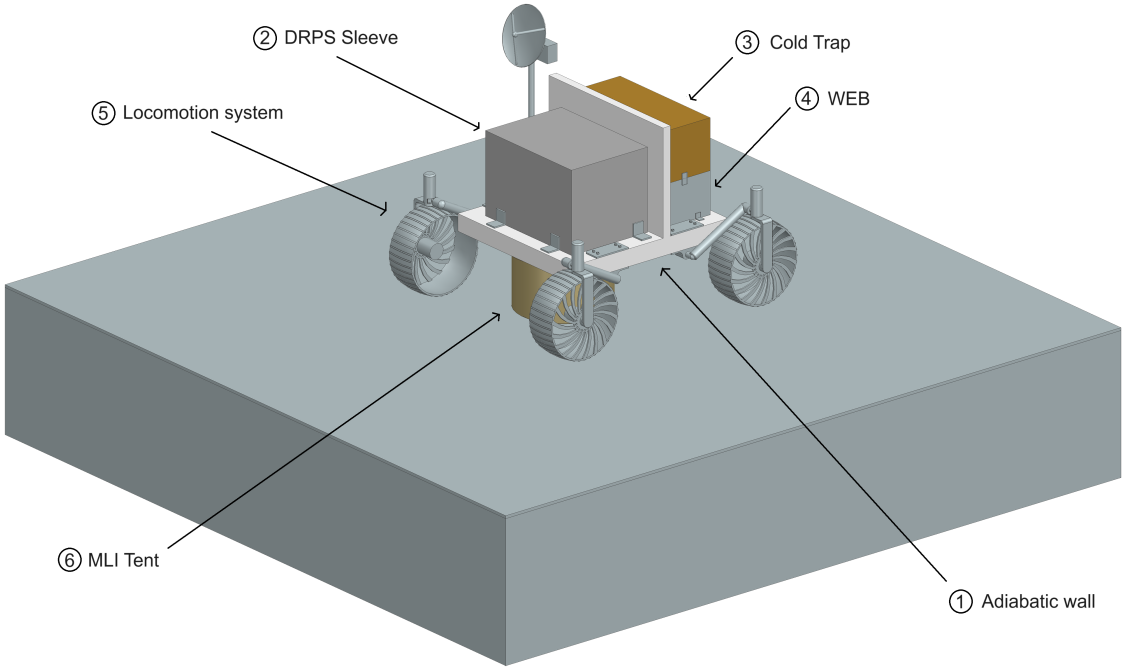

Figure 4.1: The ice-mining Lunar rover CAD model, shown during the extraction phase.

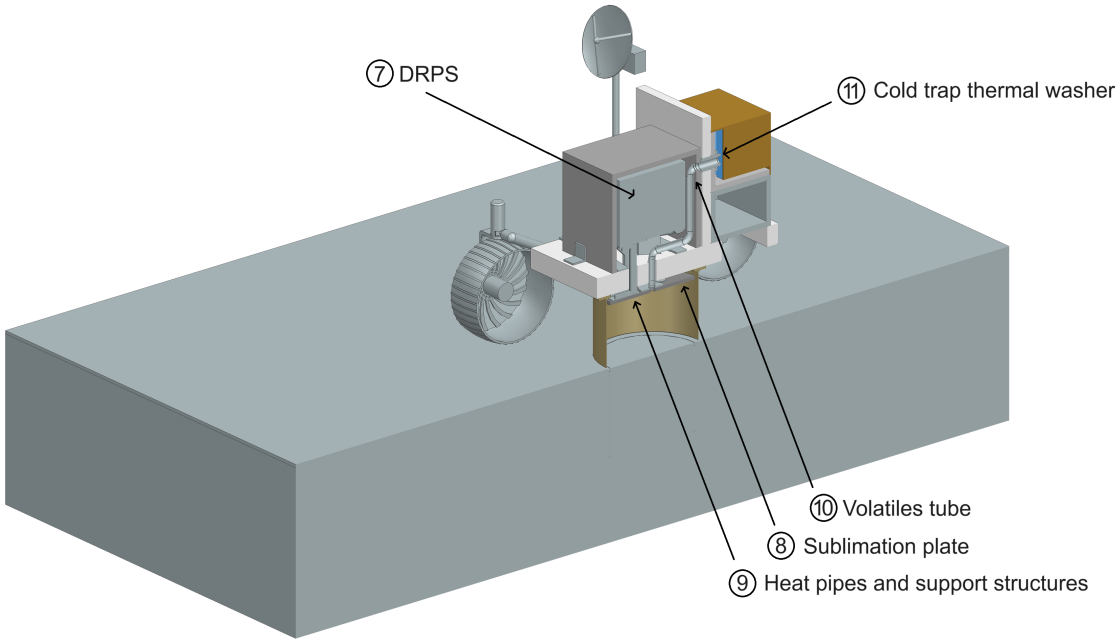

Figure 4.2: A longitudinal section of the ice-mining Lunar rover CAD model, shown during the extraction phase.

The section view is also informative, showing the internal arrangement of the TMS. The DRPS ⑥, contained in the insulating sleeve ②, has only a favourable low resistance heat transfer path leading to the sublimation plate ⑧. The sublimation plate is thermally connected to the DRPS by three heat pipes ⑨, whose sustaining structure also acts as support for the sublimation plate, which is not physically connected to the adiabatic wall to limit thermal losses. In the geometrical centre of the circular sublimation plate is inserted the volatiles tube ⑩. It is tasked with the transportation of the extracted water vapour to the cold trap, where it will deposit to be captured in solid form. The tube is physically connected to the sublimation plate to collect some heat in order to be maintained at a high enough temperature to avoid ice deposition on the conduct. Finally, the other end of the tube is connected to the adiabatic wall and the cold trap through a thermal washer ⑪, in order to thermally decouple it from the cold trap, avoiding large heat losses to the latter.

Finally, the rover CAD model used for the thermal analysis has a maximum envelope size (LxWxH) of 200x170x130 cm. This envelope size has been measured considering the wheels, but not the camera boom. One of the most important elements, contributing greatly to the rover geometry, is the adiabatic wall. The adiabatic wall can be used as reference scale for the rover dimensions, as it will be the mounting interface for all the rover components. It measures 127 cm in length, 114 cm in width and 87 cm in height. Under it, it is attached the lowerable MLI tent, 40 cm tall when fully deployed. Ground clearance is 36 cm during the extraction mode, but it can be increased during roving, if necessary, thanks to the suspensions system. The actual maximum ground clearance is dependent on the locomotion system design, and it lies outside of the scope of this work. Given the early stage of the work, and the complexity of a mass budget analysis, a definition of the total mass of the rover is also outside of the scope of this thesis. Nonetheless, it holds what stated in subsection 3.4.2 during the presentation of LUVMI, so an unmargined baseline of 80 kg is the staring estimate for the ice mining Lunar rover, and it will be used as a preliminary value to run tradeoffs, such as it was done for the estimation of the locomotion system power consumption in Equation 3.1.

4.1. Discussion over the various susbsystems

This section will focus on a more detailed description of each rover part, explaining the reasons for its employment its purposes and how it interfaces with the rest if the rover. In order to ease the introduction, all the components will be presented from the TMS designer perspective. High and low temperature segments in the TMS have been identified. These two groups are roughly based on each component temperature during ice mining operations, but also on the thermal requirements they are subjected to. Finally, some parts that are not strictly related to the TMS, but are still relevant, will also be briefly introduced.

4.1.1. The high temperature segment

The high temperature segment of the TMS comprises of all the elements which are expected to have a temperature higher than 100°C, which is the minimum temperature requirement for the sublimation plate. From a functional perspective, the high temperature segment consists of all the elements that contribute to the redirection of the DRPS waste heat to the sublimation plate, where is it expected that the majority of the heat may flow through. Figure 4.3 shows a CAD rendering of the assembly of the TMS high temperature segment components: the DRPS ①, the DRPS insulating sleeve, the DRPS sustaining structure ②, the heat pipes and the heat pipes sustaining structures ③, the sublimation plate ④ and the volatiles tube ⑤.

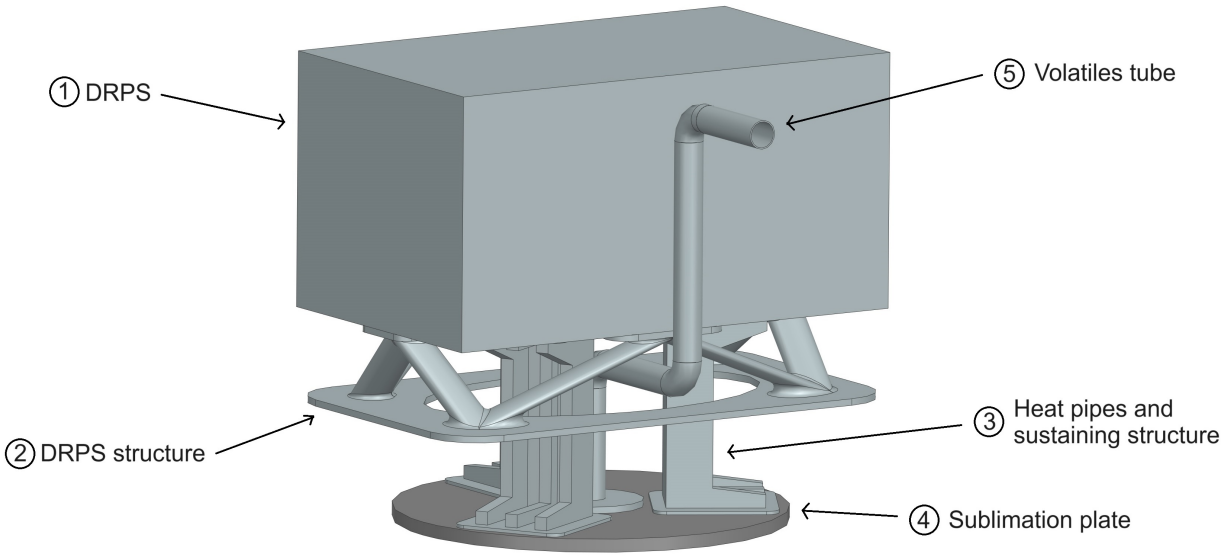

Figure 4.3: The high temperature segment of the rover TMS.

The DRPS

The rear portion of the rover is totally occupied by the Dynamical Radioisotope Power System (DRPS), which is located sideways, with his longer dimension on the width direction. This has been done in order to save space on the rover deck: the horizontal surface of the adiabatic wall. The DRPS has been modeled as a solid aluminum box, the size being 76x46x39 cm. Its dimensions, in absence of a flight qualified European Stirling engine conversion based DRPS, have been taken from the now discontinued NASA Advanced Stirling Radioisotope Generator (ASRG). This choice is also corroborated by the fact that both the ASRG and the breadboard model of the ESRG, the European Stirling Radioisotope Generator, present a similar power outputs, so that the ASRG has been taken as a baseline for the simulation of the RPS on board of the ice-mining Lunar rover.

The DRPS is the only source of energy powering up the rover, not only from and electrical power budget standpoint, but also from a thermal perspective, as there will be no sunlight nor any other source of heat in the cryogenic environment of the PSR. As introduced in section 2.1, the DRPS will based upon the ESRG. It will host two ELHS for a combined power output of 400 W_{th}. From this source, the Stirling convertor will provide an electric power output of 80 W_e, while 320 W_{th} will be radiated away as waste heat. This will be the thermal power budget for the ice-mining operations.

The DRPS insulating sleeve

The DRPS insulating sleeve is a shell shaped rigid envelope surrounding the top and lateral faces of the DRPS and insulating it from the view of deep space and the surrounding cryogenic environment. It is 2 cm thick, leaving a 2 cm gap from its inner surface to the DRPS. The gap increases to 8 cm in the front, to accommodate for the volatiles tube. The sleeve is wrapped in MLI on both the inner and outer surfaces, in order to minimize heat exchange trough infrared radiation and the subsequent radiative losses to the environment. The shell is composed of Rohacell foam based composite material, cured with carbon fiber skins or similar. Rohacell foam has been employed for its excellent structural properties as a composite core, but above all for the extremely low conductance, which makes it an excellent insulator.

For the moment being, the sleeve is not equipped with any radiating surface, following the assumption that heat waste is needed for water extraction and the adoption of simple architectures. In any case, a louvered radiator could be installed in a future iteration of the project. Such a device would provide the rover with an emergency outlet for the waste heat, to be used as a relief valve in case of temperature buildup due to off design conditions. Finally, a more refined louvered architecture could allow for at least some degree of DRPS radiator temperature control, albeit it would probably be a coarsely accurate one.

The DRPS sustaining structure

The DRPS sustaining structure is the interface between the DRPS and the adiabatic walls. It is realized in a trussed structure fashion with a hollow space in its center to leave space for the three heat pipes and their supporting structures. The DRPS bearing structure is composed of a plate, attached to the adiabatic walls, 8 beams, which are joined as couples in 4 separated plates where the DRPS will be mounted. The beams section have been sized to withstand the bending loads caused by a 20 g deceleration of the DRPS mass. The whole part is composed of Ti-6Al-4V, a titanium based alloy. Titanium is a lightweight, high-strength high-resilience material. Apart from his excellent mechanical properties, titanium also has a very low thermal conductivity, less than ten W/(m·K). This characteristic is very important for the TMS design as the sustaining structures are heat loss sources, and their conductivity shall be limited.

The heat pipes and their sustaining structure

Heat pipes are the selected technology to transfer the waste heat from the DRPS to the sublimation plate. As the heat waste output from the DRPS amounts to 320 W, three heat pipes transporting around 100 W each have been employed. Since there will be losses, the actual heat conducted through each heat pipe might be lower. The three heat pipes have been installed with radial symmetry, to spread the heat in the most uniform way possible on the sublimation plate, which is also circular. They are separated by an angle of 120° from each others.

The TMS design is still at a preliminary stage, reason for which a thorough sizing for the heat pipes has not been carried out. The baseline for the heat pipes that has been employed is water-copper heat pipes. Their thermal conductivity value to be used in the NX thermal analysis has been conservatively set as a lower than an average value of 50000 W/(m·K). It is also important to note that the heat pipes will have to work against gravity, even though lunar gravity is just 1/6 of Earth gravity. This adds another layer of complexity that must be solved in later iterations of the TMS design.

The supporting structures have the objective of sustaining both the heat pipes and the sublimation plate. They are attached directly to the DRPS, in order to better draw heat waste from it. The heat pipe sustaining structure, apart from acting as a structural component, shall also be manufactured in a highly conductive material, as it must collect heat from the DRPS and transfer it to to the heat pipes on their evaporator ends. The structure is made of aluminum alloy, which is a metal with a high strength-to-weight ratio and very good thermal conductivity, in the order of hundredths of W/(m·K). The heat pipe supporting structure section has been sized for a bending stiffness high enough to present a first natural frequency of at least 100 Hz, under the cantilevered beam model with a mass on the tip subjected to a 20 g oscillating load. The height of the heat pipe structure in 15 cm.

The sublimation plate

The sublimation plate is the terminal part of the TMS high temperature segment. It is on the sublimation plate that the majority of the DRPS waste heat must be directed. The sublimation plate radiator temperature must be at least 100°C, this in order to achieve a radiative heat flux of 1 kW/m^2 on PSR regolith. To maximize the amount of heat deposited onto the plate, it has been located just to the bottom of the DRPS. The plate has been fitted under the adiabatic wall, encircled by the MLI tent, which can be lowered down when sublimating ice in order to create a sealed atmosphere. Its only support is shared with the heat pipes, contributing too to the heat transfer process. The sublimation plate is of circular shape and has a total area of 0.28 m^2. The CAD model is 2 cm thick. The side facing the regolith is equipped with a black radiator with an emissivity value of 0.9. The fact that the sublimation plate, due to its position, can

never be under sunlight, allowed for the selection of a high-emissivity high-absorbivity surface finish for the radiator, increasing emissivity from the usual 0.85 to 0.9. For thermal modeling purposes, the sublimation plate has been considered as made up of aluminum. Finally, the plate present a 2 cm radius circular hole centered in its middle, from where the volatiles will enter a tube leading them to the cold trap.

The volatiles tube

The volatiles leading tube has the primary task of directing the volatiles from the MLI tent sealed environment to the cold trap. The tube is the only direct physical connection from the TMS high temperature segment to the low temperature one. Great care must be exerted into limiting parasitic heat transfer from the high temperature sublimation plate to the cold trap. Two different approaches were considered and after the trade-off performed in subsection 4.2.2, the leading tube option was preferred.

The tube solution presents a set of two conflicting requirements. The first one is to limit heat conduction from the plate to the cold trap, to avoid that an increase in the cold trap temperature jeopardizes its functionality. The second one is that no ice must deposit on the tube inner surface, to avoid the tube being clogged and the unwanted ice obstructing new water volatiles passage to the cold trap. To avoid ice formation, the tube temperature must always be higher than the deposition temperature of water gas in vacuum: 200 K. To solve this problem, the tube is made of copper, a highly conductive metal. It is 2 mm thick and presents a circular flange on the hot end on the plate. The tube has bended shape, as shown in Figure 4.3, in order to move around the other TMS high temperature segment components. Figure 4.2 illustrates how the tube is integrated within the rest of the rover. Starting from the sublimation plate, it pierces through the horizontal part of the adiabatic wall and coasts the DRPS inside the sleeve for as much of its length as physically possible. This design choice has been taken to expose for as long as possible the tube to a high temperature environment, in order to assist temperature retainment. Finally, the tube exits from the DRPS sleeve, passes through the vertical portion of the adiabatic wall to enter the cold trap. To limit heat transfer to the cold trap, the terminal part of the tube is encased in a low conductivity polymer sleeve, acting as a thermal washer.

4.1.2. The adiabatic wall

The adiabatic wall, which design have been inspired from NASA DRPS powered VIPER rover study, has, as most of the rover components, a double function. Primarily, it must support and interface with all the other parts, but it also needs to fulfill two important thermal management tasks: the separation between the high temperature and low temperature TMS segments, and the isolation of the rover components from the PSR cryogenic temperature Lunar surface. The former is performed thanks to the vertical portion of the wall, separating the rear part,

hosting the DRPS (right side in Figure 4.4) from the front area, hosting WEB and cold trap (left side of the figure). The latter is fulfilled thanks to the horizontally positioned thick slab, which is further reinforced as it also needs to support the weight of the other components. The wall presents holes for the volatiles tube and the heat pipes in the rear part, for the volatile tube entrance to the cold trap on the vertical side, and a large opening for the WEB radiator on the frond part. The horizontal part of the adiabatic wall is 12 cm thick, while the vertical one is 6 cm. They are both realized in a sandwich panel composite material, with two plies of carbon fiber or similar laminate material, encasing a refractory foam core. The considered baseline is the commercially available Rohacell 71 HERO Foam. Space rated and distributed by Evoink Operations GmbH, it presents good mechanical properties and excellent insulating capabilities with a thermal conductivity of just 0.0246 W/(m·K) [114].

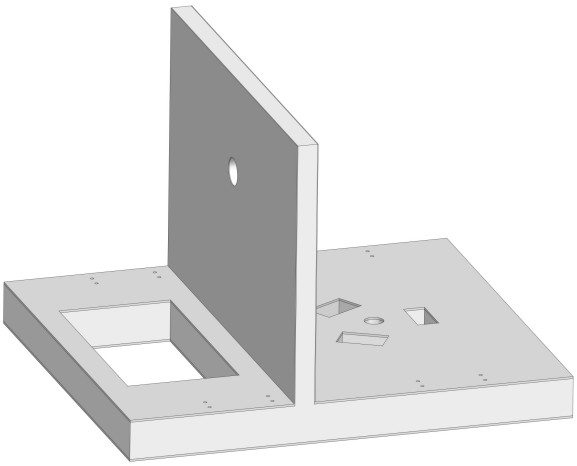

Figure 4.4: The adiabatic wall.

4.1.3. The low temperature segment

The low temperature segment of the TMS comprises of the elements that must be kept at low temperature to fulfill their task. Its architecture is much simpler than the high temperature segment as it comprises only of the cold trap and its interface with the volatiles tube.

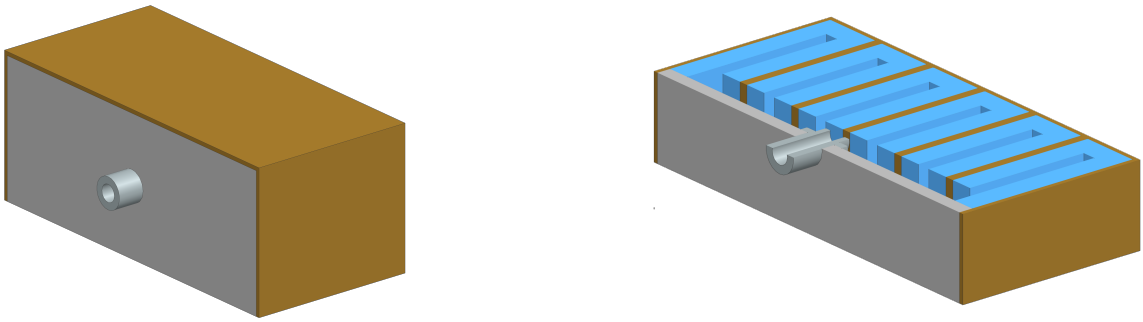

Figure 4.5: The cold trap, with the radiator shell, its adiabatic wall and the interface with the volatiles tube, presented as seen from the outside and sectioned.

The cold trap

The cold trap is located on top of the WEB, insulated from it, in the front part of the rover. On the outside it is shaped like a box of dimensions 90x42x36 cm. On the inside, it presents 5 fins made of copper, as shown in Figure 4.5. The task of the cold trap is to provide to the water vapour coming in from the tube a cold surface to deposit. Its temperature of the fins must be at least lower than -20°C. The actual temperature depending also on the pressure of the volatiles in the cold trap. For this reason, every side of the cold trap box that have a view on the outside environment is equipped with a radiating surface, so that the latent heat of deposition of the water volatiles can be dissipated into the outside environment.

The cold trap interior is part of the sealed environment created with the lowering of the MLI tent. The volatiles will flow in the cold trap naturally, driven by pressure differential as other water molecules deposit on the finned surface. The fins are 2 cm thick and 32 cm long. They are made in copper, to exploit the high thermal conductivity of the metal. They have been sized in order to conduct away all the heat derived from a reference water volatiles mass flow rate, derived from the literature. The external shell which surfaces host the radiators is also manufactured in copper, to achieve better heat rejection performances with the reduced radiating surface available. The radiator is a high-emissivity low-absorbance surface, with a baselined emissivity of 0.85. The cold trap rear and bottom sides, are constituted of a 3 cm thick adiabatic wall, to avoid heat leaks from the high temperature segments and to separate the cold trap from the WEB, which must be maintained at warmer temperatures. The same solution as for the rover adiabatic wall has been adopted, with these two sides composed of Rohacell 71 HERO Foam based sandwich panels.

The thermal washer interface

The cold trap, being at a very low temperature, cannot be interfaced directly with the highly conductive copper volatiles tube. Hence, a thermal washer to insulate the tube from the cold trap adiabatic wall is needed. The thermal washer, which can be seen protruding from the cold trap in Figure 4.5, is a sleeve shaped PEEK insert that encloses the tube on the inside and is in contact with the rover adiabatic wall and the cold trap insulating side on the outside. PEEK, a colourless organic thermoplastic polymer, has been selected for its very low thermal conductivity, in the order of tenths of W/(m·K).

4.1.4. The WEB

The Warm Electronics Box is a heavily insulated shell containing the rover electronics, such as the on board computer and the batteries. It is a widespread and effective solution to the thermal management of the rover electronics, requiring restricted temperature intervals to operate.

The WEB will be heated up by the electronics waste heat, produced by their activity. In case electronics waste heat were not enough to keep the WEB at the correct temperature, electric heaters or RHUs could be employed, even though passive methods should be preferred. The WEB, which will not be included in the thermal modeling at this stage of the work, will likely be manufactured in a similar insulative material as the rest of the rover structures: a sandwich composite panel with a refractory foam core. The WEB will be equipped with a downward facing radiator, able to reject the electronics heat to the cold regolith surface. The radiator can be louvered, in order to maintain heat inside the WEB in a cold case scenario. The electronics plate will be connected to the louvered radiator either by high conductivity copper or graphite thermal straps, or directly by water-copper heat pipes. Finally, in case heat retainment inside the WEB proved difficult, a conductive strap could be fitted inside the horizontal potion of the adiabatic wall, one end connected to the WEB and the other reaching the hotter area in the proximity of the high temperature TMS segment components. In such a way, the thermal strap could conduct some heat from the DRPS area to the WEB, easily maintaining it warm.

4.1.5. The locomotion system

The locomotion system, shown in a foreshortening in Figure 4.6, has been inspired by LUVMI. It has the task of allowing the rover to autonomously reach the ice deposits inside the PSR and delivering the extracted resource back to the processing plant. The locomotion system has also not been analysed in the FEM thermal analysis either, as the investigation focused chiefly on the thermal performances of the TMS and the ice-mining operations feasibility for the rover. Designing with the aforementioned requirements in mind, the functionalities expected from the locomotion system are multiple. First of all, the fraction of DRPS waste heat lost through the suspension and wheel assembly must be the lowest possible. This can be done by employing low conductivity metals for the suspensions, like titanium alloys, or even polymer based composite materials. The wheels will present grousers, both to increase traction on the fluffy upper layer of the Lunar regolith, but also to limit the rover contact with the cryogenic ground to the smallest possible conducting section. Another important requirement is the capability of changing the clearance from the ground, which will help the rover to adapt and to overcome the obstacles that it might encounter in the case it had to cross the crater edge. This functionality will also be needed to assist the deployment of the MLI tent at the start of the ice extraction operations. Roving speed, on the contrary, is not a priority of this design, and has

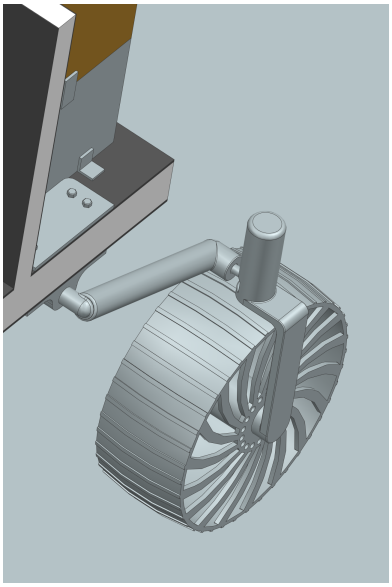

Figure 4.6: A foreshortening of the mobility system.

been maintained low (1 cm/s nominal speed), in order to limit the electric power demand and alleviating the requirements on the navigation subsystem.

4.1.6. The MLI tent

The MLI tent is a lowerable cylindrical surface culminating with an insulative ring which must interface with the Lunar regolith. The MLI tent main task is that of surrounding the area under the sublimation plate, where water is being extracted. The MLI tent will create a sealed environment capable of retaining the pressure generated by the water volatiles influx from the ice sublimating inside the regolith, avoiding losses to the the vacuum of the surrounding environment. The pressure inside the tent will not be extremely high, just a few tenths of Pascal, as explained in section 5.4. The capability to fold the MLI tent when the rover is not mining ice will be able to improve mobility, increasing ground clearance. The MLI tent also comes with an additional benefit. In fact, MLI, which have a very low thermal infrared emissivity, will be able to reflect great part of the heat irradiated sideways from the sublimation plate, focusing it to the Lunar surface. In this way, the MLI tent cal also increase the efficiency of the mining process, limiting heat dispersion.

The idea of the MLI tent was inspired from the Mars InSigth mission. Figure 4.7 shows the Mars InSigth seismographic payload thermal shield. In Mars InSigth design the extendable tent is bordered around its lower circumference by a reinforced Kapton and CRES/Aluminum chain mail appendage, designed to conform and seal various terrain obstacles, adapting to ground features in order to provide maximum sealing. The connection between the hot MLI tent and the cryogenic Lunar PSR surface is still an unaddressed problem. The chain mail sealing could be good solution, as it will adhere closely to the ground, following possible small bumps and hills in the local surface. This will minimize openings preventing volatiles leaks.

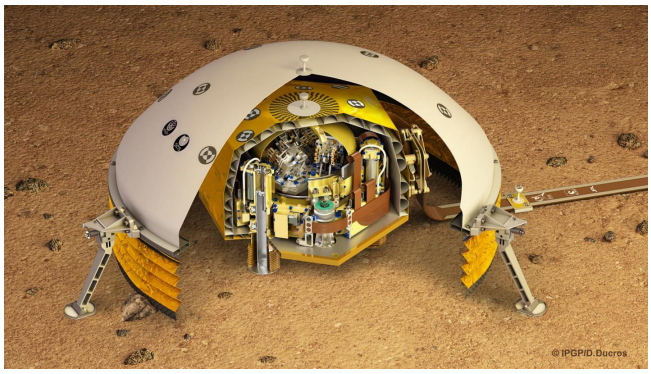

Figure 4.7: Mars InSight seismographic experiment insulated by a deployable MLI tent [115].

Finally, conductive losses should also be contained. This problem is mitigated by the fact that the MLI tent cross-section is very small, and that MLI itself is not very conductive. Furthermore, the regolith where the sealing junction touches the ground would also be at higher temperature than the surroundings, as it is just encircling the thermal extraction area. In any case, more work is needed into the characterization of the sealing interface between the MLI tent and the Lunar surface, which will have to be carried out in future studies.

4.2. Trade-off studies leading to the rover final design

The previous section introduced in detail the designs TMS elements. This section will focus on justifying the most important high level architectural choices, To do so, the trade-off studies conducted during the previous developmental phases of the project will be introduced and discussed. The trade-offs reported in this section follows the chronological order of the ice-mining Lunar rover design process.

4.2.1. DRPS vs. RTG

The characteristics of static thermoelectric conversion and dynamic Stirling engine conversion based RPS have been introduced in subsection 3.3.1, while section 2.1 outlined the two alternatives RPS. They present the following power outputs: $20W_e/380W_{th}$ for solid state thermoelectric conversion and $80W_e/320W_{th}$ for dynamic Stirling engine conversion [20]. The trade-off lies in the amount of energy to be used for ice mining purposing and to power up the rover subsystems. Being the radioisotope the sole energy source available to the rover, great consideration is due in the power budget allocation. Electrical and thermal power budgets must be considered together at the same time, as allocating electrical power to any component will subtract a similar amount of thermal power to rover ice mining operations. For this reason, the two subsystems should be considered as inextricably intertwined [21].

Under this assumption, The low efficiency of the thermoelectric conversion, will leave more power at the thermal state. This can be seen as boost to the rover ice-mining capability at the expenses of a reduced autonomy. The additional electrical power generated employing a Stirling conversion, on the other hand, would prove very useful to improve the mobility of the rover, and to better manage power consumption peaks. Unfortunately, the smaller amount of waste heat would constrain water extraction, and might also pose problems to other subsystems as it could be more difficult to maintain their components in a working temperature range.

Ice-mining Lunar rover electric power budget projections

To select the conversion technology for the ice-mining Lunar rover, similar rover power budget breakdowns have been analyzed in order to develop a preliminary power budget projection for the Ice-mining Lunar rover. Table 4.1 reports the projections. They are based on mass and volume similarities and functional analogies.

Power modes For the time being, only exemplary modes have been considered. They are: pre-Lunar deployment, nominal and peak roving, ice extraction, considered analogous to hibernation and telecomms. This is due to the prospective nature of this work, which did not allow further characterization in light of the present knowledge. Modes duration have also been pro-

	SS Peak power	Pre-Lunar deployment	Nominal roving (∼1cm/s speed)	Peak roving (>1cm/s or climbing)	Ice extraction (or hibernation)	Telecomms
Duration	N/A	∼15 days	∼2 hours	∼30 min	∼2 days	∼10 min
Mobility	40W	-	4W[a]	40W[a]	-	-
GNC	14W	-	6[b]-14[c]W	6[b]-14[c]W	-	4W[c]
OBDH	50W	14[d]-28[e]W	25[d]-50[e]W	25[d]-50[e]W	2[d]-20[e]W	14[d]-40[e]W
TMTC	9W	-	-	-	-	9W[c]
EPS[f]	11W	1-3W	4-7W	7-11W	1-2W	3-5W
TCS	15W	7W[d]	11-15W[g]	11-15W[g]	7W[d]	7W[d]
RPS PCDU	10W	8[e]-10[h]W	8[e]-10[h]W	8[e]-10[h]W	8[e]-10[h]W	8[e]-10[h]W
Rover total	N/A	30-48W	58-100W	97-140W	18-39W	45-75W
Margined total[i]	N/A	36-58W	70-120W	116-168W	22-47W	54-90W

[a] JPL formula (Eq.3.1), [b] Sojourner and Rocky VII, [c] AMALIA, [d] MarsFAST, [e] DRPS VIPER, [f] 10% of previous SS consumption, [g] VIPER base + 1W or 2W motor heating power, [h] usual RPS PCDU parasitc power, [i] 20% uncertainty margin

Table 4.1: Ice-mining Lunar rover projected electric power budget breakdown, with sources.

jected, based on previous rover designs. Ice extraction mode, which corresponds to hibernation and battery recharge mode, is set to last for around 2 days, as indicated in the lierature [22].

Mobility The mobility subsystem power consumption under nominal circumstances (speed of 1 cm/s or less, on flat terrain), is derived by Equation 3.1, and is 1 W per wheel. Having noted that power consumption scales almost exponentially as rover speed or terrain inclination stray from the nominal conditions, it is projected that each engine will consume 10 W when operating under non-nominal "peak roving" situations. The increase of one order of magnitude is justified by what found in similar designs, such as VIPER and AMALIA, where there is reported a substantial increase of power consumption for operations under off-design conditions.

GNC GNC subsystem will be composed of a simple suite of attitude sensors and imaging cameras, as the rover will have a limited speed and does not specifically need the ability to be autonomous, since it could be teleoperated by Earth with less that some seconds of delay. Sojourner and Rocky VII report a power consumption of 6 W for attitude sensors, 7 W for hazard detection and 4.5 W for imaging cameras, while AMALIA camera head total consumption is 4 W idle and 8.5 W during operations. A power budget oscillating between 6 W and 12.5 W have been considered.

OBDH OBDH subsystem power requirements largely depend on the computational load burdening the on-board computer. Rocky VII, a rover with limited computational capacities, required 28 W for nominal operations, while VIPER, a much more advanced rover design with state-of-the-art technologies and presenting autonomous driving capabilities, consumes between 28 and 50 W, depending on the tasks, with the notable exception of the sleep mode, which will consume 20 W. MarsFAST, the ESA design study for a Mars Rover mission, employs a data handling module optimized for reliable mobility and extremely low power consumption

during hibernation: just 2 W. The same module will consume 14 W while active and 25 W while navigating. According to these baselines, a lower power requirement for the ice-extraction phase has been baselined as 2 to 28 W, while a budget of 25 to 50 W has been allotted to roving operations, baselining MarsFAST for the lower and VIPER for the higher end of the range.

TMTC TMTC power consumption is based over an architecture that uses the lander as a relay for Earth or Lunar lander telecommunications. This is done to reduce the power consumption and simplify the rover equipment. AMALIA uses the same TMTC architecture, from which the 8.8 W power requirement has been derived.

RPS The RPS power conversion and regulation is subjected to losses. A good measure of the losses is given by the fact that 10 W is the usual convertor control parasitic power [21]. On the other hand, the DRPS based VIPER rover has a RPS loss of 38 W, reported in Table 3.6. Being the expected power output of VIPER around 335 W_e, 38 W is ∼10% of the RPS power output. Considering the DRPS option for the ice-mining Lunar rover can provide ∼80 W_e, a lower case estimation have been made for 8 W. In any case, both projections are very close.

EPS EPS power consumption represents the losses and inefficiencies of the harness and cabling. Usually, the main source of such losses is the Joule effect due to the cabling resistance. As the rover will be quite small, EPS losses should be contained and have been estimated as 10% of the rover total power consumption, exception made for TCS and RPS budgets. This is thanks to the fact that RPS losses happen before power distribution.

TCS The estimation of TCS power budget is not an easy task. TCS power budget is completely dedicated to heaters and at this stage of the design it is very difficult to know if heaters will be required or not. The WEB and the rover motors are the two areas potentially requiring heaters. For what concerns the WEB, the need for heaters will be heavily dependent on the electric component dissipation. It would be highly desirable that a fraction of RPS waste heat could be used to heat sensitive components. If needed, some Watts should be allocated for heating purposes, especially throughout the ice extraction and hibernation mode, during which WEB internal component dissipation will be limited. Wheel actuators, on the contrary, are hosted inside each wheel hub, and will be exposed to the cryogenic Lunar environment, far away from any heat source. Many rover designs use the same Maxon engine, which is heavily insulated from the environment and do not mention any need for heating. On the other hand, many rovers are equipped with heaters as the motors cannot drive at temperatures lower than -80°C, and that it is beneficial, if not outright necessary, to warm up the motors before driving. Hence, a maximum allowance of 2 W of heating power per motor has been budgeted. Furthermore, the whole VIPER rover TCS budget of 6.8 W has been summed up to derive the TCS power requirement. As VIPER is a very large and much more complex rover than the ice-mining Lunar rover, this estimation is strongly conservative.

Finally, a 20% margin has been applied to the resulting power balance to reflect the uncertainty over the considered baselines. Larger margins were considered but eventually discarded as the majority of the other designs already have their own margins incorporated.

Even though the power requirements in Table 4.1 are very conservative, it emerges the need for the dynamic conversion alternative, based on the Stirling technology and able to provide $\sim$80 W_e. The choice will have repercussions on the extraction capabilities of the rover, slightly limiting the sublimation plate dimensions.

4.2.2. Volatiles tube vs. lowerable cold trap

The method of delivery of the extracted volatiles from the high temperature area under the sublimation plate, inside the pressurized environment of the MLI tent, to the low temperature portion of the TMS, is very important. Depending on the selected architectural choice, heat losses to the cryogenic environment and heat leaks to the cold trap could increase, as well as the extracted water volatiles could be lost the vacuum of the Lunar environment.

After a literature survey, two volatiles delivery methods were shortlisted to be employed on the ice-mining Lunar rover: the volatiles tube and the lowerable cold trap, a sketch of the two alternatives is reported in Figure 4.8. The figure reports an earlier iteration of the volatiles tube method, which was eventually preferred, and which has been previously presented in the final form. This subsection will focus on the trade-off performed by comparing the two alternatives, and the reasons for the choice of the former.

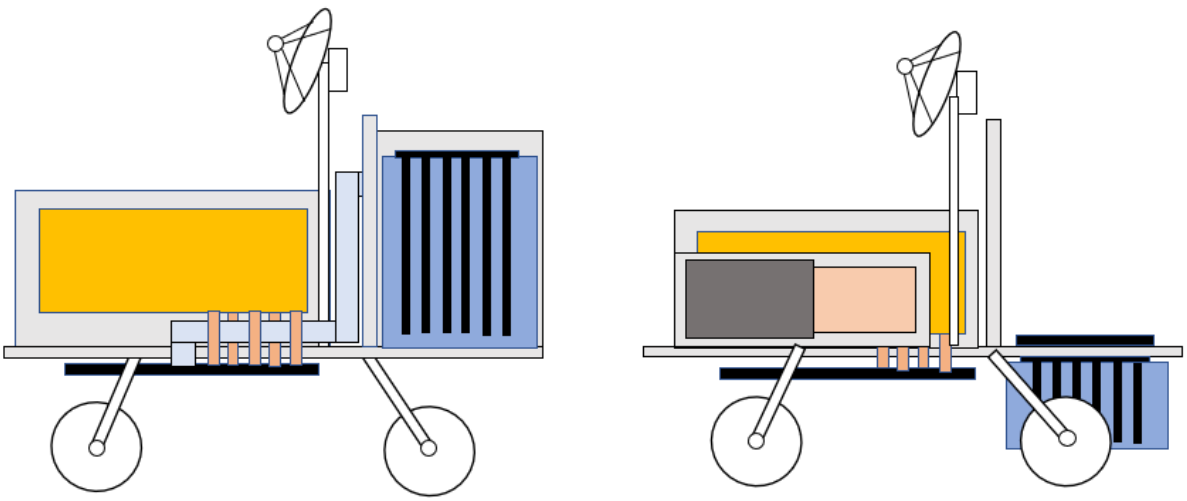

Figure 4.8: A sketch of the two volatiles delivery concepts: the volatiles tube, on the left, and the lowerable cold trap, on the right. DRPS and other warm items are in orange, sublimation plate is in black, and cold trap is in blue, on the front side of the rover.

The volatiles tube and its integration with the TMS and the rover has been already presented in the previous section. Its pros and cons can be summarized with:

- Easy integration of the MLI tent with the rover;
- The cold trap is at equipment level, no problems in case of difficult terrain;
- The cold trap radiator area can be bigger, as all its sides facing outside could be employed for rejecting volatiles deposition latent heat;
- The volatiles tube must be kept at a temperature higher than the ice deposition temperature for its whole length, to avoid occlusions;
- There is a physical connection between the sublimation plate and the cold trap, paving the way for undesired direct heat leaks.

The lowerable cold trap concept, instead, is composed of a cold trap mounted on a ladder and connected to a series of actuators able to change its elevation with respect to the ground. Volatiles enter in the cold trap through a slit on the side facing the sublimation plate. The MLI tent is also part of this mining architecture, as its absence would dictate that an extremely large portion of the extracted ice is lost to the surrounding environment. The actuation per se is not a problem, as it has been calculated that the power required to raise the box up under the weaker lunar gravity would be negligible. The criticalities of this design, which would prevent unwanted heat transfer through the tube, are many, first of all the integration of the movable cold trap box with the MLI tent. They are listed here:

- Lower losses through conduction as there is no direct physical connection with the plate;
- Higher heat leak from the plate to the cold trap, as one irradiates the other
- The cold trap volume is developed horizontally, with a balancing effect on the CoM;
- Very difficult integration of the MLI tent, due to the cold trap volume presence under the rover insulating plane, which could cause unwanted volatile losses;
- Need for actuation to raise the cold trap upwards during roving, which would also be susceptible to the damaging effect of lunar regolith dust;
- Might face deployment difficulties in case of rugged terrain underneath, due to the very small final clearance from ground;
- Its size would be restricted in height: the cold trap would need to develop horizontally, relegating the WEB to the other side of the adiabatic wall.
- Smaller radiator area as now the view to the surrounding environment on the two cold trap lateral sides is obstructed by the mobility system.

Table 4.2 shows the Simulink results for the two design alternatives compared with each other, based on an earlier iteration of the thermal network presented in chapter 6. Of the three

reported nodes, it is possible to see how how the second option, the lowerable cold trap design, results in a DRPS radiator and plate temperature higher than the first option, the volatiles tube alternative. This is not desirable as it decreases the conversion efficiency of the Stirling convertor. The second design option also presents higher heat leakages, mainly due to a view factor radiative connection between the two. On the other hand, heat conductivity through the tube can be limited to less than 1 W by employing a copper 2 mm wall tube, paired with thermal washer sleeve to be fitted on the tube as interface with the cold trap. Hence, the first option will present a slightly higher TMS efficiency.

Node		Volatiles tube	Lowerable cold trap
DRPS	Q_{DRPS}	326 W	331 W
	$T_{DRPS\ Rad}$	255 °C	285 °C
Sublimation plate	Q_{Plate}	296 W	287 W
	T_{Plate}	253 °C	282 °C
	η_{TMS}	90.8%	86.7%
Cold trap	$Q_{Deposition}$	144 W (5% ice vol.)	144 W (5% ice vol.)
	$Q_{Leakages}$	$\leqslant$ 1 W	20 W (sublimation plate radiation) $\cong$ 1 W (other sources)
	$Q_{Rejected}$	145 W	166 W
	$A_{Radiator}$	1.00 m^2	0.70 m^2
	$T_{Radiator}$	-43 °C	-12 °C
	T_{Ice}	-40 °C	-9 °C

Table 4.2: A comparison of the Simulink results for the two design alternatives.

Finally, the most important factor disqualifying the lowerable cold trap design is a direct result of its lower area available for radiators. In fact, this design allows a final radiator area 30% lower than for the other alternative, resulting in a ice temperature of just -9 °C, which does not meet the core requirement outlined in section 2.2. This, paired with the increased difficulties in integrating the movable cold trap with the MLI tent, identified the volatiles tube design as the alternative of choice.

4.2.3. Two-ways vs.single-way TMS architecture

Another trade-off regards the possibility of developing a more complex two paths system for the TMS, in which RPS waste heat could be directed away from the sublimation plate and radiated to the sky. This would effectively turn off any mining capability. The alternative to the previous design would be a simpler and more efficient single way heat transfer architecture, where heat could only flow from the RPS hot end to the sublimation plate, situated under the belly of

the rover. This design choice implications can have important ramifications impacting on the whole mission. A two way TMS architecture would increase the complexity of the thermal management system, but the ability to switch off the sublimation plate during non-extraction phases would help preserving intact any ice deposit the rover would be moving over during its travels back and forth to the lander or reference station, to which he would have to deliver the extracted water. To decide if this capability is actually needed, a trade-off has been considered, balancing the risk of the rover depleting an ice deposit while passing over it against the more cumbersome functioning of a more complex TMS.

The drawbacks of a two ways heat transfer architecture are not univocally defined, as their precise nature depends on how the second heat transfer pathway is implemented. The first solution is a system making use of heat switches, such as paraffin wax heat switches. This system has the merit of not needing any moving part (especially in the case that a paraffin switch actuator is used), while maintaining a good heat rejection capability. The second solution encompasses a rotatable shield, made of insulating material and/or coated by a reflective MLI blanket, which would obstruct the view to the RPS hot end either from the sublimation plate or from the heat rejection plat. This system would have an excellent efficiency in redirecting heat were desired, but Lunar dust could infiltrate its mechanisms, making it quite unreliable. Furthermore, the presence of concave shapes would offer a place where dust could gather, and this could impede heat shield movements and also alter surfaces thermal performances, as it happened with the Lunar rover Lunokhod 2. Finally, a more sophisticated approach, inspired from NASA Mars Science Laboratory (MSL) [92], is presented. In this design the RPS hot end is encapsulated between two plates, called hot and cold plate. The function of the inner one (hot plate) is to gather the heat from the RPS and to direct it to the sublimation plate for ice extraction. The outer one (cold plate), would be connected to the heat rejection plate facing the sky and would be posed directly adjacent to the hot plate. The two plates would be separated by a paraffin wax actuated heat switch, which while turned off would block the transfer pathway to the cold plate and the heat rejection plate. Otherwise, when the switch would be turned on, an alternative path would be connected to the heat source, siphoning some thermal energy and letting the sublimation plate temperature decrease. This system, although quite complex, has merit, besides it fairly high effectiveness, of not having any moving part.

Another solution, which could be employed with limited effectiveness but also limited drawbacks, would be the installation of a louvered radiator on top of a hard insulative shell, as outlined in subsubsection 4.1.1. This option has the benefit of not requiring a well defined architectural choice constraining the rover development and could also be added in the future, without any provision to be taken in this phase of the project.

The decision between the two architectural alternatives takes into account how fast can the

rover move and how far away would the rover need to go. Depending on parameters such as the distance that the rover needs to travel and its speed, a rough estimate of the time elapsed while roving could be obtained and compared to the extraction time, which is in the order of days [22]. In summary: if the ratio between the roving time and extraction time is high, a further investigation over how much of an ice deposit might the rover deplete while passing over a plot of Lunar soil could be warranted, so to make an informed decision over the matter. Otherwise, if roving time is one or more order of magnitudes smaller than extraction time, it is very likely that the potential benefits in terms of ice deposit left intact would not be worth the increased complexity of a two-way heat transfer architecture. Hence:

$$\text{If } \frac{t_{Roving}}{t_{Mining}} > 1 \longrightarrow \text{2-ways alternative can be considered} \tag{4.1}$$

Assuming an exemplary roving distance of a hundred of meters, covered at an average speed of 1 cm/s, it would take the rover less than 3 hours to traverse it. As already reported in the previous paragraph, it would instead take around 2 days to deplete a 5 to 10% ice vol. deposit. This comparison, in which the roving time is one order of magnitude lower than the extraction time, already indicates that there is no need for a two-ways thermal management architecture.

Furthermore, the decision of not developing a two-ways heat transfer architecture is also backed up by the dynamics of the extraction process. In fact, unmarred Lunar regolith will be at very low temperature, and will have quite a sizeable thermal inertia, hence, the transient during which the regolith is heated up will be quite long. It is reasonable to think that a fast passage of the sublimation plate, even if irradiating at full regime, will not be able to bring the underlying regolith to a temperature high enough to start ice sublimation in the time it will transfer heat to the same patch of terrain. This last considerations further corroborates the single-way heat transfer TMS architectural choice.

5 | Thermal balance description and model boundary conditions

This chapter will focus on introducing the boundary conditions of the PSR cryogenic environment where the rover is going to operate. It will also describe the thermal steady state balance of the various scenarios the rover could encounter during the ice-mining operation, with their different heat loads. Figure 5.1 shows the thermal environment in which the rover is set to operate. The PSR regolith is at a very low cryogenic temperature of 40 K, as reported by many sources found in the literature review [16, 17]. PSR craters are characterized by the absence of sunlight. There are no environmental heat sources directing heat on the rover. The only exception is a very faint heat flux originating from the geological processes still ongoing in the Moon core. Nevertheless, its magnitude is very low, amounting to only 0.031 W/m^2 [116].

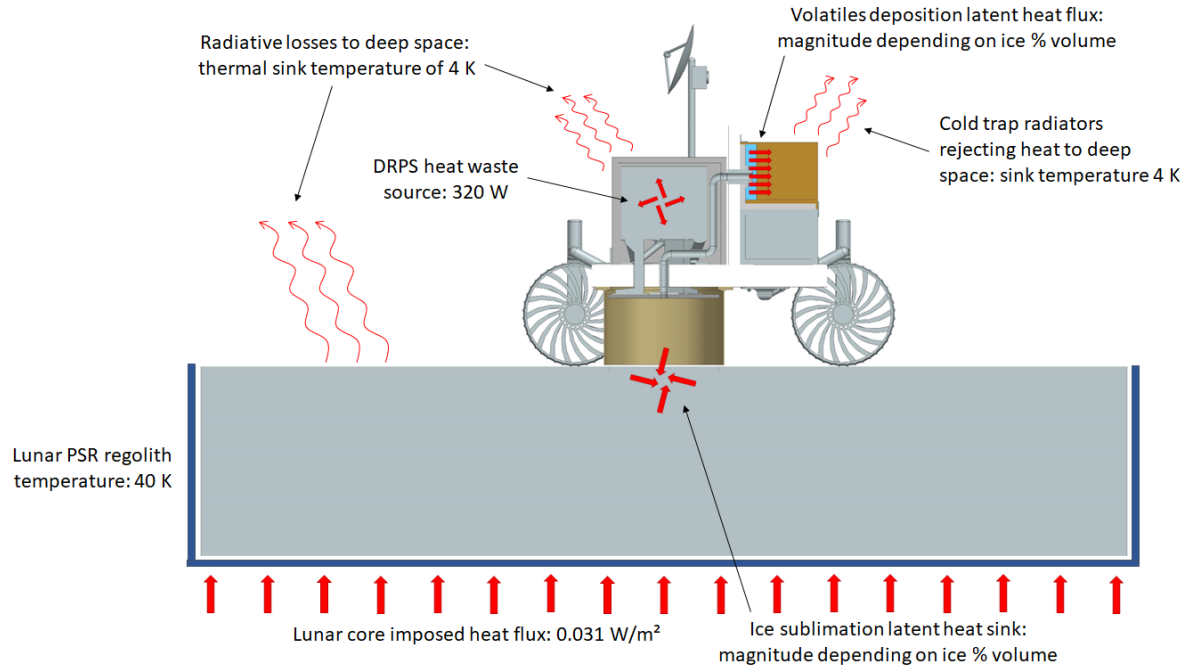

Figure 5.1: The ice-mining Lunar rover in the thermal environment of the PSR, with its environmental boundary conditions and the heat loads on the TMS.

Conversely, Lunar PSR presents plenty of sinks: heat is easily lost to the surrounding environment, be it through conduction or irradiation. Regolith itself has a very high emittance, and will effectively reject to a 4 K heat sink deep space sky the surplus heat radiated from the sublimation plate for extraction purposes. Also the rover sees deep space, and all its surfaces will lose heat by radiation too, in the same way as the regolith. This can be desirable, such as in the case of the cold trap, but can also be a problem for the TMS design, like in the case of the DRPS sleeve, which has the aim of retaining heat.

Finally, Figure 5.1 also reports three heat loads representing the TMS heat sources and sinks during ice-mining operation, when thermal steady state has been reached. The first one, which is the only one independent by the local regolith ice content in % vol., is the DRPS waste heat. It is the only heat source in the whole simulation, apart for the virtually negligible Lunar core imposed heat flux. Its magnitude is 320 W. The other two elements presented in Figure 5.1 will vary in intensity depending on the regolith ice content. The one located in the regolith, under the sublimation plate, is a thermal sink element, representing the latent heat subtracted from the surrounding regolith by the sublimating ice. In the Siemens NX thermal analysis, it has been considered as a negative volumetric heat generation term, measured in W/mm^3. The other one, located inside the cold trap, represents the latent heat flux brought in the cold trap by the depositing volatiles. It has been materialised as a heat flux, measured in W/mm2. It can be calculated by dividing the ice sublimation latent heat by the cold trap inner surface. Both terms vary in magnitude according to the regolith ice content, with higher amounts meaning higher extraction rates, resulting in increased thermal loads on the cold trap.

5.1. The regolith model

The Lunar regolith has peculiar thermal properties, which must be taken into account in the design of the ice-mining Lunar rover TMS. The baseline for the regolith thermal and radiative properties has been taken as the model shown in Figure 5.2 [116]. Lunar surface is comprised of two layers, the upper one, called fluff, is composed by fine silicate particles, having a density half of the underlying regolith, made of the same silicate mineral, but coarser and denser. This model is the one NASA uses to simulate Lunar thermal environment at different latitudes [116].

The upper undisturbed fluff layer presents a low conductivity at the cryogenic temperatures of the Lunar PSR. Heat transfer in the fluff layer is mainly due to particle radiation: conductivity is highly temperature dependent, increasing with it [116]. Fluff has an absorbivity of 0.87, meaning that 87% of the incoming Solar radiation is absorbed by the regolith. This translates in an albedo factor of 0.13. The Solar radiative heat flux depends on the sunrays incidence angle ϕ, as illustrated in the formula in Figure 5.2. In the case of PSR, there is no incoming Solar radiation. Regolith can radiate heat to deep space with an infrared emissivity of 0.97.

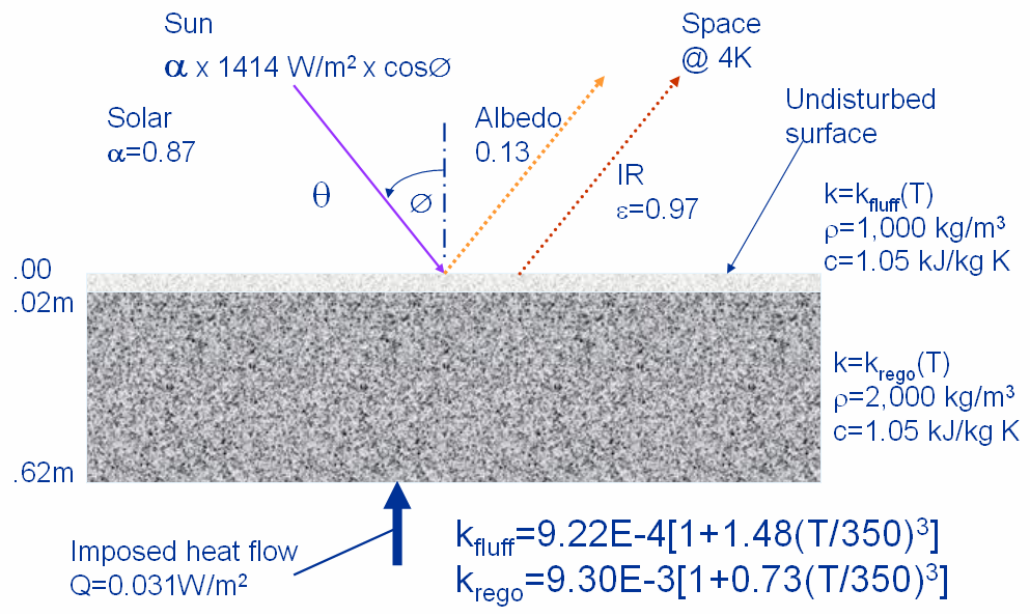

Figure 5.2: Thermal characteristics of Lunar surface [116].

The fluff layer, which is 2 cm thick, covers a 1 m deep consolidated regolith layer. The depth of the regolith layer has been increased from the 0.6 m of the literature source to 1 m as it has been considered that ice sublimation will happen within a regolith cylinder as large as the MLI tent, and 0.5 m deep. The remaining regolith depth has been added in order to mode away the model boundary, on which a constant temperature boundary constraint has been applied, as illustrated in Figure 5.1. The lower regolith layer is denser, so conductivity is favoured. Conductivity is still mainly driven by particle radiation, hence the same temperature dependence as in the fluff case is present, although the increased density reflects on regolith being roughly one order of magnitude more conductive than fluff, as it is evident from the two conductivity formulas reported below:

$$k_{fluff} = 9.22 \cdot 10^{-4} \left[1 + 1.48(T/350)^3\right] \tag{5.1}$$

$$k_{regolith} = 9.30 \cdot 10^{-3} \left[1 + 0.73(T/350)^3\right] \tag{5.2}$$

Finally, a heat flow from the interior of the Moon is applied to the base of the regolith slab in the model. Such flow is justified by the subsurface temperature measurements taken by Apollo 15 and 17, which detected an increase of temperature with depth. Hence, an imposed heat flow from the Lunar core is applied, with an intensity of 0.031 W/m^2 [116].

5.2. The ice model

A formula for ice thermal conductivity can be retrieved from the literature. Hexagonal ice (Ih), cubic ice (Ic) and ice XI are the only crystalline ices that can be produced at atmospheric or

lower pressures [117]. Hexagonal ice, whose temperature stability range extends from 273 K down to 40 K, is dominant at higher temperatures, while it can coexist with its other two forms at lower ones. This is especially true for ice XI, which can form when temperatures fall lower than 70 K from hexagonal ice, even though only a fraction of it will transition from Ih to XI [117, 118]. For simplicity, the following formula for ice conductivity will be adopted [117]:

$$k_{ice} = a/T + b + cT \tag{5.3}$$

Where a = 632 W/m; b = 0.38 W/(m·K) and c = -0.00197 W/(m·K^2). This formula is a mathematical fit of a set of empirical results, with an accuracy of 5%. It has been derived measuring the conductivity of prevalently hexagonal phase ice, with a temperature validity range spanning from 40 K to 273 K [117].

Figure 5.3 shows the thermal conductivity plotted for the various forms of regolith. The temperature range for the conductivity values employed for the NX thermal simulations span for 500 degrees, starting from 40 K: the constant temperature boundary condition at the external edges of the regolith slab. Figure 5.3 also shows the temperature evolution of ice conductivity, plotted along its validity temperature range from 40 K to 273 K.

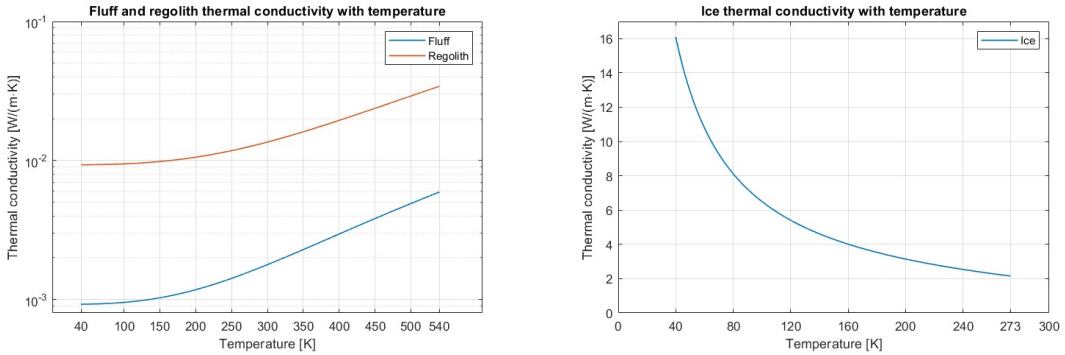

Figure 5.3: Thermal conductivity of fluff, regolith and ice depending on temperature.

5.3. Extracted volatiles mass flow rates

Once the regolith model has been laid out, and all the environmental boundary conditions have been presented and explained, it remains to define the steady state balance heat loads constraining the rover TMS. The loads are, as introduced at the start of this chapter, the DRPS heat source, the sublimating ice thermal sink, in the regolith, and the depositing volatiles latent heat flux, on the cold trap. Of the three, the first one is constant (320 W), while the magnitude of the latter two will vary according to the amount of extracted water, which is in turn proportional to the percentage of ice volume in the regolith. As a simulation of the thermal behaviour of the heated icy regolith would require an in depth characterization of the various physical phenomena governing heat exchange and volatiles outgassing, such a task is

beyond the scope of this work. Hence, relevant data, such as the amount of volatiles mass flow rate extracted in each mining scenario, has been gathered through a literature survey.

Table 5.1 shows the mass of ice extracted and the time to do so, among many other data, for regolith with ice contents of 1%, 5% and 10% in volume [22]. The data reported in the table are referred to the researchers model results for thermal ice mining performed by uniform irradiation of the Lunar regolith by a 1.2 m by 1.2 m (1.44 m^2) sublimation plate. The depth of the regolith in the model is 1 m. The results reported in the table shows how 1000 W is the best power level for ice mining, outclassing even the one order of magnitude higher power level of 10000 W, which presents lower recovery rates than the former option. This is a further confirmation of the 1 kW/m^2 heat flux requirement.

Power [W]	Ice [vol%]	Duration [s]	Mass [kg]	% Total	Max. Temp. [K]
100	1	500,040	$9.71 \cdot 10^{-7}$	0	205.1
100	5	500,040	$9.78 \cdot 10^{-7}$	0	205.1
100	10	500,040	$9.88 \cdot 10^{-7}$	0	205.1
1000	1	500,040	2.48	17.22	366.0
1000	5	163,440	42.65	59.24	389.8
1000	10	184,770	69.71	48.41	392.0
10000	1	499,990	2.94	20.43	648.0
10000	5	30,800	14.78	20.53	648.0
10000	10	26,970	41.33	28.7	648.0

Table 5.1: Extracted ice mass, mining time, percentage of extracted ice and maximum regolith temperature, depending on heating power budget and regolith ice content [22].

Data from Table 5.1 can be adjusted to be used for the ice-mining Lunar rover thermal analysis, in order to derive the magnitude of the sublimating ice thermal sink inside the regolith and the depositing volatiles latent heat flux on the cold trap. First, the extracted ice mass must be rescaled to account for the smaller size of the sublimation plate, which is 0.28 m^2, instead of 1.44 m^2. Then the rescaled ice mass can be divided by the extraction time, still unchanged, to obtain the volatiles mass flow rate at steady state. Finally, considering a latent heat of sublimation of $2.8 \cdot 10^3$ kJ/kg [22], relevant heat loads can be calculated.

Table 5.2 shows the results of the rescaling process. The two variable heat loads, namely the sublimating ice thermal sink and the depositing volatiles heat flow terms, can be calculated by dividing latent heat by the relevant surface or volume. In the first case, the volume of the regolith in which ice is being extracted, a cylinder of base 0.28 m^2 and height 0.5 m, is to be

considered. In the second case, the calculation takes into account the finned area inside the cold trap, where ice deposition will happen, which is roughly 1.2 m^2 wide.

Ice [vol%]	Time [s]	Rescaled Mass [kg]	Mass flow rate [kg/s]	Latent heat [W]	Sublimating ice thermal sink [W/mm^3]	Depositing volatiles heat flow [W/mm^2]
1	500,040	0.48	$9.6 \cdot 10^{-7}$	2.7	$-1.93 \cdot 10^{-8}$	$2.24 \cdot 10^{-6}$
5	163,440	8.29	$5.1 \cdot 10^{-5}$	143.9	$-1.02 \cdot 10^{-6}$	$1.19 \cdot 10^{-4}$
10	184,770	13.55	$7.3 \cdot 10^{-5}$	208.1	$-1.48 \cdot 10^{-6}$	$1.72 \cdot 10^{-4}$

Table 5.2: The ice-mining Lunar rover rescaled extracted ice mass, total sublimation latent heat, and the regolith thermal sink value, with the correspondent heat flow in the cold trap.

From the final results, it can be seen how the amount of water extracted from the regolith in case ice is present at only 1% in volume is very meagre, while the extraction time extends for more than 5 days. The related heat loads are 2 orders of magnitudes lower than in the other two cases. Hence, an attractive quantity of ice can be mined only in the two other cases: icy deposits of 5% and 10% in volume. In this case, the the latent heat to be subtracted from the total irradiance of the sublimation plate is in the order of one or two hundreds. This is less than the DRPS heat waste, 320 W, so thermal mining is feasible in both cases, provided that heat losses are not overwhelming. The mining operations will take roughly 2 days, leaving plenty of time for the process to reach the steady state, which will be the object of this simulation.

5.4. Pressure balance in the MLI tent

Once the baseline for the extracted volatiles mass flow rates have been identified, it is possible to calculate the projected pressure inside the MLI tent. Such procedure is necessary for two purposes. The first one is to have an idea on the order of magnitude of the pressure which will be established once the balance between the incoming and outcoming mass flow rates will be reached. The result can be compared with the literature to explore the feasibility of the MLI tent concept. The second scope of this analysis is to determine the temperature range at which the volatiles will start to deposit on the cold trap fins, in order to perform cold trap radiator sizing. In fact, the deposition temperature is strongly influenced by the pressure at which the volatiles are kept. Figure 5.4 shows that the maximum temperature for deposition is increasing with pressure over a range of 40 degrees in the 1 Pa to 100 Pa interval, then tending to 0°C in the proximities of the triple point, at slightly more than 600 Pa [119].

The extraction process is presented in Figure 5.5. The considered scenario is the heliostat based thermal mining introduced in subsection 3.2.2, but as far as volatiles mass flow rates are concerned, the phenomenon is conceptually identical to the ice-mining Lunar rover. The process can be described by the following differential equation [120]:

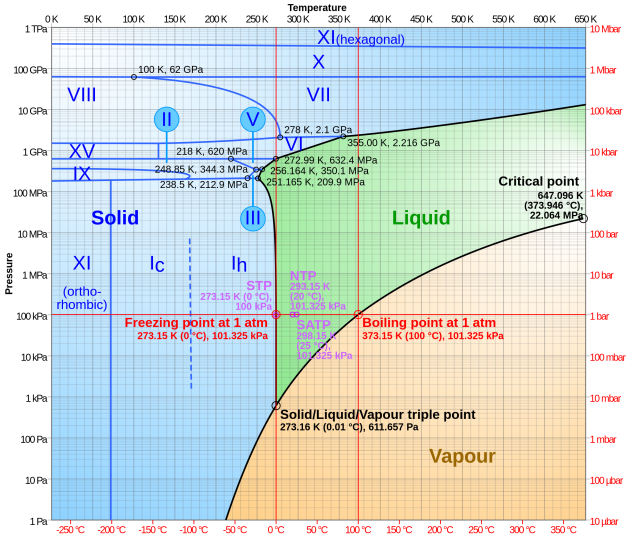

Figure 5.4: Water state-phase diagram [119].

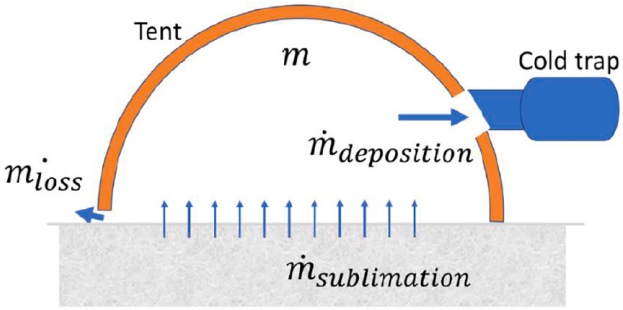

Figure 5.5: Mining mass flow rates [120].

$$\frac{dm}{dt} = \dot{m}_{sublimation} - \dot{m}_{deposition} - \dot{m}_{loss} \tag{5.4}$$

The change of water volatiles mass in the tent over time is expresses and the sum of incoming and outcoming mass flow rates, namely $\dot{m}_{sublimation}$, the extracted volatiles incoming mass flow rate from Table 5.2, and two negative terms, representing the water volatiles leaving the tent: $\dot{m}_{deposition}$ and $\dot{m}_{loss}$. The former stands for the depositing volatiles mass flow rates, the latter represents the losses, due to imperfect sealing and the vacuum of the outside environment, which cannot be completely prevented. These two terms can be considered deriving from an effusion process, and can be estimated with the following formula [120]:

$$\dot{m}_{deposition} = P \cdot A_{coldtrap} \sqrt{\frac{M_{H_2O}}{2\pi RT}} \tag{5.5}$$

where P is the pressure inside the MLI tent and A is the area through which the volatiles pass. It can be the area of the openings of the cold trap for $\dot{m}_{deposition}$, while it is the area open to losses for $\dot{m}_{loss}$. M_{H_2O} is molar mass of water, R is the ideal gas constant and T is the temperature of the water molecules. Equation 5.4 can be rewritten by substituting the mass in the derivative with the pressure thanks to the ideal gas law. The result is the following first order ordinary differential equation (ODE) of pressure as a function of time:

$$\begin{gathered} \frac{dP}{dt} = -A \cdot P + B \qquad\qquad where \\ A = \frac{A_{coldtrap}}{V}\left(1 + \frac{\%_{loss}}{100}\right)\sqrt{\frac{RT}{2\pi M_{H_2O}}}; \qquad B = \frac{RT}{M_{H_2O}V}\dot{m}_{sublimation} \end{gathered} \tag{5.6}$$

Equation 5.6 can be solved to obtain the time evolution of pressure inside the tent. $A_{coldtrap}$ is

the area of the opening of the volatiles tube, a circle of 2 cm radius. The percentage of losses has been selected as 10% of $A_{coldtrap}$, while the water molecules temperature has been considered to be 220 K [120]. Figure 5.6 reports the pressure evolution until steady state has been reached, for the three investigated ice volumetric concentrations. The pressure generated under the tent by ice-mining with 1% in volume icy regolith is negligible, less than 1 Pa, this pressure corresponds to a deposition temperature of ∼210K (∼ -60°C). Conversely, 5% ice vol. and 10% ice vol. regolith mining leads to final equilibrium pressures of 30 Pa and 42 Pa, corresponding to a deposition temperature of ∼240K (∼ -30°C) and ∼250K (∼ -20°C), respectively. These temperatures will drive the development of the cold trap, providing a baseline for a target temperature to prove feasibility of concept for the ice-mining Lunar rover and its TMS.

Pressure inside the MLI tent might not evolve to reach steady state in a few seconds since the start of the extraction operations. In fact, the derivation of the volatiles mass flow rate only aims at a first order of approximation characterization of the steady state operations. In reality, there will be a transient in which regolith must be heated up first to reach sublimation temperature, during which the extracted volatiles mall flow rate will be negligible or much lower than the figures calculated in Table 5.2 and used to obtain the results of Figure 5.6.

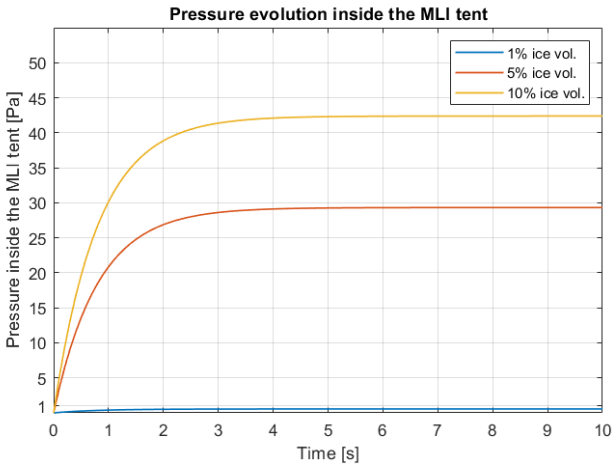

Figure 5.6: The pressure evolution inside MLI tent.

Finally, the design of the cold trap, which is heavily influenced by the pressure balance in the MLI tent, is aided by a negative feedback loop established between pressure and deposition temperature, contributing to the stability of the system and enabling the cold trap to work at the maximum possible efficiency, safeguarding against pressure increase. The phenomenon works in the following way. Considering steady state equilibrium have been reached, if the pressure inside the MLI tent increases, the volatiles deposition maximum temperature is also increased. In the case the cold trap were working near to its saturation point, which means that the new higher inflow of volatiles is bringing enough heat to increase the local temperature over the deposition temperature, the growth in pressure also raises the maximum deposition temperature by a few degrees, accommodating for the higher amount of volatiles to be deposited, and causing pressure to decrease again by regressing to the previous steady state when the inflow is reduced back to the previous amount.

This could also work in case an even richer ice deposit, presenting more than 10% ice in volume,

were to be mined. In this scenario the TMS would work in an off design condition, but until the increase of pressure does not directly threaten the MLI tent structural stability, it would be beneficial in favouring volatiles deposition by raising the deposition temperature. The growth in pressure would also stress the tent sealing and increase losses, so that a dynamical equilibrium is reached even in off-nominal conditions. A vent valve, or similar, could also be fitted on the rover as part of the MLI tent, in order to actively control similar scenarios.

5.5. Final considerations on the mining heat loads

The thermal loads calculated in Table 5.2 have been based on the expected ice extraction rates extrapolated from the literature. They only work for the simulation of steady states scenarios, establishing the model boundaries with the aim of delimiting the temperature evolution of ice-mining phenomenon between the starting and ending scenarios. In fact, the steady state thermal analysis performed in this work strive to characterise the hot and cold case for the extraction operations. The time dependent evolution of the regolith and rover temperatures during ice-mining will be constrained by the results of the cold and hot scenarios. This is enough to study the feasibility of the ice-mining Lunar rover concept, while it can also provide a large amount of data to be employed in the future phases of the work. Hence, this work will not dwell on transients, leaving their study to for a future developmental phase.

The next two chapters will present the results of the thermal analysis, conducted on Simulink and Siemens NX. Four cases have been considered for the rover in the ice-mining configuration: the extraction on icy regolith presenting 1%, 5% and 10% ice vol. concentrations, and the irradiation of dry regolith, without any ice being extracted.

The dry regolith mining case will be employed as a baseline on the rover thermal situation at the start of the mining process, when regolith is being heated up and no ice have been sublimated yet. This will be considered as the cold case for the rover TMS, as there is not heat flux incoming on the cold trap. The other three simulated scenarios will reference to the ice-mining operations at full regime, when steady state has been reached. This scenario can be reconducted to a mid-extraction situation, in which regolith has been heated and ice is sublimating, but a sizeable amount of ice is still present inside the regolith, so that the extraction can proceed with similar recovery rates for some hours at least. This will be considered as the hot case for the rover TMS, since thermal loads are now applied as the cold trap is flooded with an inflow of hot volatiles that need to be deposited on its fins.

Anything happening between the cold and hot case scenarios is ignored, for the time being. This can be safely done since the temperature is bound to evolve from the cold case to the hot case and viceversa, which represents the two extreme situations.

6 | The rover SIMULINK thermal model

This chapter will introduce the rover Simulink thermal model. Only the final version of the Simulink will be presented, even though both the Simulink and the Siemens NX models were developed and iterated next to each other. Simulink allows for the design of simple 1D thermal networks, employing basic components such as temperature or heat sources to exemplify the system boundary conditions, and three main building blocks regulating heat exchange: conduction, convection and irradiation.

Convection has not been considered in the rover model. This is justified by the fact that the Moon has no atmosphere, while the volatiles inside the tent, the tube and the cold trap are too rarefied to transfer non-negligible amounts of heat. Conduction is modeled as a 1D phenomenon, where heat is transferred through a layer of material. The rate of heat transfer is governed by Fourier's law and is proportional to the temperature difference, ΔT, the material thermal conductivity, k, the area normal to the heat flow direction, A, and inversely proportional to the layer thickness, t:

$$Q = \frac{kA}{t}\Delta T \tag{6.1}$$

Finally, radiative heat transfer between two surfaces is governed by the Stefan-Boltzmann law and is proportional to the difference in the fourth power of the temperatures of the two surfaces, T_1 and T_2, their emissivity, ε_1 and ε_2, their areas, A_1 and A_2, and their relative view factor. The previous amounts are scaled down by the the Stefan-Boltzmann constant, σ, equal to $5.76{\cdot}10^{-8}$ $\mathrm{W/(m^2{\cdot}\ K^4)}$. The Stefan-Boltzmann law can be expressed in different ways according to the radiative scenario. The following equation is a simplification considering only radiation from a surface at temperature T_1 to a thermal sink at temperature T_2, such as in the case of radiative losses to deep space:

$$Q = \sigma\varepsilon A(T_1^4 - T_2^4) \tag{6.2}$$

The same equation can become more complicated if radiation between two surfaces is considered. In this case the balance between the two surfaces view factors, F, must be considered. The view factor from an object to another can be defined as the fraction of the radiation outcoming

from the former impinging on the latter, hence, it will always be a number between 0, meaning that the two objects do not exchange heat, and 1, meaning that the second object completely surrounds the first one. To account for the aforementioned phenomenon, a term called radiation coefficient appears in the Stefan-Boltzmann equation: the longer expression between brackets in Equation 6.3. The radiation coefficient depends on the geometric configuration and surface emissivities of the interacting bodies. It can be derived from the solution of the thermal balance for the radiative exchange between the two bodies:

$$Q = \sigma\,(T_1^4 - T_2^4) \cdot \left(\frac{1-\varepsilon_1}{A_1\varepsilon_1} + \frac{1}{A_1 F_{1-2}} + \frac{1-\varepsilon_2}{A_2\varepsilon_2} \right)^{-1} \tag{6.3}$$

Finally, Equation 6.3, which is the most general form of the Stefan-Boltzmann equation, can be simplified under the assumption of parallel plates at a close distance, to the following formulation:

$$Q = \frac{\sigma A (T_1^4 - T_2^4)}{1/\varepsilon_1 + 1/\varepsilon_2 - 1} \tag{6.4}$$

Simulink Simscape rewrites the Stefan-Boltzmann equation in the radiative heat transfer block source code factorising the quadratic term into a sum of squares and difference of squares, which can be further decomposed into the product of the sum of the two temperatures and their difference, as shown in Equation 6.5, The absolute value is to avoid spurious solution in the quartic equation [121]. The product of k and A, respectively called radiation coefficient and radiating surface area, contain the geometry of the heat transfer and can be reconducted to all the terms left out of the quadratic temperature difference of the previous equations:

$$Q = kA(T_1^2 + T_2^2)(|T_1 + T_2|)(T_1 - T_2) \tag{6.5}$$

Once all the model components have been laid out and connected to each other, the system looks like the one presented in Figure 6.1. Each rectangle represent a subsystem, modeling a part of the rover. The subsystems are color coded according to the designer expectation on the local temperature, and are connected to each other by radiative and connective couplings. The most influential ones have been summarized by arrows linking two different areas of the model: they are also color coded: warm colors for the encouraged heat transfer pathways and cold colors for the heat leaks, which are curbed by insulation. Smaller red and blue bubbles, located on the bottom left corner of some subsystems, represents the active thermal sources or sinks, as explained in the previous chapter. Finally, the environmental boundary conditions are portrayed by sharp edged rectangles, they can represent PSR regolith or deep space sky. The rover will transfer heat by irradiation to all of these sinks, except for one case: conduction through the wheels, due to the physical connection between the grousers and the Lunar soil.

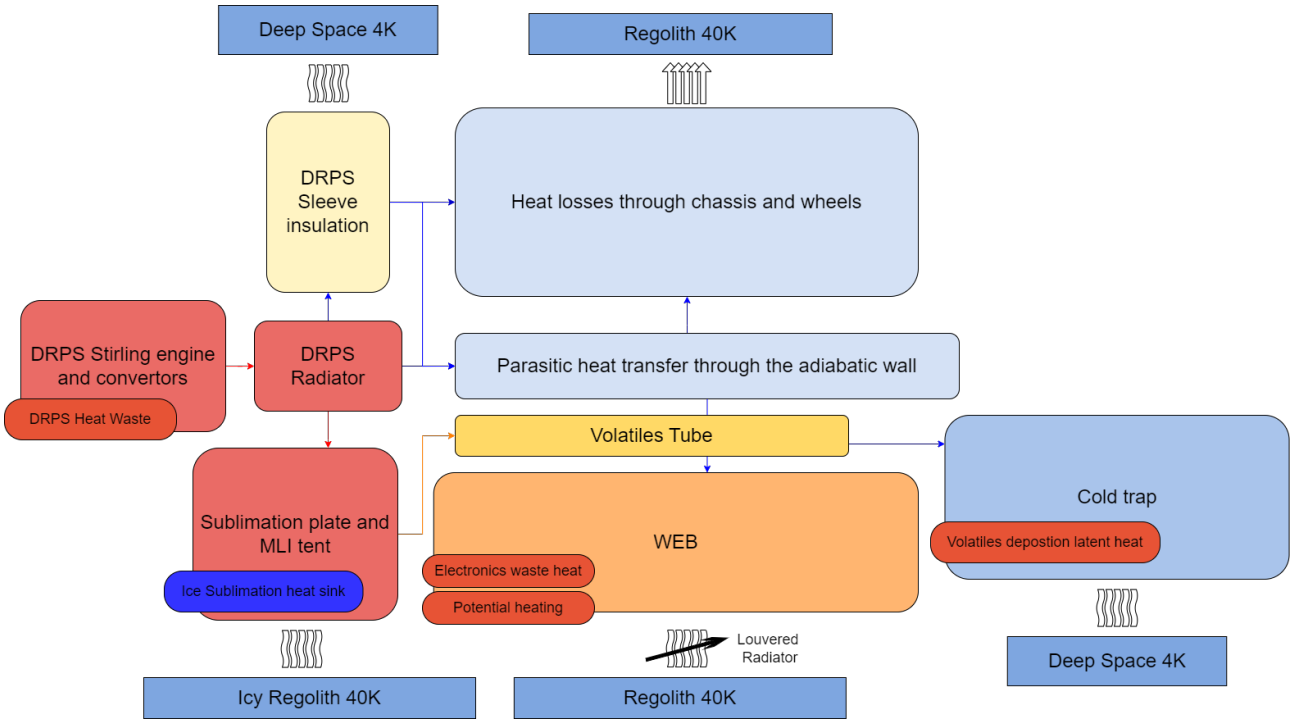

Figure 6.1: A sketch of the Simulink system, with the subsystems, color coded by expected temperature, and their connection to the temperature sources and boundary conditions.

At this point Simulink can solve the physical system network using the Simscape Simulation solver [121]. First of all, the solver will validate the model configuration and check all the data entries. To do so, it will control that all block diagrams are connected to one or more physical networks, and that each network is connected to exactly one solver block. After the model has been validated, the network will be constructed, with all the directly connected ports sharing the same variable along their connection line, which, in this case, is temperature. Later, based on the previous steps, Simscape solver constructs the system of equations for the model. This system will be an algebraic one, as no time derivative of the temperature appears in the equations. Finally, Simscape can solve the network. The simulation is done for steady state, as there are no time dependent inputs, so the solver will solve considering all boundary conditions to be stable for a long enough time to start from and maintain steady state [121].

6.1. Hypothesis and simplifications made to adapt the problem to a 1D network

Simulink is a great tool to explore the behaviour of a new system in order to discover and characterize its governing phenomena, which will drive its design. The Simscape environment allows the designer to rapidly lay out a thermal network comprising of the main elements of a system, to perform a fast and low-cost analysis. Such an analysis is very useful in the first

phases of a project, when many alternatives have to be explored and ruled out, until only the one, or few, which are the most promising, are left. They can be later further characterized both on Simulink and in other ways, such as with a 3D FEM thermal analysis.

Unlike a Finite Element Method simulation, Simulink can only work with one dimension. This obliges the designer to simplify complex geometries, such as entire portion of the rovers, to a slab shaped body, in order to be able to employ the conductive heat transfer block, for example. This one is the first simplification to be made in order to perform the Simulink analysis. Rover elements have been reconducted to basic geometrical shapes, such as parallelepipeds and cylinders, so to be able to easily declare elements length or thickness and cross sectional areas.

Deriving from the previous simplification, large surfaces radiating to the deep space, such as in the case of the insulated rover shell or adiabatic walls, or receiving radiation from another body, as in the case of the regolith being irradiated by the sublimation plate, are considered at a uniform temperature. This can be a problem when a large surface is subjected both to radiative and conductive heat transfer at the same time. In this case, Simulink cannot accommodate for the change in temperature along the surface. The aforementioned limitation is particularly deleterious in the simulation of the regolith heat transfer, where a large amount of regolith is conducting to the nearby regolith and radiating to deep space at the same time.

As for the regolith, which is the greatest obstacle to the accuracy of the ice-mining Lunar rover model, it has been decided to set the regolith temperature as a boundary condition at 40 K. This is not optimal, but can give an initial estimate about the behaviour of the system, from which important parameters, such as the sublimation plate size, can be derived. These parameters will be the inputs of the first iteration of the FEM thermal analysis performed on Siemens NX, which will take into account the 3D effects that the Simulink cannot consider.

6.2. The 1D DRPS model implemented in SIMULINK

The first subsystem to be implemented is the heat source: the DRPS. The Simulink subsystem representing the DRPS leverages from the work previously conducted at the University of Leicester for the characterization of an Am-241 heat source into electrical energy via the Sunpower Radioisotope Stirling Convertor [122]. Figure 6.2 shows the thermal network representing the European Stirling Radioisotope Generator (ESRG) inner workings, exemplifying the flow of the heat from the Am-241 European Large Heat Source (ELHS) through the ESRG Stirling convertor to the radiator. Losses are accounted for as parallel between the leakages through the solid insulation and the ELHS supporting structure, which both bypass the Stirling convertor assembly. Finally, heat leakages and Stirling heat waste meet on the radiator, which radiates to the external environment.

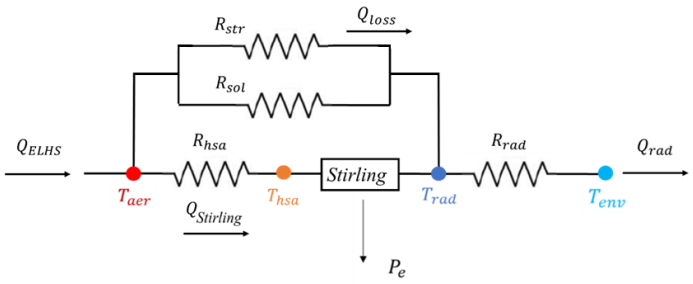

Figure 6.2: The 1D ELHS-ESRG thermal network [122].

The need for a simulation of the Stirling conversion stems from the fact that, being a thermodynamical cycle, its efficiency its influenced by the difference between the hot and cold ends temperatures of the convertor. The DRPS, due to the ice-mining Lunar rover TMS requirements, will work outside of its nominal operational range, as its waste heat will not be radiated away to deep space, as originally designed. The DRPS radiator temperature will be a few degrees higher than the sublimation plate, which in turn must be maintained at at least 100°C during extraction. This will be reflected on the efficiency of the Stirling convertor, which is greatly influenced by the convertor cold end temperature, according to the following relationship:

$$\eta_{Stirling} = \eta_{Carnot} \cdot FoC; \qquad \eta_{Carnot} = 1 - \frac{1}{T_H/T_C} \tag{6.6}$$

where η_{Carnot} is the maximum theoretical efficiency of a the Carnot thermodynamical cycle. η_{Carnot} depends only on the engine hot and cold ends temperatures, T_H and T_C. The higher the ration between these two values, the higher the Carnot efficiency. FoC, or Fraction of Carnot, is the ratio between the efficiency of the Stirling cycle and the efficiency of the Carnot cycle, which provides an upper limit to the efficiency of any thermodynamic engine. The FoC is 0.48 for the Stirling cycle. Finally, the overall efficiency of the DRPS, η_{DRPS}, can be calculated multiplying $\eta_{Stirling}$ by the alternator efficiency, $\eta_{alternator}$, baselined as 0.9:

$$\eta_{DRPS} = \eta_{Stirling} \cdot \eta_{alternator} \tag{6.7}$$

Subsequently, the electric power output P_e can be calculated multiplying the heat collected by the Stirling hot head by the overall efficiency of the DRPS:

$$P_e = \eta_{DRPS} \cdot Q_{Stirling} \tag{6.8}$$

The waste heat (Q_{rad}), on the other hand, is composed of the remaining fraction of the Stirling convertor incoming heat flux, plus the heat losses which bypassed it, Q_{loss} and the heat dissipated by the alternator $Q_{alternator}$:

$$Q_{rad} = (1 - \eta_{DRPS}) \cdot Q_{Stirling} + Q_{loss} + Q_{alternator} \tag{6.9}$$

The waste heat will be rejected by the DRPS radiator and directed to the sublimation plate by a high conductance path constituted of heat pipes. The TMS will also draw some heat from the DRPS, in order to heat up other parts of the rover, such as the volatiles tube, or the WEB.

The latter could in fact be maintained at warm temperatures through trough a conductive path linking the DRPS and the WEB inside, even though this task is left to future design efforts. In fact, this Simulink subsystem will be connected to the other subsystems, as shown in Figure 6.1 and will be the source of thermal power for the ice-mining operations.

6.3. Implementation on SIMULINK of the rest of the rover elements

After the detailed model of the DRPS subsystem have been presented, the implementation of the rest of the rover subsystems will be introduced. The macro areas considered for the thermal analysis are the following: sublimation plate and MLI tent, volatiles tube, cold trap, WEB and the rover insulating and supporting structures, to account for losses. The rover thermal performances will be analysed during extraction phase, even though both a cold and hot scenario will be investigated for the WEB.

6.3.1. Sublimation plate and MLI tent

The first macro area to be presented is an integral part of the TMS. The sublimation plate and MLI tent have been conceptually lumped together in the same subsystem as they are expected to be at a high temperature during the extraction phase, Figure 6.3 shows the layout of their thermal network.

The DRPS radiator node, through which flows DRPS waste heat from the 1D DRPS model based on the ESRG, loses heat to parasitic heat transfer pathways through the adiabatic walls, the insulating sleeve and the rover chassis. The majority of it, anyway, is directed to the sublimation plate by a parallel of two conductive blocks and a radiative one. The latter is the result of the radiation between the lower part of the rover horizontal adiabatic wall. In this case, the heat must first pass through the adiabatic wall, so the amount of heat exchanged this way is negligible. The former two conductive paths are

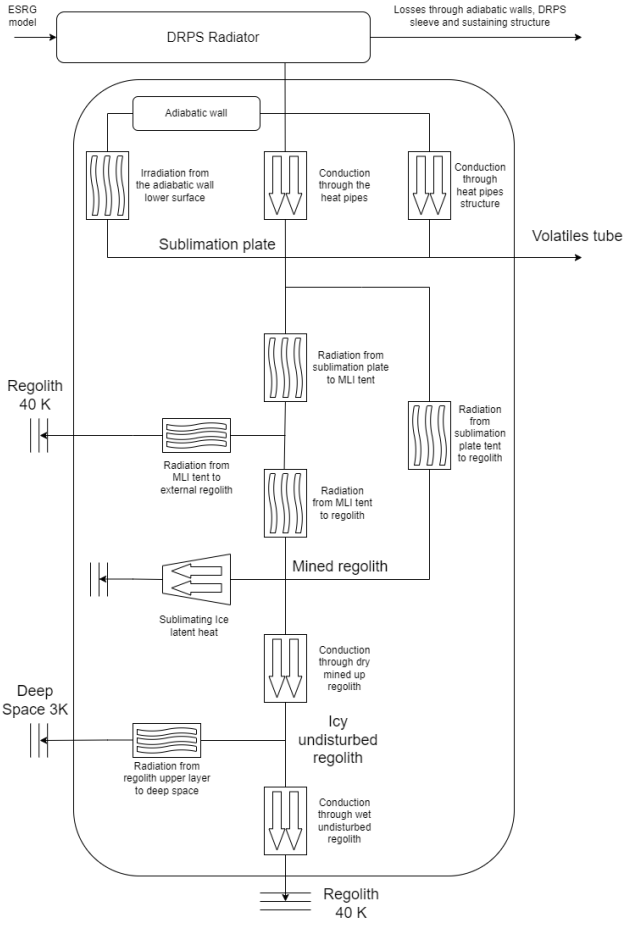

Figure 6.3: Plate and tent thermal network.

the intended ones to draw heat from the DRPS radiator to the sublimation plate: one represents the heat pipes, and the other the heat pipes aluminum supporting structure. Once the sublimation plate node has been reached, some heat is lost to heat up the volatiles tube. The rest is radiated downwards: a fraction of it directly to the regolith, while the rest of the radiation encounters the MLI surface of the tent. The MLI surface consists of a node, which can either lose heat by radiating it to the surrounding regolith on the outer side, or can radiate it inwards on the regolith where ice is being extracted.

Finally, the penultimate node, representing the dried up mined regolith, is connected to a heat sink, standing for the power absorbed by the sublimating ice latent heat. Then, heat is conducted until the boundary condition representing the undisturbed Lunar soil is reached. Alternatively, part of such heat can be radiated to deep space through the Lunar surface.

The limitations of the 1D model, as introduced in section 6.1, constrain the accuracy of this part of the simulation, as it is nearly impossible to model on Simulink the parallel between heat conduction and radiation happening within the regolith. First, heat will be conducted trough a layer of dry regolith deep 0.5 m. This is to represent the extraction phase in its middle. Then the last node, representing icy undisturbed regolith, is reached. Radiation to deep space from this node will be accounted for by considering an area roughly one order of magnitude larger the mined area, representing the regolith surrounding it. Heat can also be conducted trough 1 m of regolith across a section 10 times larger than the sublimation plate area. This has been done to account for the gradual increase in size of the regolith volume while distancing from the area where extraction is conducted. Both radiation and conduction in from the last node have been heavily simplified to fit the 1D nature of the model, so results may need to be refined through the NX 3D analysis.

6.3.2. Volatiles tube

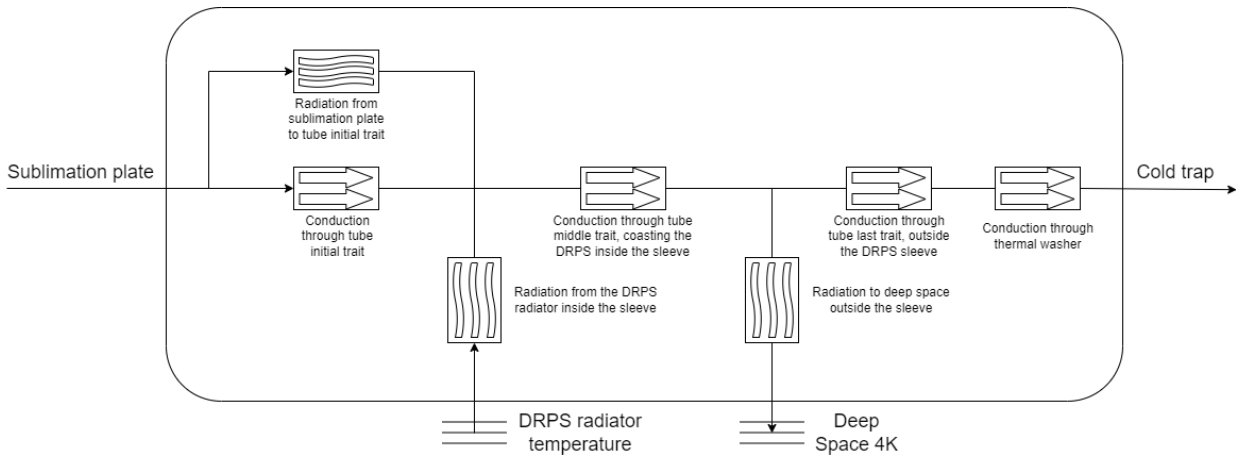

Figure 6.4: The volatiles tube thermal network.

The volatiles tube, also implemented as another subsystem, is shown in Figure 6.4. The initial part of the tube is directly connected to the sublimation plate node, drawing heat from it. A short first portion of the tube also receives heat from the sublimation plate through irradiation. Subsequently, the volatiles tube is exposed to the DRPS radiator while it coasts the DRPS inside the insulating sleeve: this portion of the tube will receive heat radiated from the DRPS radiator. Finally, the terminal part of the tube, exposed to the adiabatic wall and the external environment, will see the deep space for a very short section. The tube will then enter a thermal washer interface with the cold trap, designed to limit heat transfer across the tube.

6.3.3. Cold trap

The cold trap is the last element properly belonging to the TMS. Its thermal network can be seen reported in Figure 6.5. The cold trap must be kept at the lowest temperature possible, to do so, heat spillages must be avoided at all costs. Hence, the cold trap is equipped with thick solid insulating layers which obstruct the parasitic heat flows coming from warmer elements located near it, such as the WEB. Some heat may also leak from the DRPS through the adiabatic walls and the rover chassis. Another source of heat is the volatiles tube, insulated by a thermal washer, as exemplified in the previous subsection.

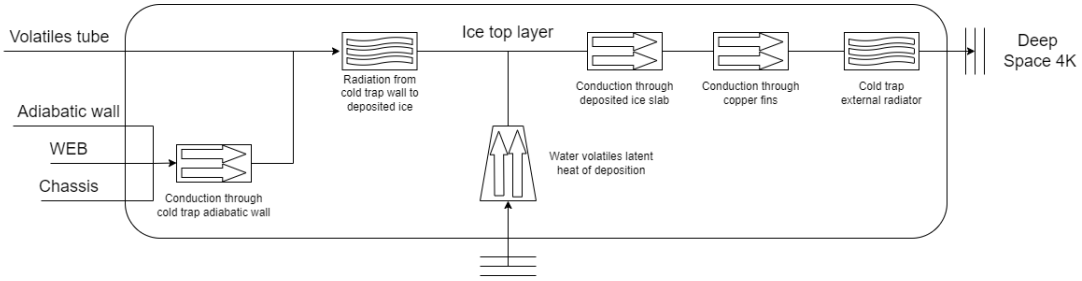

Figure 6.5: The cold trap thermal network.

Subsequently, heat spillages will be radiated from the cold trap walls to the top layer of ice depositing on the finned surface. To represent the ice mining situation in the broadest and most general way, the deposition process is simulated while ongoing, so that a layer of ice is already present around the cold trap fins. This ice acts as a mildly effective insulator, slightly degrading the cold trap performances with respect to the start of the extraction phase. On the node representing the top ice layer is also applied a heat flux representing the water volatiles latent heat of deposition, equal in amount to the heat subtracted from the regolith in the sublimation plate and MLI tent of subsection 6.3.1.

Deposition latent heat is conducted through the previously deposited ice layer to reach the fins. The fin spacing was an integral part of the cold trap sizing process, and has been derived on MATLAB/Simulink with a tradeoff between the number of fins and the amount of insulation provided by the ice layer. The less the fins, the more the space for the ice in the cold trap, but

also the higher the insulative effect of the ice towards the end of the extraction phase, due to its higher thickness. For the cold trap to function as intended, all the deposition latent heat must be rejected to deep space. This means that heat must be conducted through the ice first, and by the copper fin through its section to the radiator, later. The phenomenon is governed, on a first order of approximation, by two relationships, defining two thicknesses, a thermal and a geometrical one:

$$t_{thermal} = k_{ice} \cdot \Delta T \cdot A / \dot{Q}_{ice} \tag{6.10}$$

$$t_{geometrical} = \frac{l - N_{fins} t_{fin}}{2N_{fins} + 2} \tag{6.11}$$

The first thickness, $t_{thermal}$, indicates the maximum thickness after which the insulating effect of ice renders impossible the conductance of all the deposition latent heat $\dot{Q}_{ice}$, taken from the results of Table 5.2. A, the deposition area, depends on the number of fins: the more the fins the larger the area. ΔT is the temperature difference between the top layer of the ice slab, and the lowest one, in contact with the fin. It has been considered as 5 K. The second equation describes the semi-distance between two fins, which would be the maximum geometric thickness of the ice slab depositing on a single fin surface. It depends only on geometrical parameters: l is the cold trap inner width, equal to 84 cm, N_{fins} is the number of fins, and t_{fin} is the thickness of a fin, selected as 2 cm.

The two thicknesses, depending only on the number of fins, have been calculated for various cold trap configurations to see where the two values were closer, so that ice capacity is maximized, while the cold trap performances are not jeopardized. The fin number to achieve the closest value between $t_{thermal}$ and $t_{geometrical}$ have been found to be slightly below 5 in case of regolith with 5% ice vol. and slightly over 5 in case of 10% ice vol. regolith. Hence, a 5 fins configuration have been adopted for the cold trap. Considering a deposited ice slab thickness of 5 cm, representing the ice already deposited on the cold trap, a volume of 55 litres is occupied by the ice, corresponding to a mass of water of around 50 kg. This value can be taken as a baseline for a reasonably full cold trap, and it represent the amount of ice present in the cold trap during the thermal analysis. It is only a lower limit on the capacity of the cold trap, as if its inner temperature is still low enough, additional ice can still be deposited.

Finally, heat is conducted through the the copper fins and directed to the cold trap radiator, which, to increase the heat rejection performances, has been extended over all the cold trap surfaces having an unobstructed view to deep space. The large width of the fins increase their conducting section, ensuring that the totality of the heat can be conducted smoothly to the radiator, maintaining a lower ΔT between the former and the latter. This choice has been taken to improve the cold trap performance, by lowering the minimum temperature achievable, which has been very useful in the 10% ice vol. case to reach deposition temperature.

6.3.4. WEB

The WEB thermal network, illustrated in Figure 6.6, presents incoming and outcoming heat flows, together with the heat sources deriving from the electric power dissipation of the WEB instrumentation. The node called WEB electronics, represents the area inside the WEB, sees the inflow from DRPS radiator heat leaks and has different heat dissipation terms applied according to the situation. The first term, always present, represents the DRPS Power Control and Distribution Unit (PDCU) waste heat, baselined as 10 W. The second heat source is the electric power dissipation by the rest of the rover electronics. It depends on the power mode.

A hot and cold case scenario has been identified, the former when roving, the latter when the rover is in stand-by, or extracting ice. The amount of heat dissipation is still uncertain: it has been taken from the prospective power budget of Table 4.1. For the cold case, a heat dissipation ranging from 2 W to 20 W is to be considered, while for the hot case the amount of heat waste will oscillate between 25 W and 50 W.

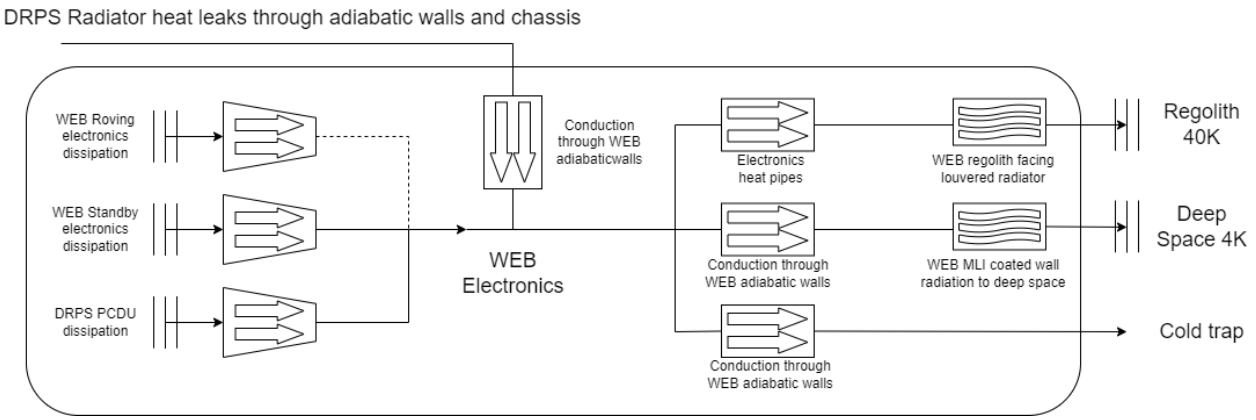

Figure 6.6: The WEB thermal network.

Subsequently, heat will leave the cold trap following three routes. The first two, are unwanted routes, and consist of heat losses through the insulation. One is the heat leak to the cold trap, from the WEB top side, while the other one is the the heat losses to deep space through radiation from the MLI coated adiabatic walls. The last one, is part of the WEB TMS design, and consists of a louvered radiator facing the Lunar soil.

The louvered radiator has been selected as a temperature management technology. It is a virtually passive device. The radiator is connected to the rover on-board computer by electronics heat pipes, and its louvers will be opened during power consumption peaks to dissipate the additional heat, and closed during standby and extraction, to avoid losing excessive amounts of heat. The radiator baselined emissivity is 0.25 when the louvers are closed and 0.7 when they are open. The optimal temperature interval for the WEB is ranges from -10°C to 30°C.

6.3.5. Losses through DRPS sleeve, chassis and wheels

The last macro area of the rover Simulink model is subdivided into three different sections: the DRPS insulating sleeve, the rover adiabatic wall and the rover chassis and wheels, connected to each other as shown in Figure 6.7. They have been lumped together because they all represent a source of loss by the TMS perspective, in fact they are characterized by thick refractory foam insulation based on the Rohacell baseline. Radiative losses are also kept in check by use of MLI, especially on large surfaces seeing deep space, as in the case of the DRPS sleeve.

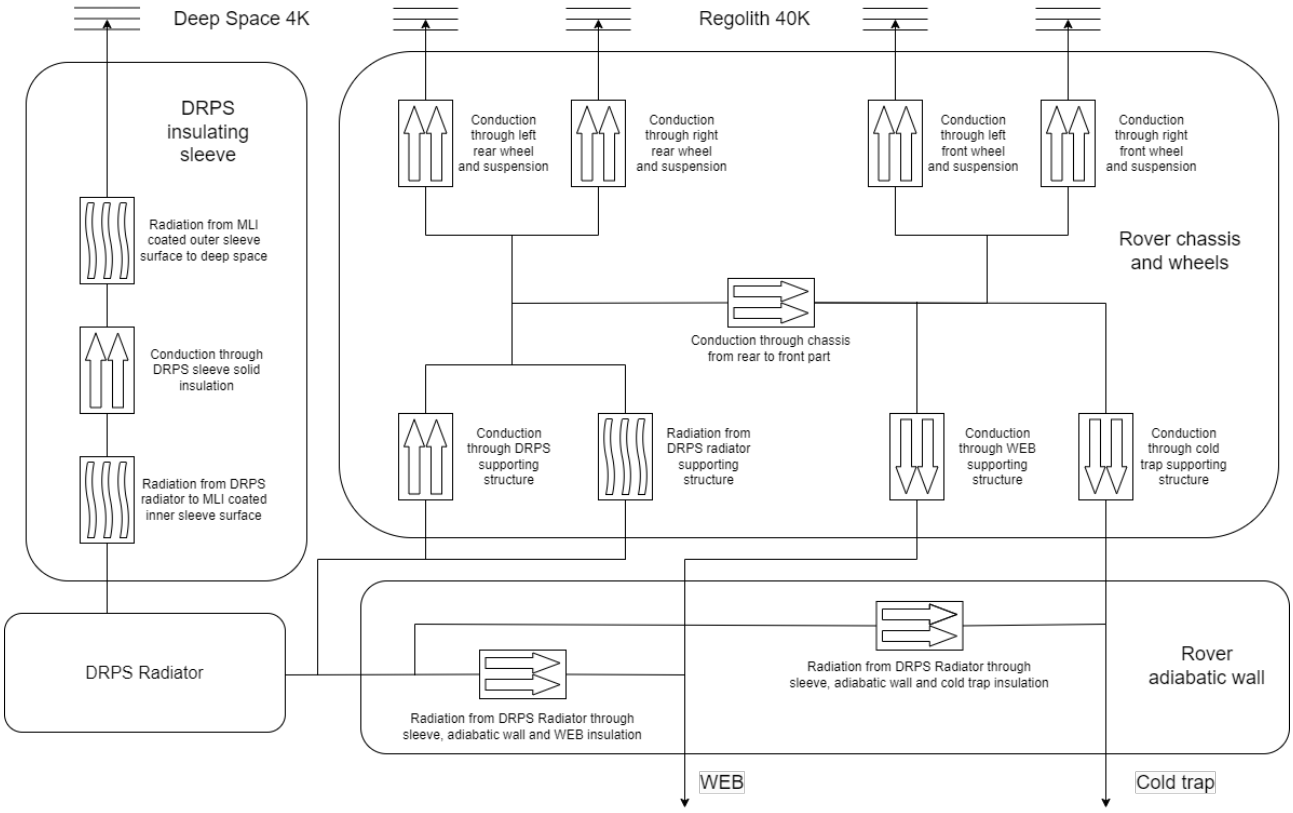

Figure 6.7: The thermal network representing the losses through DRPS sleeve, adiabatic wall, sustaining structure, chassis and wheels to the surrounding environment.

The DRPS insulating sleeve, which shields the DRPS radiator from the view of deep space, is coated internally and externally with MLI, to minimize as much as possible radiative heat losses. The sleeve itself is made of refractory foam, to increase insulation capabilities. The rover adiabatic wall contains two conductive blocks, exemplifying the radiative and conductive losses from the DRPS radiator through the adiabatic wall, to the WEB and the cold trap.

The rover chassis and wheels, and their supporting structure, have been implemented in the third and last subsystem. First, heat will flow from the DRPS sustaining structure to the chassis, which is connected to the locomotion system rear couple of suspensions and wheels.

From there, heat can be conducted to the cryogenic PSR regolith. The heat lost this way can be a high fraction of the rover thermal budget, if precautions are not employed. To minimize it, wheels have been equipped with grousers, which, apart from increasing traction, also minimize the contact area with the ground, reducing the cross sectional area for thermal conductivity. Furthermore, the whole chassis is realised in a low conductivity material, which can either be titanium alloy or composite material, and the chassis interface with the hot DRPS radiator presents a thermal washer interface to control heat spillage. The front wheels couple node is connected to the rear one by a conductive block representing the chassis length between the two. From there, heat can be lost to the PSR environment by conduction through the front wheels, or it can leak inside the WEB and the cold trap through their supporting structures.

6.4. Results presentation and discussion

This section will present the results of the Simulink thermal analysis. Table 6.1 to Table 6.4 report the temperature of every node of the thermal network, as presented in section 6.2 and section 6.3. The first table will report the results for the rover irradiating dry regolith through the sublimation plate. The others will present the network temperatures for ice-mining over 1%, 5% and 10% ice vol. regolith. Heat losses and flows to the environment and across nodes, together with heat loads, sinks and efficiencies, have also been added to the tables.

Node		T_{node}	Additional remarks
DRPS Radiator		330°C	P_{th} = 338 W; η_{DRPS} = 16.4%; P_e = 62.5 W
Sublimation plate		329°C	P_{mining} = 293 W; η_{TMS} = 86.7%
Volatiles tube	at plate	300°C	Heat loss from plate: 13 W Heat radiated by DRPS: 9 W
	coasting DRPS	195°C	
	to cold trap	182°C	
MLI tent		208°C	Heat loss to environment: 268 W
Mined regolith		296°C	Sublimation latent heat sink: 0 W
Undirsturbed icy regolith		-156°C	Heat flow through regolith: 23 W Heat radiated to deep space: 2 W
Cold trap ice		-223°C	Deposition latent heat flow: 0 W
Cold trap radiator		-223°C	Total rejected heat ≅ 0 W
WEB	Extraction	13°C	Cold case internal dissipation: 20 W
	Roving	15°C	Hot case internal dissipation: 50 W
DRPS sleeve		-269°C	Heat loss to deep space ≅ 0 W
Chassis	Rear	9°C	Rear wheels heat loss: 21 W
	Front	-59°C	Front wheels heat loss: 15 W

Table 6.1: Dry regolith Simulink thermal analysis results.

Node		T_{node}	Additional remarks
DRPS Radiator		329°C	P_{th} = 337 W; η_{DRPS} = 16.5%; P_e = 62.7 W
Sublimation plate		327°C	P_{mining} = 293 W; η_{TMS} = 86.9%
Volatiles tube	at plate	298°C	Heat loss from plate: 13 W Heat radiated by DRPS: 9 W
	coasting DRPS	195°C	
	to cold trap	181°C	
MLI tent		207°C	Heat loss to environment: 265 W
Mined regolith		294°C	Sublimation latent heat sink: 3 W
Undirsturbed icy regolith		-163°C	Heat flow through regolith: 8 W Heat radiated to deep space: 18 W
Cold trap ice		-185°C	Deposition latent heat flow: 3 W
Cold trap radiator		-185°C	Total rejected heat: 3 W
WEB	Extraction	13°C	Cold case internal dissipation: 20 W
	Roving	15°C	Hot case internal dissipation: 50 W
DRPS sleeve		-269°C	Heat loss to deep space ≅ 0 W
Chassis	Rear	7°C	Rear wheels heat loss: 21 W
	Front	-60°C	Front wheels heat loss: 15 W

Table 6.2: 1% ice vol. regolith Simulink thermal analysis results.

Node		T_{node}	Additional remarks
DRPS Radiator		255°C	P_{th} = 326 W; η_{DRPS} = 19.8%; P_e = 74.1 W
Sublimation plate		253°C	P_{mining} = 296 W; η_{TMS} = 90.8%
Volatiles tube	at plate	229°C	Heat loss from plate: 11 W Heat radiated by DRPS: 5 W
	coasting DRPS	151°C	
	to cold trap	135°C	
MLI tent		130°C	Heat loss to environment: 131 W
Mined regolith		171°C	Sublimation latent heat sink: 144 W
Undirsturbed icy regolith		-194°C	Heat flow through regolith: 16 W Heat radiated to deep space: 5 W
Cold trap ice		-40°C	Deposition latent heat flow: 144 W
Cold trap radiator		-43°C	Total rejected heat: 144 W
WEB	Extraction	8°C	Cold case internal dissipation: 20 W
	Roving	13°C	Hot case internal dissipation: 50 W
DRPS sleeve		-269°C	Heat loss to deep space ≅ 0 W
Chassis	Rear	-72°C	Rear wheels heat loss: 14 W
	Front	-94°C	Front wheels heat loss: 12 W

Table 6.3: 5% ice vol. regolith Simulink thermal analysis results.

Node		T_{node}	Additional remarks
DRPS Radiator		209°C	P_{th} = 319 W; η_{DRPS} = 21.8%; P_e = 80.7 W
Sublimation plate		208°C	P_{mining} = 296 W; η_{TMS} = 92.8%
Volatiles tube	at plate	186°C	Heat loss from plate: 9 W Heat radiated by DRPS: 4 W
	coasting DRPS	122°C	
	to cold trap	106°C	
MLI tent		74°C	Heat loss to environment: 73 W
Mined regolith		49°C	Sublimation latent heat sink: 208 W
Undirsturbed icy regolith		-216°C	Heat flow through regolith: 14 W Heat radiated to deep space: 1 W
Cold trap ice		-16°C	Deposition latent heat flow: 208 W
Cold trap radiator		-21°C	Total rejected heat: 208 W
WEB	Extraction	6°C	Cold case internal dissipation: 20 W
	Roving	12°C	Hot case internal dissipation: 50 W
DRPS sleeve		-269°C	Heat loss to deep space ≅ 0 W
Chassis	Rear	-109°C	Rear wheels heat loss: 11 W
	Front	-112°C	Front wheels heat loss: 11 W

Table 6.4: 10% ice vol. regolith Simulink thermal analysis results.

The first node listed in the tables is the DRPS radiator. Its temperature is presented, along with the total waste heat, the DRPS electric power output according to the 1D model and its overall conversion efficiency. The total DRPS waste heat, which is available for mining, slightly decreases when ice vol. content grows. This is due to the fact that dry regolith is much more insulating than wet regolith, but most importantly, from the fact that extraction in higher ice vol. content terrains entails that a sizeable amount of the waste heat is absorbed by the ice sublimation latent heat, which acts as heat sink, contributing to a decrease in the sublimation plate and DRPS radiator temperature of more than 100°C between the dry and the 10% ice vol. regolith cases. A higher DRPS radiator temperature reverberates on the DRPS efficiency, as shown by Equation 6.6, causing the electric power output to decrease. In fact, according to the model result, only in the 10% ice vol. regolith mining case, the radiator temperature would be low enough to allow for a total conversion efficiency over 20%. This underlines a serious problem which warrants additional investigations, because, even if the DRPS power output is still higher than the rover power budget, this might negatively influence its autonomy.

The sublimation plate presents a temperature just one or two degrees centigrade lower than the DRPS radiator node: it is an effect of the high conductivity connection established by the heat pipes between the two elements. In all the investigated cases, the plate temperature is abundantly over the 100°C requirement. This aspect will be clarified by the NX 3D thermal

analysis. The higher temperatures resulting from the Simulink model are likely caused by the propensity for heat retainment of 1D models, where it is difficult to account for all the possible heat loss contributions. For this reason, the sublimation plate design has been also iterated with NX, in order to perform a 3D analysis. Depending from the NX results analysis, the sublimation plate might be enlarged, or its dimensions could be confirmed. The heat radiated from the sublimation plate downwards to the regolith is employed to calculate the TMS efficiency, which is very high (over 85%) for all the four cases. This is also probably a derivation from the 1D model difficulty to account for heat losses, and will be further investigated with a 3D simulation.

The volatiles tube, which temperature has been measured in three different locations along its length, can be successfully maintained at a temperature high enough to avoid ice deposition on its inner surface. The heat is subtracted from the sublimation plate mainly through conductivity, but also absorption from the DRPS radiator, while the tube coasts it inside the insulating sleeve, is relevant. In all instances, both sources provide less than 25 W, decreasing down to 15 W when the sublimation plate is colder, in the scenarios with higher ice contents.

The MLI tent temperature, as well as the heat loss through radiation to the outside regolith, decreases with the increase of the ice volumetric content in the Lunar terrain. This is due to the fact that in icy regolith, more heat is removed through the sink mechanism representing sublimation latent heat. The mined regolith node follows the same pattern, and it is always at a higher temperature than the MLI tent. This temperature difference is much more pronounced at lower ice vol. contents, where the MLI tent becomes one of the largest heat rejecting elements, due to the low conductivity of dry regolith. Both the mined regolith and the undisturbed icy regolith nodes decrease in temperature with the increase of ice content, even though the patch of regolith directly under the sublimation plate is always at a higher temperature than the ice sublimation point. It is also interesting to see that, as a greater regolith ice content means higher conductivity for the undisturbed icy regolith, the balance between radiation and conductivity heat transfer from the last node to the environmental boundary condition nodes is in favour of conductivity for icy regolith. Conversely, the equilibrium is shifted in favour of radiation in the cases of dry and 1% ice vol. regolith.

On the other extremity of the TMS, the cold trap can always be maintained at low temperatures, with very limited heat leaks from the TMS high temperature segment. Heat spillage is so low, that, in all the investigated scenarios, the deposition latent heat flow is equal to the amount of heat rejected by the cold trap radiator. This result would mean virtually perfect insulation, which is very difficult to be achieved. Hence, the results of the 3D FEM analysis will need to characterize the cold trap with more detail than it has been done now. In any case, on 3 out of 4 cases, the cold trap temperature is low enough to guarantee ice deposition on the finned surface. In the 10% ice vol. regolith case, the temperature on the top layer of the cold trap is

just -16°C, indicating that the cold trap might face difficulties while processing higher volatiles mass flow rates, at least towards the end of the mining process, and that the radiator area could be enlarged to be able to dissipate enough heat.

The WEB node, conversely, presents a very high temperature stability across all the four scenarios. The cold case scenario considers a dissipation of 20 W, and it presents temperatures ranging from 13°C to 6°C. The hot one, with a total internal heat dissipation accounted for 50 W, achieves temperatures slightly higher, ranging from 12°C to 15°C. In any case, the maximum change in temperature among the four scenarios is 6°C, which is a very good result.

Considering the losses, three nodes have been investigated. The DRPS sleeve external temperature is practically the same as deep space, and the total losses through the sleeve are negligible. This result is very unlikely to be representative of the real outcome, so a closer investigation over the sleeve heat loss dynamics is necessary, and will be conducted on NX.

Finally, losses to the Lunar terrain through chassis and wheels have been analysed. Two nodes, representing the front and rear portion of the rover chassis have been laid out in the thermal network. The rear chassis temperature is always higher than the front one, sometimes marginally, as in the case of high ice content regolith, sometimes sizeably, as in the dry regolith case, where there is a difference of 60°C between each other's temperatures. This is due to the fact that the rear part of the chassis is closer to the DRPS waste heat source than the front. Furthermore, the temperature of both nodes increases as the regolith gets dryer, since the DRPS waste heat, which is not being absorbed by the sublimating ice, must find other paths to be rejected to the environment. This will be of use while roving on dry regolith outside of ice deposits, as a higher temperature on the locomotion system will favour the actuation of its driving motors. The heat lost to the Lunar soil through the wheels is in any case limited, it amounts to generally less than 20 W per couple of wheels in the drier regolith cases, and is reduced down to 11 W per wheel couple in the 10% ice vol. scenario. For the aforementioned reason, and since a correct thermal representation of the rover locomotion system would be very difficult and time consuming, wheels and suspensions have not been included in the FEM based 3D thermal analysis.

In conclusion, as 1D analysis are limited into accounting for heat loss mechanisms and usually favour heat retainment, a more complete 3D simulation is needed. The NX FEM thermal analysis will in fact report lower temperatures, with the same applied heat loads.

Another important consideration is the fact that the investigated situations represent final steady states. They will constitute a lower limit on the TMS performances, rather than a baseline characterizing its nominal behaviour, especially for the dry and 1% ice vol. content regolith. In fact, the results of the two aforementioned cases, reported in Table 6.1 and Table 6.2,

would only be achieved only after long stationary periods on terrains poor in ice content. In reality, this would not happen, as there would not be any particular reason to have the rover unproductively station for long time over patches of dry regolith. Hence, a situation similar to the one outlined in the first two scenarios would virtually never happen. If the rover were to be roving over dry regolith PSR areas, the sublimation plate would see a new influx of undisturbed regolith, which would act as a cryogenic temperature heat sink, absorbing the DRPS waste heat and contributing to a decrease of its temperature.

The Simulink analysis results about the final DRPS radiator temperature, if confirmed by the NX 3D thermal analysis, might after all indicate the need for a second heat transfer pathway. A louvered radiator on top of the sleeve could be an effective solution as it is a passive technology able to control in a continuous manner the radiator emissivity by changing the angle of its louvers. This solution, paired with a thermostat based temperature controller system, could adapt the heat transferred to the sublimation plate to the amount of ice contained in the regolith, avoiding the high temperatures seen in the results of the drier regolith scenarios.

Finally, these results show that ice mining operations can, within a certain range of efficiencies, be carried out over regolith containing up to 10% in ice vol. The best performances would be obtained at regolith ice contents near to 5%.

7 | The rover NX 3D thermal analysis

This chapter will introduce the rover 3D model employed in the FEM thermal analysis, developed on the Siemens NX CAD. As for the Simulink 1D thermal network presented in the previous chapter, only the final model and the results of its thermal analysis will be presented. The Siemens NX CAD allowed for the design of the rover, as detailed in chapter 4. Subsequently, the software also permits the designer to analyse the rover thermal behaviour through a 3D Finite Element Method (FEM) based thermal analysis. The model heat loads and environmental boundary conditions have been presented in chapter 5.

FEM is a numerical technique to solve differential equations arising from the modeling of a variety of physical phenomena characterising a wide array of engineering problems, among which lies thermal analysis. In order to solve the set of differential equations describing the problem, the technique discretises a large body subdividing it between many smaller fractions, called finite elements. Finite elements are multidimensional geometrical bodies, whose vertexes are identified by nodes. The nodes are connected together describing a mesh, which also defines the elements shape. To each mesh are associated some material properties. In the case of the presented analysis, which refers to steady state, the only material properties required are thermal conductivity and infrared emissivity. They are reported in Appendix A.

The meshes are created by Siemens NX once the relevant bodies or surfaces have been identified. The finite elements contributing to a mesh can be of different shapes, for the meshes employed in the ice-mining Lunar rover thermal analysis simple tetrahedral elements for 3D body meshes and triangular elements for 2D surface meshes have been employed. At this point, once the mesh have been established, it is possible to discretise the continuous partial differential equations problem into a system of algebraic equations, which can be solved by numerical methods.

Meshes are saved in the FEM file which is connected to the CAD and the simulation files. The simulation file allows the designer to declare boundary conditions, heat loads and thermal connections between the meshes. Conductive couplings can be established by declaring surfaces belonging to different meshes which are in touch with each other. Alternatively, meshes can

be united in FEM file with the "unite mesh" command. This will avoid the need for declaring physical connections later. Radiative couplings can be established with two commands: "enclosure radiation" and "all radiation". The first command allows to consider only certain surfaces, which must be selected one by one by the designer. View factors between communicating surfaces will be calculated for each enclosure. The second one instead directly considers the view factor of each element with the others and the environment. This second method of accounting for radiation requires longer simulation time in order to calculate the required view factors, but accounts for all the CAD model geometries, and is the one which have been employed.

7.1. The final model for the NX 3D thermal analysis

As outlined in the previous chapters, only the most representative components of the ice-mining Lunar rover thermal behaviour have been simulated in the NX 3D analysis. The results of the Simulink model presented in chapter 6 indicated that there was not a pressing need to include the wheels and the rest of the locomotion system, as losses from them have been found to be minor. The WEB has also not been included. This choice was due to the preference to simulate only components which are parts of the TMS, as the cold trap, the volatiles tube, the sublimation plate and the cold trap; or that are intimately connected with it, such as the MLI tent, the regolith and the adiabatic wall. Figure 7.1 shows the rover components included in the simulation, while Figure 7.2 illustrates a section view of them.

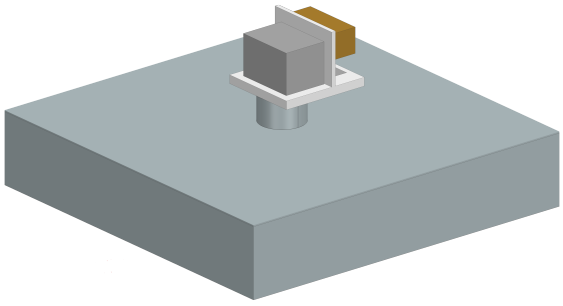

Figure 7.1: The CAD model of the ice-mining Lunar rover components simulated in the FEM thermal analysis.

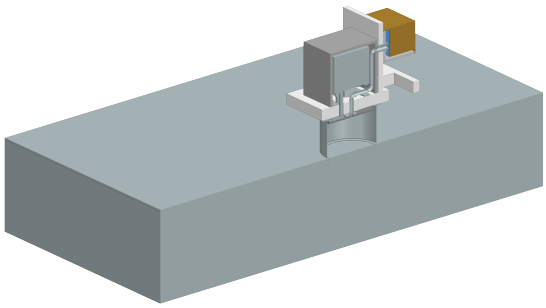

Figure 7.2: A section of the CAD model of the ice-mining Lunar rover components simulated in the FEM thermal analysis.

An additional provision had to be taken as the absence of the WEB would cause the regolith and the lower part of the adiabatic wall to see the cold trap and exchange heat with it by radiation. This problem has been taken into account and solved by meshing the lower surface of the cold trap separately and unflagging the radiation box, so that no radiative exchanges can be exchanged between the cold trap and the rest of the rover and the environment.

7.2. Results presentation and discussion

The following four couples of figures and tables illustrate the results of the NX 3D finite element based thermal analysis for the four scenarios for which boundary conditions have been derived in chapter 5. Figure 7.3 and Table 7.1 refer to the dry regolith case, while Figure 7.4 to Figure 7.6, as well the accompanying tables, report the analysis results for 1%, 5% and 10% ice vol. content in the regolith, respectively. The tables illustrate the maximum and minimum temperature for the most important rover and rover TMS components.

As it emerges from the comparison of the analysis results for different ice vol. contents, it can be seen that most element temperatures are stable between different scenarios. If fact, the only area of the TMS which sizeably changes temperature from case to case is the low temperature segment, especially the cold trap. This can be seen as a proof of the good decoupling between TMS high and low temperature segments, able to avoid excessive heat spillages even with the presence of a direct physical connection such as the volatiles tube, which is kept at a high enough temperature to avoid ice deposition on its surface, in all four scenarios.

Due to the increased influx of hot water volatiles to be deposited, cold trap deposited ice and cold trap radiator temperatures increase with regolith ice vol. content. In all four cases, a temperature of maximum -20°C is achieved on the cold trap deposited ice top layer, meeting the core requirement delineated in section 2.2. The last case, representing 10% ice vol. content regolith being mined, might indicate a difficulty for the TMS to allow ice deposition while extracting water from high content icy regolith, as cold trap ice temperature ranges from -20°C to -25°C. This is nonetheless result of a conservative analysis, as no volatiles losses were considered and thanks to the fact that already deposited ice already act as an insulator, but also proves that 10% ice vol. content is the richest ice deposit that the ice-mining Lunar rover can handle under the current configuration. A simple improvement, if needed, would be the increase of the cold trap radiator area. To do this without revolutionizing the rover size, deployable radiator panels could be fitted on the sides of the cold trap, increasing heat rejection capabilities and resulting in lower cold trap temperatures.

The results regarding the TMS low temperature segments elements agree with the Simulink model, as the effective decoupling from the other segment and the rest of the rover simplify its dynamics to be very straightforward. On the other hand, the 3D model is more effective in accounting for losses than the 1D model, and this can be seen in the high temperature segment, where temperatures have been lowered substantially with respect to the Simulink analysis results. This is due to two factors. The first one is the correct portrayal of the DRPS sleeve losses, which now is at much higher temperature and hence it radiates a sizeable amount of heat to deep space. The second one, and also the main responsible of a similar

decrease in temperature for the DRPS, is the much higher amount of heat lost through regolith irradiation to deep space. In fact, the rest of the heat radiated to the regolith by the sublimation plate, which is not absorbed by ice sublimation, is conducted by the regolith towards the area surrounding the rover, or radiated to the regolith fluff by the MLI tent, thanks to its very good view factor with the surrounding environment. This will heat up large areas of regolith fluff to temperatures, which although quite low (decreasing radially from ∼170 K to ∼100 K along a distance of ∼1.5 m from the mining spot), will manage to radiate to deep space tens of Watts, due to the high emissivity of regolith fluff and the large areas considered. This interesting heat loss mechanism, which it was impossible to account for in a 1D analysis, is the main responsible of the temperature decrease of the TMS high temperature segment components across the two simulations.

Nonetheless, the other basic requirement mandating a sublimation plate temperature of at least 100°C has been met with an abundant margin as the temperature is in all scenarios slightly lower than 150°C. Furthermore, the relatively low temperature of the DRPS radiator, from which the sublimation plate draws heat through the heat pipes, goes into the direction of satisfying one of the additional requirements of section 2.3, which lists as a "nice to have" a low temperature for the DRPS radiator, in order to raise RPS electric power output thanks to an increase in its conversion efficiency (Equation 6.6).

Finally, Figure 7.5 and Table 7.3 report the results for the 5% ice vol. content scenario. This is the reference scenario on which the ice-mining Lunar rover concept was focused. Sublimation plate temperature on the radiator side amounts to 147°C, while cold trap deposited ice highest temperature is -40°C allowing deposition for pressures as low as ∼10 Pa (Figure 5.4). The projected steady state pressure for the water volatiles under the MLI tent, and in the cold trap, is 30 Pa (Figure 5.6). Hence, all the core temperature requirements for the nominal working scenario have been met, proving that the ice-mining Lunar rover concept is a feasible one.

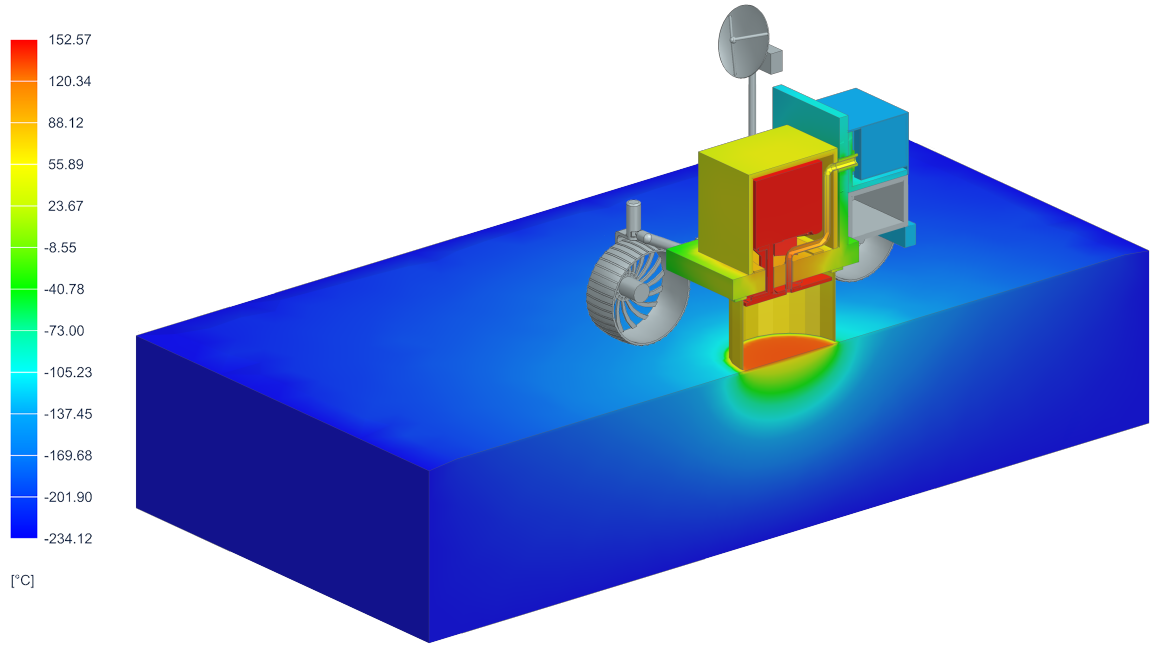

Figure 7.3: Dry regolith Siemens NX FEM thermal analysis results.

Component	Temperature [$°C$]		Component	Temperature [$°C$]	
DRPS radiator	max: 152 (top side) min: 150 (on heat pipes)		Volatiles tube initial trait	max: 145 (on plate) min: 128 (out of AD wall)	
Heat pipes	max: 150 (on DRPS) min: 147 (on plate)		Volatiles tube middle trait	max: 128 (sleeve entrance) min: 48 (out of sleeve)	
Sublimation plate	max: 147 (on heat pipe) min: 145 (on radiator)		Volatiles tube terminal trait	max: 48 (out of sleeve) min: 46 (tube end)	
MLI tent	Int.	min: 53 (AD wall) max: 68 (to regolith)	Cold trap thermal washer	Radially	min: -30 (to AD wall) max: 46 (to tube)
	Ext.	min: 52 (AD wall) max: 67 (to regolith)		Face seeing ice	min: 4 max: 16
Regolith max.	133 (centre of mining area)		Ice	-132	
DRPS structure	max: 150 (to DRPS) min: 82 (on walls)		Cold trap	Fins: -133 Radiator: -134	
DRPS sleeve	Int.	min: 72 (lower angle) max: 86 (top side)	Adiabatic walls	max: 100 (inside sleeve) min: -125 (front of rover) rear min: -55 (AD wall)	
	Ext.	min: 40 (lower angle) max: 54 (top side)			

Table 7.1: Dry regolith Siemens NX FEM thermal analysis results.

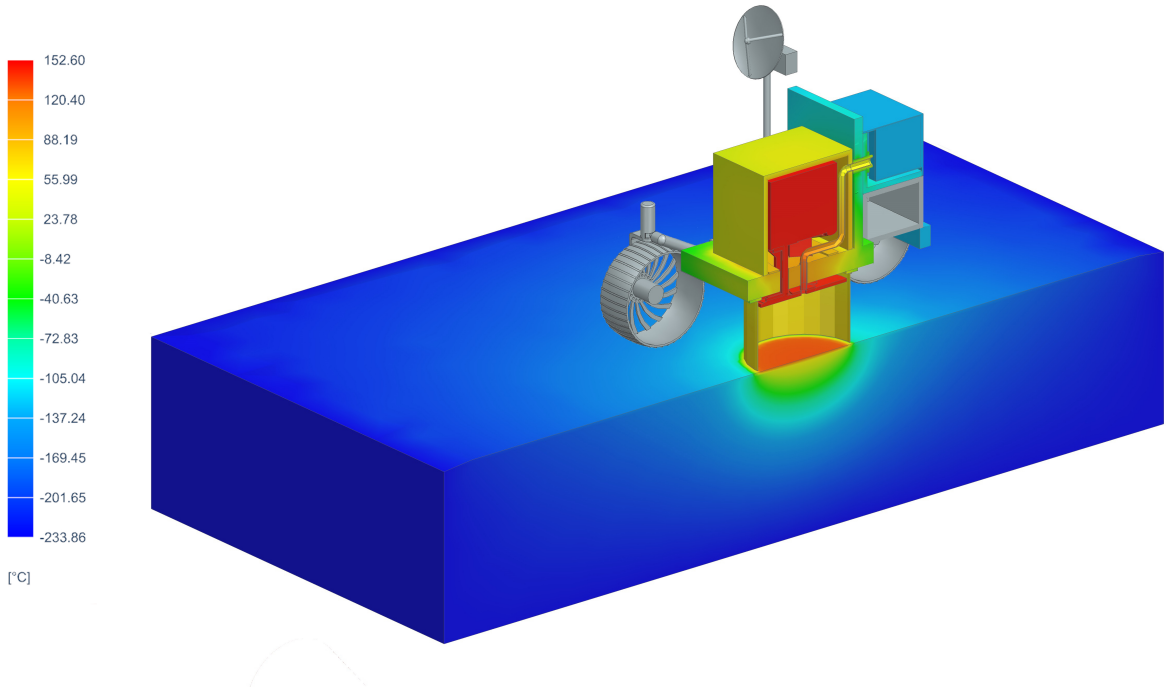

Figure 7.4: 1% ice vol. regolith Siemens NX FEM thermal analysis results.

Component	Temperature [$°C$]		Component	Temperature [$°C$]	
DRPS radiator	max: 152 (top side) min: 150 (on heat pipes)		Volatiles tube initial trait	max: 145 (on plate) min: 128 (out of AD wall)	
Heat pipes	max: 150 (on DRPS) min: 147 (on plate)		Volatiles tube middle trait	max: 128 (sleeve entrance) min: 48 (out of sleeve)	
Sublimation plate	max: 147 (on heat pipe) min: 145 (on radiator)		Volatiles tube terminal trait	max: 48 (out of sleeve) min: 46 (tube end)	
MLI tent	Int.	min: 53 (AD wall) max: 68 (to regolith)	Cold trap thermal washer	Radially	min: -30 (to AD wall) max: 46 (to tube)
	Ext.	min: 52 (AD wall) max: 67 (to regolith)		Face seeing ice	min: 4 max: 17
Regolith max.	133 (centre of mining area)		Ice	-128	
DRPS structure	max: 150 (to DRPS) min: 86 (on walls)		Cold trap	Fins: -129 Radiator: -130	
DRPS sleeve	Int.	min: 72 (lower angle) max: 86 (top side)	Adiabatic walls	max: 100 (inside sleeve) min: -125 (front of rover) rear min: -55 (AD wall)	
	Ext.	min: 40 (lower angle) max: 54 (top side)			

Table 7.2: 1% ice vol. regolith Siemens NX FEM thermal analysis results.

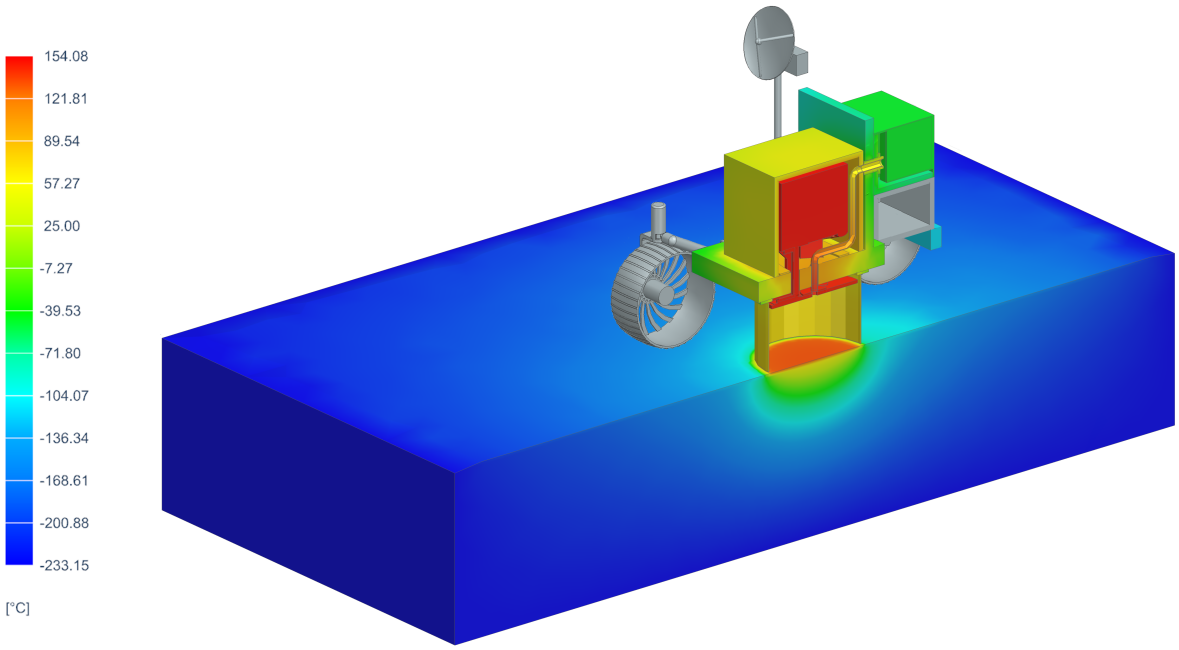

Figure 7.5: 5% ice vol. regolith Siemens NX FEM thermal analysis results.

Component	Temperature [$°C$]		Component	Temperature [$°C$]	
DRPS radiator	max: 154 (top side) min: 152 (on heat pipes)		Volatiles tube initial trait	max: 147 (on plate) min: 131 (out of AD wall)	
Heat pipes	max: 152 (on DRPS) min: 149 (on plate)		Volatiles tube middle trait	max: 131 (sleeve entrance) min: 64 (out of sleeve)	
Sublimation plate	max: 149 (on heat pipe) min: 147 (on radiator)		Volatiles tube terminal trait	max: 64 (out of sleeve) min: 62 (tube end)	
MLI tent	Int.	min: 55 (AD wall) max: 70 (to regolith)	Cold trap thermal washer	Radially	min: -2 (to AD wall) max: 63 (to tube)
	Ext.	min: 54 (AD wall) max: 69 (to regolith)		Face seeing ice	min: 25 max: 35
Regolith max.	135 (centre of mining area)		Ice	-40 (near tube); -44 (away from tube)	
DRPS structure	max: 152 (to DRPS) min: 82 (on walls)		Cold trap	Fins: -45 Radiator: -46	
DRPS sleeve	Int.	min: 73 (lower angle) max: 88 (top side)	Adiabatic walls	max: 102 (inside sleeve) min: -112 (front of rover) rear min: -52 (AD wall)	
	Ext.	min: 42 (lower angle) max: 55 (top side)			

Table 7.3: 5% ice vol. regolith Siemens NX FEM thermal analysis results.

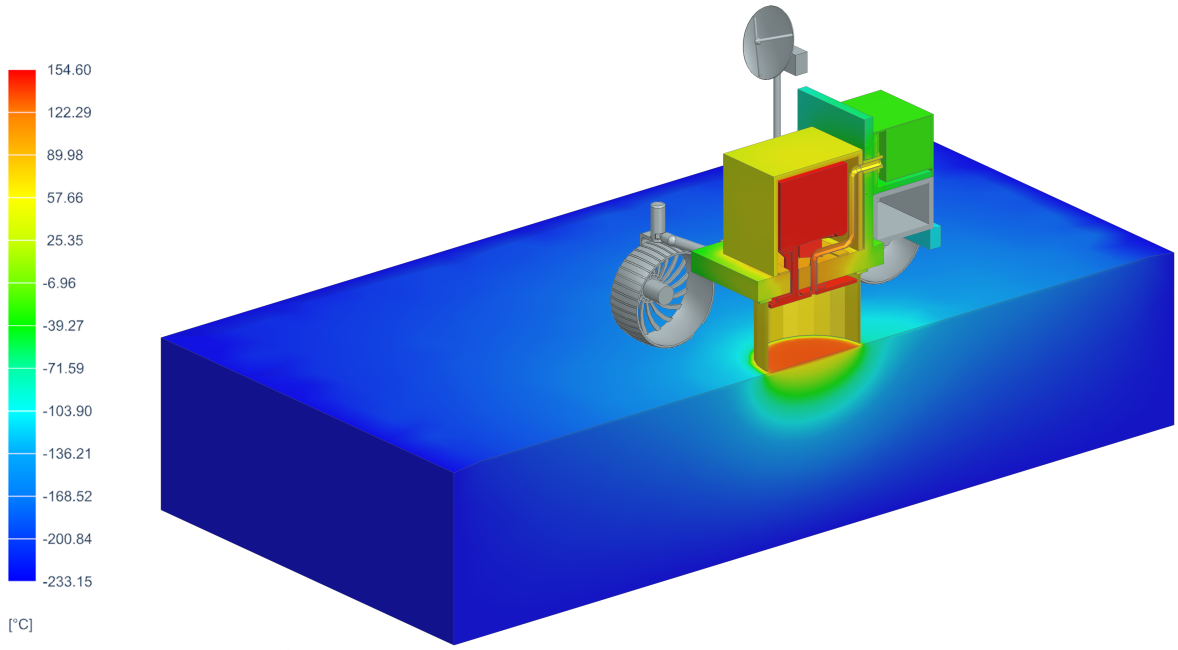

Figure 7.6: 10% ice vol. regolith Siemens NX FEM thermal analysis results.

Component	Temperature [$°C$]		Component	Temperature [$°C$]	
DRPS radiator	max: 154 (top side) min: 152 (on heat pipes)		Volatiles tube initial trait	max: 147 (on plate) min: 132 (out of AD wall)	
Heat pipes	max: 152 (on DRPS) min: 150 (on plate)		Volatiles tube middle trait	max: 132 (sleeve entrance) min: 69 (out of sleeve)	
Sublimation plate	max: 150 (on heat pipe) min: 148 (on radiator)		Volatiles tube terminal trait	max: 69 (out of sleeve) min: 67 (tube end)	
MLI tent	Int.	min: 56 (AD wall) max: 71 (to regolith)	Cold trap thermal washer	Radially	min: 7 (to AD wall) max: 67 (to tube)
	Ext.	min: 54 (AD wall) max: 69 (to regolith)		Face seeing ice	min: 32 max: 42
Regolith max.	136 (centre of mining area)		Ice	-20 (near tube); -25 (away from tube)	
DRPS structure	max: 152 (to DRPS) min: 88 (on walls)		Cold trap	Fins: -26 Radiator: -27	
DRPS sleeve	Int.	min: 73 (lower angle) max: 89 (top side)	Adiabatic walls	max: 103 (inside sleeve) min: -107 (front of rover) rear min: -50 (AD wall)	
	Ext.	min: 42 (lower angle) max: 56 (top side)			

Table 7.4: 10% ice vol. regolith Siemens NX FEM thermal analysis results.

8 | Conclusions

The very preliminary results of this work show that it is possible to extract ice in a PSR crater of the Moon south pole. The amount of ice recovered in a single extraction cycle varies according to the regolith percentage ice vol., but nothing impedes the rover from conducting more than one extraction cycles in a single journey back and forth from its reference station, until all the cold trap volume have been occupied. According to the cold trap dimensions of the rover CAD model used in the analysis, a minimum amount of 50 kg of water ice can be deposited and stored in the cold trap, equivalent to a volume of 55 litres. This value corresponds to a deposited ice layer around the fin surface of 5 cm thickness, which is the size of the ice block simulated in NX. The total amount of recovered ice could increase if more ice were allowed to deposit, so the 50 kg value only represents a baseline.

Various architectural trade-offs have been performed during the early phases of the design process, leading to the definition of the current TMS architecture. The employment of a Stirling based dynamic conversion radioisotope power system will grant the ice-mining Lunar rover enough electric power output to make it autonomous, without compromising its ice-mining capabilities, as per requirements (section 2.2).

The other two two basic temperature requirements over the TMS, presented in section 2.2, regarding sublimation plate and cold trap temperature have also been satisfied with generous margins, both in the nominal working case, regarding 5% ice vol. deposits in the Lunar regolith, and in other off-nominal scenarios. The findings of this work shows that the concept of ice-mining Lunar rover with the current TMS is a feasible one, as ice can be successfully sublimated from the regolith and deposited in the cold trap. It has also been found that an increase in the cold trap radiating surface would benefit the extraction of water from richer ice deposit, as the maximum temperature threshold for deposition is hit in the 10% ice vol. scenario.

9 | Future developments

This work is just the initial step of the design process for the ice-mining Lunar rover, and it could be forwarded in many ways. This chapter will enumerate some of the possible future developments which could be carried out. Apart from simulating the whole rover, adding the rest of its subsystems and increasing in their complexity, the thermal analysis work performed for this thesis underlined the need of further explorations of rover transients, both inside and outside of operational environment. On the other hand, a more thorough characterization of the heat loads and boundary conditions could be performed by creating a model for the sublimation of ice within regolith, and by testing it empirically with some experiments.

9.1. Transient analysis

The presented work aimed at studying the feasibility of the ice-mining Lunar rover concept by analysing its steady state behaviour, allowing to assess the feasibility of concept in a simple and straightforward way by simulating operational worst case scenarios. The reliance on the assumption that the investigated steady states represent the extreme conditions that the rover will have to face ensured that the TMS can satisfy the basic requirements requested from it. Transient analysis will benefit the design by describing what happens in between the simulated scenarios, providing insights on the TMS that might result in better performances.

9.1.1. Analysis of transients in operational environment

This analysis refers to a more detailed characterization of what happens at the start and the end of the extraction process. Extreme case scenarios are represented by the rover being stationary over different ice vol. content or dry regolith, each one characterised by its own thermal loads. Future efforts should hence be dedicated to understanding the TMS behaviour during the initial and ending phases of ice mining. For the initial phase, it would be interesting to simulate the regolith warm up and the initial ice sublimation. For the final phase, the progressive diminution of the heat loads on the TMS, together with the increase in temperature of the regolith and the plate due to the absence of the sublimating ice heat sink, would be worthy of investigation. In order to simulate this more complex mining process, it is necessary to have available a model for the sublimation of ice in regolith, as mentioned in the next section.

9.1.2. Analysis of transients outside of operational environment

After transient in the mining PSR Lunar environment have been investigated, the analysis of transients outside of operational environment should be performed. This part of the work would encompass an examination of the rover survivability on very different environmental conditions, such as during launch, or if traversing a non PSR zone, for example after having been deployed or when coming back to the reference station to handout the collected ice. Such a transient analysis is necessary as the rover TMS design have been optimized for ice extraction in a PSR environment, which is radically different from the launch or the non-PSR environment on the Moon. It is vital that this phases must be maintained as short as possible, especially the non-PSR environment roving one. A detailed transient thermal analysis is required to assess the stress accumulated over by the TMS during operations outside of PSR, in order to ensure the rover survivability in all the environments it might encounter.

9.2. Model for the sublimation of ice within regolith

One of the most limiting restrictions on the rover mining performances validation over different ice % vol. contents was the scarcity of data regarding the volatiles mass flow rates for ice sublimating inside the regolith. The creation of a model able to provide reliable data on the ice extraction rates, which are also the mass flow rates of volatiles, would greatly help to characterize the heat load to be dissipated in the cold trap and the thermal sink effect from the sublimation latent heat of the ice being extracted in the regolith.

A simple initial step would be to account for the increase in conductivity in regolith due to ice dispersed within, also considering ice sublimation according to local temperature and pressure conditions. A more refined model could then be used to derive inputs for future simulations, as the heat loads on the TMS and the heat sink term in the regolith, that will be necessary to simulate the thermal transients for the ice-mining phase mentioned in the previous section.

9.3. Experiments on regolith

Finally, a series of experiments on the regolith would help to empirically validate the aforementioned model. Such experiments could initially focus on the sublimation plate dynamics during the ice extraction phase, reproducing the Lunar PSR ice deposits by cooling a vacuum chamber containing a regolith-like silicate mineral with ice deposits of various forms and mass dispersed inside it, over which would be placed an electrically heated prototype of the sublimation plate.

Apart from giving an empirical demonstration of the ice mining process, a similar experiment would also offer a precious opportunity to study the interactions between the MLI tent and the regolith soil, helping to develop better adhesion between the tent sealing and the terrain, limiting volatiles losses when extracting ice on the Moon.

Bibliography

[1] Jeffrey S. Parker and Rodney L. Anderson. *Low-Energy Lunar Trajectory Design*, volume 12. NASA JPL, DESCANSO Book Series, July 2013. Pages 1-12.

[2] United Launch Alliance. InSight Launch Booklet. www.ulalaunch.com, 2018.

[3] William Graham. Atlas V launches MAVEN en route to Martian adventure. www.nasaspaceflight.com, 2013.

[4] United Launch Alliance. Atlas V Juno: Mission Overview. www.ulalaunch.com, 2011.

[5] NASA. NASA Moon to Mars website. https://www.nasa.gov/specials/moontomars /index.html, 2023.

[6] Office of Inspector General - NASA's management of the Artemis missions. https://oig.nasa.gov/hotline.html., 2021.

[7] NASA Fiscal Year 2023 Budget Request. https://www.nasa.gov/sites/default/files /atoms/files/fy23_nasa_budget_request_summary.pdf.

[8] ESA Agenda 2025; ESA unclassified-for public release. https://www.esa.int/About_Us/ESA_Publications/Agenda_2025.

[9] Terrae novae 2030+ strategy roadmap. https://esamultimedia.esa.int/docs/ESA _Agenda_2025_final.pdf, 2022.

[10] BBC Paul Rincon. China lands Jade Rabbit robot rover on Moon. https://www.bbc.com/news/science-environment-25356603, 14 Dec 2013.

[11] CNN. China Lunar rover touches down on far side of the Moon, state media announce. https://edition.cnn.com/2019/01/02/health/china-lunar-rover-far-moon-landing-intl/index.html, 4 Jan 2019.

[12] Space News. China recovers Chang'e-5 moon samples after complex 23-day mission. https://spacenews.com/china-recovers-change-5-moon-samples-after-complex-23-day-mission/, 16 Dec 2020.

[13] G. Baiocco et al. A water-filled garment to protect astronauts during interplanetary missions tested on board the iss. *Life Sciences in Space Research*, 18:1–11, 8 2018.

[14] Robert Singleterry. Radiation engineering analysis of shielding materials to assess their ability to protect astronauts in deep space from energetic particle radiation. *Acta Astronautica*, 91:49–54, 04 2013.

[15] Ian Crawford. Lunar resources: A review. *Progress in Physical Geography*, 39:137–167, 04 2015.

[16] D. A. Paige et al. The lunar reconnaissance orbiter diviner lunar radiometer experiment. *Space Science Reviews*, 150:125–160, 1 2010.

[17] Norbert Schorghofer and G. Jeffrey Taylor. Subsurface migration of h2o at lunar cold traps. *Journal of Geophysical Research: Planets*, 112, 2 2007.

[18] NASA CLPS Website. https://www.nasa.gov/commercial-lunar-payload-services.

[19] NASA. NASA Science. https://science.nasa.gov/lunar-discovery/deliveries.

[20] Hannah M Sargeant, Ramy Mesalam, Emily Jane Watkinson, Alessandra Barco, Richard M Ambrosi, Leo Gard, Bert Lara, Erik Scougal, and Tim Tinsley. Ice-mining on the moon with radioisotope power systems. Proceedings of the Nuclear and Emerging Technologies for Space, Idaho Falls, ID, USA, 7-11 May., 2023.

[21] Hannah Sargeant, Ramy Mesalam, Alessandra Barco, Emily Jane Watkinson, Richard Ambrosi, Marzio Mazzotti, Leo Gard, Bert Lara, Erik Scougal, and Tim Tinsley. Radioisotope power sources: A novel approach to ice mining on the moon. *Proceedings of the European Space Power Conference, Elche, Spain*, (2023).

[22] Julie Brisset, Thomas Miletich, and Philip Metzger. Thermal extraction of water ice from the lunar surface - a 3d numerical model. *Planetary and Space Science*, 193, 11 2020.

[23] K. Hadler et al. A universal framework for space resource utilisation (sru). *Planetary and Space Science*, 182, 3 2020.

[24] D. A. Paige et al. The lunar reconnaissance orbiter diviner lunar radiometer experiment. *Space Science Reviews*, 150:125–160, 1 2010.

[25] ESA. ESA Website. https://www.esa.int/Enabling_Support/Preparing_for_the_ Future/ Space_for_Earth/Energy/Helium-3_mining_on_the_lunar_surface.

[26] Sanders Gerald. "What next for space resource utilisation?" Workshop, LuxExpo. Technical report, NASA Johnson Space Center Houston, 10 Oct 2019. Document ID: 20190032062.

[27] Carsten Schwandt, James A. Hamilton, Derek J. Fray, and Ian A. Crawford. The production of oxygen and metal from lunar regolith. volume 74, pages 49–56, 12 2012.

[28] Anthony Colaprete, Peter Schultz, and Jennifer Heldmann et al. Detection of water in the lcross ejecta plume. *Science*, 330:463–468, 10 2010.

[29] NASA. Volatiles investigating polar exploration rover 4/30/2021.

[30] K Ennico-Smith, A Colaprete, D S S Lim, and D Andrews. The viper mission, a resource-mapping mission on another celestial body. https://www.nasa.gov/viper.

[31] Kevin M. Cannon and Daniel T. Britt. A geologic model for lunar ice deposits at mining scales. *Icarus*, 347, 9 2020.

[32] R Terik Daly and Peter H Schultz. The delivery of water by impacts from planetary

accretion to present. https://www.science.org, 2018.

[33] P. Prem, N. A. Artemieva, D. B. Goldstein, P. L. Varghese, and L. M. Trafton. Transport of water in a transient impact-generated lunar atmosphere. *Icarus*, 255:148–158, 7 2015.

[34] J.W. Head. Lunar volcanism in space and time. *Rev. Geophys*, 14:265–300, 1976.

[35] D H Needham and M Siegler et al. Calculated thicknesses of volcanically derived water ice deposits at the lunar poles. *50th Lunar and Planetary Science Conference 2019*, 2019.

[36] James Wilson et al. Volcanically induced transient atmospheres on the moon: Assessment of duration, significance, and contributions to polar volatile traps. *Geophysical Research Letters*, 47, 09 2020.

[37] John E. Moores. Lunar water migration in the interval between large impacts: Heterogeneous delivery to permanently shadowed regions, fractionation, and diffusive barriers. *The Journal of Geophysical Research Planets*, 121, 01 2016.

[38] Dana Crider and Richard Vondrak. Space weathering effects on lunar cold trap deposits. *Journal of Geophysical Research*, 108, 07 2003.

[39] Vladimir Airapetian and Arcadi Usmanov. Reconstructing the solar wind from its early history to current epoch. *The Astrophysical Journal*, 817, 01 2016.

[40] Quentin Pognan, C. Garraffo, Ofer Cohen, and Jeremy Drake. The solar wind environment in time. *The Astrophysical Journal*, 856, 02 2018.

[41] Terry Fong. VIPER: Volatiles Investigating Polar Exploration Rover, 29 Mar 2021.

[42] M. A. Siegler and David Paige. Subsurface ice stability on the Moon. Aug 2018.

[43] Kenneth Watson et al. The behavior of volatiles on the Lunar surface. Sep 1961.

[44] Norbert Schorghofer and G. Jeffrey Taylor. Subsurface migration of h2o at lunar cold traps. *Journal of Geophysical Research: Planets*, 112, 2 2007.

[45] Siegler Paige. Diviner lunar radiometer observations of cold traps in the moon's south polar region. *Science*, 22; pg 479-82, Oct 2010.

[46] Emily Costello, Rebecca Ghent, and Paul Lucey. The mixing of lunar regolith: Vital updates to a canonical model. *Icarus*, 314:327–344, 11 2018.

[47] Costello et al. Impact gardening as a constraint on the age, source, and evolution of ice on mercury and the moon. *Journal of Geophysical Research: Planets*, 125, 03 2020.

[48] Siegler et al. Lunar true polar wander inferred from polar hydrogen. *Nature*, 531:480–484, 03 2016.

[49] David Paige; M. A. SieglerJ, .T. Keane. Subsurface Ice Stability on the Moon: What lies beyond the frost? https://www.esa.int/Enabling_Support/Preparing_for_the_ Future/ Space_for_Earth/Energy/Helium-3_mining_on_the_lunar_surface.

[50] Philip T Metzger et al. Nasa innovative advanced concepts (niac) phase i grant number 80nssc 20k1022 aqua factorem: Ultra low energy lunar water extraction final report.

[51] Li S et al. Direct evidence of surface exposed water ice in the lunar polar regions. *Proceed-*

ings of the National Academy of Sciences of the United States of America, 115:8907–8912, 9 2018.

[52] Mike Wall. No digging required: Space mining on the moon and beyond may be solar powered. https://www.space.com/moon-asteroid-space-mining-with-concentrated-sunlight.html, 4 Sep 2019.

[53] George Sowers. Thermal mining of ices on cold solar system bodies niac phase i final report, 2019.

[54] Martin J. Losekamm et al. Assessing the distribution of water ice and other volatiles at the lunar south pole with luvmi-x: A mission concept. *Planetary Science Journal*, 3, 10 2022.

[55] Kuan-Lin Lee, Calin Tarau, Quang Truong, Srujan Rokkam, Kris Zacny, Hunter Williams, and Dean Bergman. Thermal management system for lunar ice miners, 12-15 July 2021.

[56] George R Schmidt and Robert D Abelson et al. Enabling exploration with small radioisotope power systems, 2004.

[57] Eric S Clarke and Joe Giglio et al. Multi-mission thermoelectric generator assembly testing and launch operations for mars 2020. http://www.inl.gov, 2021.

[58] Richard M. Ambrosi, Hugo Williams, Emily Jane Watkinson, Alessandra Barco, and Ramy Mesalam et al. European radioisotope thermoelectric generators (RTGs) and radioisotope heater units (RHUs) for space science and exploration, 11 2019.

[59] NASA. About plutonium-238. https://rps.nasa.gov/about-rps/about-plutonium-238/.

[60] Sanchez-Torres. *Radioisotope Power Systems for Space Applications*. InTech, 10 2011.

[61] Steven D Howe, Douglas Crawford, Jorge Navarro, and Terry Ring. Economical production of pu-238: Feasibility study nasa niac phase i.

[62] Smith R. B., Romero F., and Vicente R. Plutonium-238: The fuel crisis. *Brazilian Journal of Radiation Sciences*.

[63] Oak Ridge National Laboratory. Ornl-produced plutonium-238 to help power perseverance on mars. https://www.ornl.gov/news/ornl-produced-plutonium-238-help-power-perseverance-mars.

[64] Space exploration: DOE could improve planning and communication related to plutonium-238 and radioisotope power systems production challenges, accessible version report to congressional requesters U]nited States Government Accountability Office, 2017.

[65] C S Chong, A Shukri, and A A Tajuddin. Gamma ray spectrum of am-241 in a back scattering geometry using a high purity germanium detector.

[66] R M Ambrosi et al. Development and testing of americium-241 radioisotope thermoelectric generator: Concept designs and breadboard system.

[67] Christine Guéneau, Alain Chartier, and Laurent Van Brutzel. *Thermodynamic and Thermophysical Properties of the Actinide Oxides*, volume 2, pages 21–59. 02 2012.

[68] Jamie Brown et al. Americium and plutonium purification by extraction (the amppex process): Development of a new method to separate 241 am from aged plutonium dioxide for use in space power systems. *Progress in Nuclear Energy*, 106:396–416, 07 2018.

[69] Turbo-brayton converter for radioisotope power systems rps community review, 2018.

[70] Eric S Clarke and Joe Giglio et. al. Multi-mission thermoelectric generator assembly testing and launch operations for mars 2020. http://www.inl.gov, 2021.

[71] June F Zakrajsek. Nuclear power assessment study-final nuclear power assessment study final report.

[72] Advanced stirling radioisotope generator (asrg) national aeronautics and space administration how does an asrg work? www.nasa.gov.

[73] A. Lou Qualls et al. Dynamic radioisotope power system development for space exploration. IEEE Computer Society, 6 2017.

[74] T. Bradshaw J. Watson C.Pulker et al. G. Gilley, M. Crook. Development of the european radioisotope stirling generator (ersg).

[75] Andrew Klein et al. October 2020 nasa/cr20205009307 operational considerations for fission reactors utilized on lunar in-situ resource utilization missions, a report to the nuclear power propulsion technical discipline team. http://www.sti.nasa.gov.

[76] Lee S. Mason; Glenn Research Center Cleveland Ohio. A comparison of fission power system options for Lunar and Mars surface applications. http://www.sti.nasa.gov, 2006.

[77] Sterling Bailey et al. Small fission power system feasibility study final report without export control warning), 13 May 2010.

[78] Patrick Hull et al. Thermal analysis and shape optimization of an in-space radiator using genetic algorithms. *AIP Conference Proceedings*, 813:81–90, 01 2006.

[79] Kuan Lin Lee, Calin Tarau, William G. Anderson, and Derek Beard. Titanium-water heat pipe radiators for space fission power system thermal management. *Microgravity Science and Technology*, 32:453–464, 6 2020.

[80] Mohammed T Ababneh et al. Hybrid variable and constant conductance heat pipes for lunar and martian environments and high heat flux space applications.

[81] Marc A Gibson et al. Nasa's kilopower reactor development and the path to higher power missions. http://www.sti.nasa.gov, 2017.

[82] Cleveland Jan Wittry, NASA's Glenn Research Center. Kilopower. https://www.nasa.gov/directorates/spacetech/kilopower, 2017.

[83] NASA Gleen Research Center. Dynamic thermal energy conversion: photo gellery. https://www1.grc.nasa.gov/research-and-engineering/thermal-energy-conversion/.

[84] NASA. Mars pathfinder landing - NASA's mars exploration program press kit.

[85] J Matijevic. "Sojourner", the Mars pathfinder microrover flight experiment.

[86] Bickler Morgan. The retelling of "Romancing the rover". JPL. Archived from the original

(PDF) on 27 May 2010. Retrieved 25 September 2010.

[87] G. Hickey D.F. Braun H.J.Eisen, L.C. Wen. Sojourner Mars rover thermal performance. *Jet Propulsion Laboratory, California Institute of Technology, Pasadena.*

[88] Joy A. Crisp et al. Mars exploration rover mission. *Journal of Geophysical Research: Planets*, 108, 12 2003.

[89] Randel A. Lindemann and Chris J. Voorhees. Mars exploration rover mobility assembly design, test and performance. volume 1, pages 450–455, 2005.

[90] John P. Grotzinger et al. Mars science laboratory mission and science investigation. *Space Science Reviews*, 170:5–56, 9 2012.

[91] NASA. Mars 2020 mission overview. https://mars.nasa.gov/resources/7909/computer-design-drawing-for-nasas-2020-mars-rover/.

[92] Pradeep Bhandari et al. Mars science laboratory thermal control architecture, 2005.

[93] 2009) Watanabe, Susan (August 9. "keeping it cool (...or warm!)". nasa/jpl. 2021. https://www.nasa.gov/mission_pages/mars/images/20081209_msl.htm.

[94] ESA. Marsfast. https://sci.esa.int/web/future-missions-department/-/56167-cdf-study-report-marsfast-rover.

[95] ESA. Marsfast assessment of an esa fast mobility mars rover, 2014.

[96] Lunokhod mission diagram. https://en.wikipedia.org/wiki/Lunokhod_programme.

[97] Sean Blair. Rovers, learning from lunokhod. https://eandt.theiet.org/content/articles/2011/03/rovers-learning-from-lunokhod/, 14 Mar 2011.

[98] NASA Space Data Coordinated Archive. Luna 21/lunokhod 2. https://nssdc.gsfc.nasa.gov/nmc/spacecraft/display.action?id=1973-001A.

[99] Oleson et al. Use of an americium-based dynamic radioisotope power system (drps) for a long duration lunar science rover. *Proceeding of the Nuclear and Emerging Technologies for Space, May 7-11 2023, Idaho Falls, ID.*, 2023.

[100] Steven Oleson et al. Use of a dynamic radioisotope power source for a long duration lunar science rover. https://ntrs.nasa.gov/citations/20220004665.

[101] NASA Glenn Research Centre. Dynamic radioisotope power systems (drps). https://www1.grc.nasa.gov/research-and-engineering/thermal-energy-conversion/rps-program/, 2021.

[102] R. Vaughan. Viper volatiles investigating polar exploration rover: Mission overview. *in International Small Satellite Conference*, 11 May 2020.

[103] Astrobiotic press release. Astrobotic's moonranger moves into final production. https://www.astrobotic.com/astrobotics-moonranger-moves-into-final-production/, 16 Jun 2021.

[104] Lydia Schweitzer et al. Micro rover mission for measuring lunar polar ice. volume 2021-March. IEEE Computer Society, 3 2021.

[105] J Biswas and et al. Exploring the moon with the lunar volatiles mobile instrumentation-extended (luvmi-x) platform.

[106] A mobile platform for lunar exploration experiments configurations. https://www.spaceapplications.com/.

[107] M J Losekamm et al. Searching for water ice with the luvmi-x lunar rover.

[108] Guillaume Fau et al. Luvmi-x rover: test results and prospects. https://www.researchgate.net/publication/364128399.

[109] Google lunar x-prize website. https://www.xprize.org/prizes/google-lunar.

[110] Alberto Della Torre et al. Amalia mission lunar rover-the conceptual design of the team italia rover. *Acta Astronautica*, 67:961–978, 10 2010.

[111] Christopher Roberts et al. Space systems engineering: Rapid modelling of mars robotic explorers. mit opencourseware. http://ocw.mit.edu16.89J/ESD.352Jhttp://ocw.mit.edu/terms., 2007.

[112] V. T. Bickel, B. Moseley, I. Lopez-Francos, and M. Shirley. Peering into lunar permanently shadowed regions with deep learning. *Nature Communications*, 12, 12 2021.

[113] Richard Volpe, J. Balaram, Timothy Ohm, and Robert Ivlev. Rocky 7: A next generation Mars rover prototype. *Advanced Robotics*, 11:341–358, 1 1996.

[114] Evoink Operations GmbH. ROHACELL HERO Thermal Insulator. https://performance-foams.evonik.com/en/products-and-solutions/rohacell/rohacell-hero-170036.html.

[115] P. Lognonné, W. B. Banerdt, and D. Giardini. Seis: Insight's seismic experiment for internal structure of mars. *Space Science Reviews*, 215, 1 2019.

[116] Robert J Christie, David W Plachta, and Mohammad M Hasan. Transient thermal model and analysis of the lunar surface and regolith for cryogenic fluid storage. http://www.sti.nasa.gov, 2008.

[117] Andersson and Inaba. Thermal conductivity of crystalline and amorphous ices and its implications on amorphization and glassy water. volume 7, pages 1441–1449, 4 2005.

[118] Norman Anderson and Alex Travesset. The many phases of ice. http://www.physics.iastate.edu/staff/travesset/phasesofice.doc.

[119] London South Bank University. The phase diagram of water. https://ergodic.ugr.es/termo/lecciones/water1.htmlbg.

[120] David Kornuta et al. Commercial lunar propellant architecture: A collaborative study of lunar propellant production, 3 2019.

[121] MathWorks. How Simscape Simulation Works. https://it.mathworks.com/help/simscape/ug/how-simscape-simulation-works.html.

[122] Jesse Stuck. ELHS – DRPS Heat Transfer Model. Leicester University provided source, 11/02/2022.

A | Appendix A: FEM analysis materials properties table

Material	Components	Thermal conductivity	Infrared emissivity
Rohacell 71 HERO foam	Adiabatic wall DRPS sleeve cold trap insulation	0.0246 W/(m·K)	-
MLI	MLI tent DRPS sleeve cover Adiabatic wall cover	0.155 W/(m·K)	0.05
Aluminium 6061	DRPS radiator heat pipes structure Sublimation plate	167 W/(m·K)	0.2; 0.95 for plate radiator
Copper C10100	Volatiles tube, cold trap fins and radiator	398 W/(m·K)	0.2; 0.9 for trap radiator
Ti-6Al-4V	DRPS Structure	6.7 W/(m·K)	0.34
Heat pipes	Heat pipes	50000 W/(m·K)	-
PEEK	Thermal washer and other insulating joints	0.25 W/(m·K)	0.95
Carbon fibre	Composite skin in cold trap	24 W/(m·K)	0.85
Ice	Ice in cold trap and mixed in the regolith	$k_{ice} = 632/T +$ $+0.38$ -0.00197·T; $40\text{K} \leqslant T \leqslant 273K$	0.97
Fluff	Regolith top layer	$k_{fluff} = 9.22 \cdot 10^{-4}$ $[1 + 1.48(T/350)^3]$	0.97
Regolith	Regolith bulk	$k_{regolith} = 9.30 \cdot 10^{-3}$ $[1 + 0.73(T/350)^3]$	-

B | Appendix B: Commentary of attached files

The results presented in this work have been obtained through the use of various different softwares. Here will be presented a list of the files produced to derive them:

- The rover 1D thermal network, a MATLAB/Simulink file.
- The rover 1D thermal network input file, a MATLAB script.
- A series of simpler couples of MATLAB input scripts and Simulink 1D thermal networks for the tradeoff analysis.
- A MATLAB script solving the pressure equilibrium in the MLI tent.
- A MATLAB script calculating the cold trap geometry and the number of fins.
- The rover CAD model assembly, with all its parts, as a part file on Siemens NX.
- Four couples of FEM files and simulation files representing the four regolith ice vol. content cases for the 3D thermal analysis on Siemens NX.
- A series of Excel files containing the thermal conductivity for regolith, regolith fluff, ice and their mixtures to be input in the Siemens NX files.

Acknowledgements

I would like to acknowledge for the help provided in the realisation of this work all my supervisors, mentioned in the title page. Special thanks go to my University of Leicester supervisors, Alessandra Barco, Ramy Mesalam and Hannah Sargeant, for having closely followed my progresses and assisted me during my setbacks while at Space Park. Finally, I would also like to thank Dr. Kuan-Lin Lee, and his colleague, Dr. Sai Kiran Hota, for their very helpful correspondence, which clarified many of my doubts.